Material Physics

Department of Physics and

Astronomy

University of Sussex

PhD Dissertation

Applications of High Surface Area Carbon Nanomaterials

Author:

Sebastian Nufer

Supervisors:

Dr. Adam Brunton

Prof. Alan B. Dalton

14th April 2019

Acknowledgments

Firstly I would like to thank my supervisor Dr. Adam Brunton at M-Solv. His numerous advices, feedbacks and ideas contributed significantly to this work and lead me through the project.

I also thank Prof. Alan Dalton for his contributions to the thesis, which were crucial and helped me realize this thesis.

I would like to express my gratitude to Phil Rumbsy for making it possible to do my research in M-Solv's Research and Development team. His interest in research and the open mind for innovation taught me a great deal.

To all of the R&D members at M-Solv, who were very supportive through the entire doctoral thesis time. I thank them for their patience answering all the questions I had. It was great fun to work together in the lab with Dave Myles, Dimitrios Fantanas, Greg Rigas, Helios Chan, Maria Cann, Marta Kozak, Mickey Crozier, Mirek Kula, Munya Ziyenge, Simon Henley and Vijay Tailor.

I would also like to thank the entire team of the Material Physics group at the University of Sussex. I had great discussions and scientific advice from Alice King, Aline Graf, Giuseppe Fratta, Manuela Meloni, Matt Large, Peter Lynch and Sean Ogilvie without which I could not have finished this thesis.

I had a great experience being part of the Enabling Excellence network, which organised the funding. The students in the project Ana Santidrian, Antonia Kagkoura, Daniel Funes, Dominik Winterauer, Emin Istif, Lorenzo Vallan, Mario Fernandez, Ruben Canton, Yuman Baraza made the entire journey throughout the thesis an interesting time. Thanks to their supervisor Ana Benito, Chris Ewels, Nikos Tagmatarchis, Raul Arenal, Tim Batten and Wolfgang Maser, who never got tired answering all my questions on chemistry and nanomaterials. I would also like to thank the people helping on the project and the numerous workshops given by Edward

Goldwyn, Elodie Babu and Richard Lee, it would not have been the same without them.

Three years is a long time to be away from family and I am truly grateful to my parents and my brother for being so kind and understanding. I am grateful to them to the wonderful start I have had in my life.

Special thanks to Alice King, Chris Lim, Dave Myles, James Buffham and Margherita Nulli for proof-reading my thesis.

Finally I would like to acknowledge the financial support from the European Union Horizon 2020 under the Marie Sklodowska-Curie Training Networks (ITN-ETN) grant number 642742, which gave me the opportunity to work in the European wide network.

Contents

Abstract

In recent years carbon nanomaterials have shown great potential in various applications; among them gas sensing and supercapacitor electrodes. Devices reported in the literature, which are built to exploit the properties of the nanomaterials are often based on expensive multistep processes. As nanomaterials start to be commercially available, the remaining challenge is to find scalable fabrication methods to take advantage of the nanomaterial characteristics. In this thesis, manufacturing techniques and materials are presented which enable technically and commercially interesting gas sensors based on nanomaterials with interdigitated electrodes.

Graphene flake dispersions are readily available on the market in large quantities. Currently most available materials are actually multilayer graphene rather than single pristine sheets of carbon atoms. Flake sizes are typically below 1 μm preventing the readout of individual sheets. Nevertheless these small graphene sheets can be made to form a percolating film when dispensed and compressed in a L-S trough. Such films can be transferred to readout electrodes which have been pre-patterned by laser ablation. This simple three step process creates a sensor which is read-out by resistance measurement.

In this work, sensors have been manufactured, with this device architecture, showing performance compatible with personal safety applications. Their detection limit of 1 ppm for NH_3 with a response time of 90 seconds competes with current commercial systems. Investigation into the sensing mechanism of these percolating films reinforces the scalability of the fabrication method. Using reducing (NH_3) and oxidising (acetone) gases we determined the origin of the sensor's response. KPFM and Raman analysis show basal plane doping of the graphene sheets in opposite direction when exposed to the reducing and the oxidising agent. The resistance of the film increases in both cases when exposed to the gases. This leads to the conclusion

that the dominating sensing mechanism in the percolating graphene film takes place at the contacts of the flakes in the film. This sensing mechanism allows the use of even relatively low quality graphene flakes to make effective devices. Defects in the basal plane play a negligible role within the films as the edge properties are responsible for the adsorption.

Another, less well-investigated nanomaterial with gas sensing properties is carbon nanofoam (CNF). CNF is formed in a diffusion limited aggregation process where individual carbon clusters form elongated networks with a "web"-like appearance.

Synthesis of CNF and deposition onto readout electrodes in a single step is made possible by using a pulsed laser. The CNF is formed during the interaction between the laser and a precursor material, positioned close to the electrode onto which the CNF is to be deposited. This direct deposition method makes a film with good adhesion and uniformity. Metal functionalization using physical vapor deposition can be applied to the CNF in order to modify its sensing properties. Preliminary gas sensing studies, exposing both CNF and metallised CNFs to a changing humidity environment show responses of +70 % for CNF and -30 % for metallized CNF when the humidity is decreased by 17 %. This is among the highest reported response of carbon nanomaterials. The reaction of the CNF to dry air changing environment only takes 13 seconds to reach steady state while the functionalised material takes 32 seconds. The metallization of the CNF follows the percolation law as the foam acts as a scaffold for the sputtered metal particles. The sign of the response when exposed to a dry environment inverts when the percolation threshold is crossed. At the threshold the sensitivity to a change in humidity is suppressed. As water is a major interferent for carbon nanomaterials in gas sensing devices it is important to find ways to suppress the response of a device towards water.

CNF has also been used to make supercapacitors and their behaviour has been characterised.

Characterising the CNF in supercapacitor electrodes reveals a large influence of the gravimetric capacitance on the mechanical properties of the foam. Supercapacitors were made using directly-deposited CNF (as above) and also by transfer through a water sub-phase. The CNF lifts from the substrate when immersed into water and can then be picked up with another substrate. This transfer not only

induces a change in morphology but also introduces a compressional stress. These effects more than double the gravimetric capacitance from 17 $\mathrm{F\,g^{-1}}$ to 42 $\mathrm{F\,g^{-1}}$. The fragility of the CNF that this reveals indicates the necessity of a one-step deposition process as the properties of the CNF are easily changed if mechanical force is applied. Nevertheless the transfer enhances the specific capacitance greatly.

In summary, laser-deposition technology and a combination of laser ablation and L-S deposition allows scalable fabrication of gas sensor devices based on carbon nanomaterials. Similar devices show interesting supercapacitive properties but they do not, so far, approach the state of the art as defined by gravimetric capacitance.

Symbols

Acronyms and Abbreviations

AC	Alternate Current
AFM	Atomic Force Microscopy
CAD	Computer Aided Design
CMOS	Complementary Metal Oxide Semiconductor
CNF	Carbon Nanofoam
CNT	Carbon Nanotube
CPD	Contact Potential Difference
CV	Cyclic Voltammetry
CVD	Chemical Vapour Deposition
DC	Direct Current
DEFRA	Department for Environment Food and Rural Affairs
DFT	Density Functional Theory
DXF	Drawing Interchange Format
FEG-SEM	Field Effect Gun Scanning Electron Microscope
FET	Field Effect Transistor
GO	Graphene Oxide
IDE	Interdigitated Electrodes
ITO	Indium Tin Oxide
IoT	Internet of Things
KPFM	Kelvin Probe Force Microscopy
L-B	Langmuir Blodgett

LOD	Limit of Detection
L-S	Langmuir Schaefer
MWCNT	Multi Walled Carbon Nanotube
PANI	Polyaniline
PDMS	Polydimethylsiloxan
PECVD	Plasma Enhanced Chemical Vapour Deposition
PMMA	Polymethylmethacrylat
ppb	parts-per-billion
ppm	parts-per-million
ppq	parts-per-quadrillion
RF	radio frequency
rGO	reduced Graphene Oxide
rH	room Humidity
RVC	Reticulated Vitreous Carbon
SEM	Scanning Electron Microscope
TEM	Transmission Electron Microscope
UK	United Kingdom
UV	Ultra Violet
VOC	Volatile Organic Compound

List of Figures

List of Tables

List of Equations

Chapter 1

Introduction

When someone takes his smartphone out of the pocket usually it is not only to make a phone call. More often than not smartphones are used for something else other than making a call such as checking a text message, browsing the internet, taking a picture, looking at a picture, watching a video, listening to music and so on. Just 20 years back all of these actions required an individual gadget. If you would have spread all of these gadgets across a table they would have covered most of the space. On the other hand a smartphone nowadays only needs a fraction of it. The process of making electronic devices smaller is called *downscaling*.

All modern electronic technology has gone through this process. The most prominent downscaling has happened in the chip manufacturing industry, more specifically in the fabrication of transistors. More and more transistors are fitted on to a single chip without increasing its area [1]. These chips boost the performance of modern computers by making them quicker and allowing more calculations at the same time. The so called Moore's law describes the process of downscaling in the transistor world. It predicts that the number of transistors on a single chip doubles every year. So far Moore's law, established when transistors were still relatively large in size in the 20th century, has been very accurate. The number of transistors on a single chip currently doubles every 1.5 years. Figure 1.1 shows the history of Moore's law so far by looking at the number of calculations per second per 1000 $. The chip manufacturing world is concerned though, as the size of individual gates are approaching the physical limits of what is possible [2]. These limits lie in the nanometre regime, the size of current state-of-the-art devices are around 12 - 15 nm.

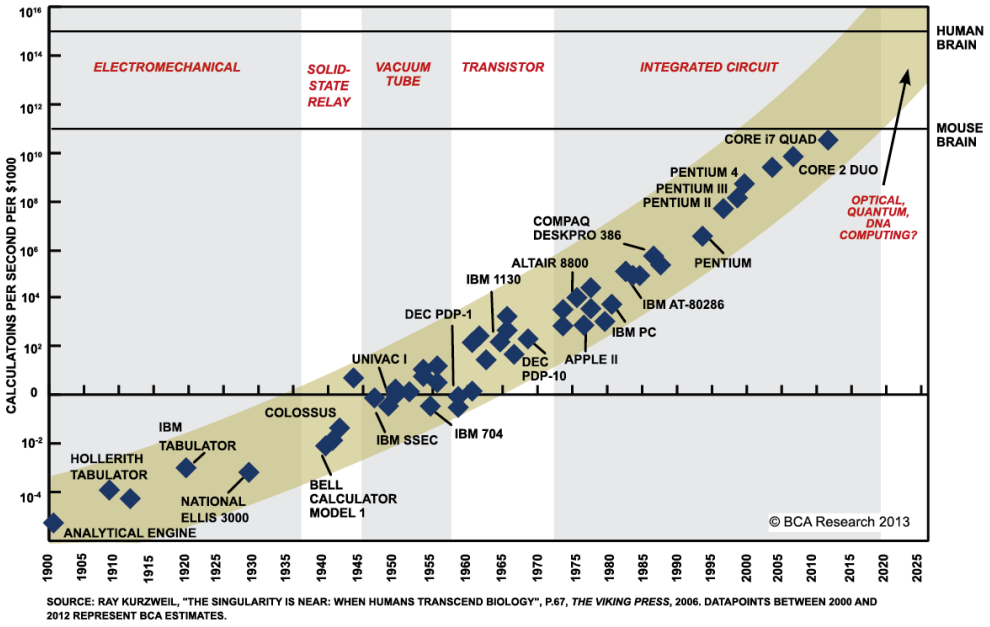

Figure 1.1: Moore's Law. Source ExtremeTech (https://www.extremetech.com/extreme/210872-extremetech-explains -what-is-moores-law), accessed on 17th of September 2018.

At these low dimensions materials start having different properties and behaviour compared to their bulk state. For example if heat is applied to nanometre sized materials the heat transfer within the material is so quick that they are heated almost instantly. In a similar setup with the same material in bulk form it takes minutes if not hours for the entire material to be uniformly heated.

The European Union defines a nanomaterial as follows: "A natural, incidental or manufactured material containing particles, in an unbound state or as an aggregate or as an agglomerate and where, for 50 % or more of the particles in the number size distribution, one or more external dimensions is in the size range 1 nm - 100 nm" [3]. A real nanomaterial is commonly defined as a material which has one or more dimensions below 10 nm. There are various shapes that nanomaterials can be found in [4]. Figure 1.2 illustrates the three basic shapes a carbon nanomaterial can be found in.

In the 0-dimensional form the material has a spherical shape with a diameter lower than 10 nm, a fullerene is a good example. If the material is present in the form of a wire or tube with a diameter in the low nanometres but a length beyond this,

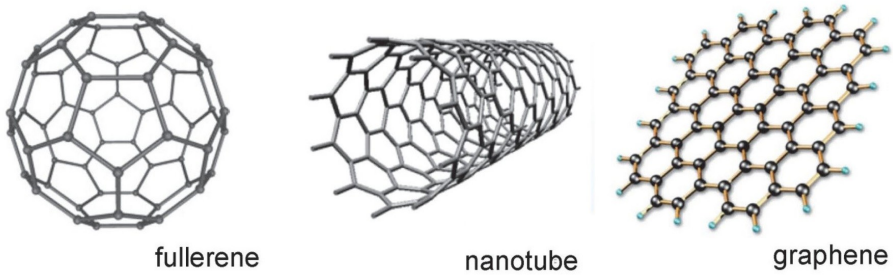

Figure 1.2: Forms of carbon nanomaterials. Source: http://sciencedge.blogspot.com, accessed on 17th of September 2018.

then we talk about a 1D material. The most prominent 1D material is the carbon nanotube, a rolled-up sheet of carbon with a diameter of 1 nm [5]. A 2D material is a sheet which is atomically thin. The most well-known 2D nanomaterial is graphene, a one atom thick sheet of carbon atoms discovered by Novoselov and Geim in 2004 [6]. Graphene is a good example to show the changes in property from its graphite bulk state to nanometre sized sheets of carbon. Whereas graphite is very brittle and is difficult to deform, the Young's modulus of graphene is over 1 TPa (graphite is 27.6 GPa). In comparison steel has a Young's modulus of 200 GPa, which is 5 times lower compared to graphene [7]. Beside the enhanced mechanical characteristics the electron mobility increases up to 200 000 $cm^2\,V^{-1}\,s^{-1}$ out-performing copper, the current standard conductive material, by a factor of 4500 [8].

Beside these by now famous structures, carbon can be found in other various forms where it has nanometre size properties:

- *Carbon aerogel* is an amorphous carbon, meaning it has not overall crystalline order, carbon is often polycrystalline in an amorphous matrix. It is a highly porous and amorphous form of carbon [9]. Particles in the is size of 3 to 20 nm are interconnected forming a porous structure. They result in a conductive network when the precursor organic aerogels undergoes a pyrolysis or carbonization step (typically above 600 degrees). The molecular structures changes to a mixture between amorphous and graphitic structures, which are highly disordered. Carbon aeorgels are used in many applications, most prominently in electrical storage applications such as supercapacitors due to their porosity, giving a high surface area and a low density, and their good conductivity for a porous network [10–13].

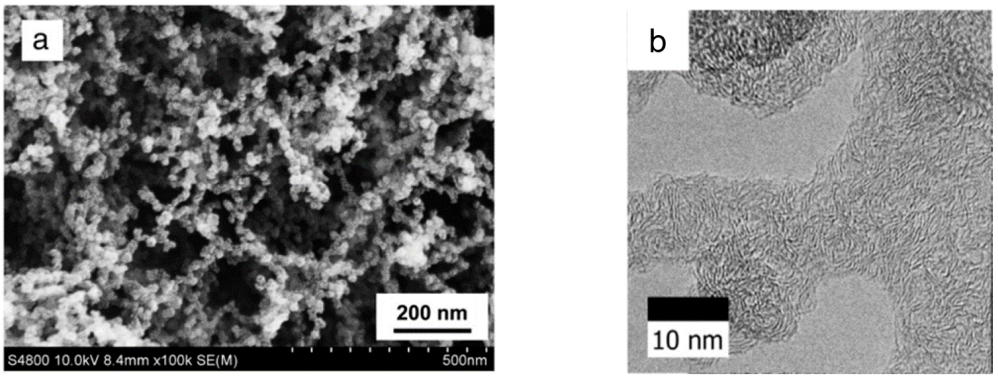

Figure 1.3: a) SEM, b) TEM image of carbon aerogel, Figures adapted with permission from Feng et al., Materials letters, vol. 65, 23-24, 2011 [14] and Wohlgemuth et al., Green Chemistry, vol. 14, 5, 2012 [15].

- *Carbon foam* is very similar to carbon aerogels [14]. The difference lies in the porous structure, whereas the aerogels form porous structures with agglomerated small particles, foam shows a higher order in mesopores with clearer defined carbon structures forming the pores. Synthesis methods are similar to aerogels and the distinction between foams and aerogels is not always clear. The carbon nanofoam investigated in this thesis should be classified as aerogel, literature has done so otherwise, therefore the carbon foam is classified as foam in this thesis.

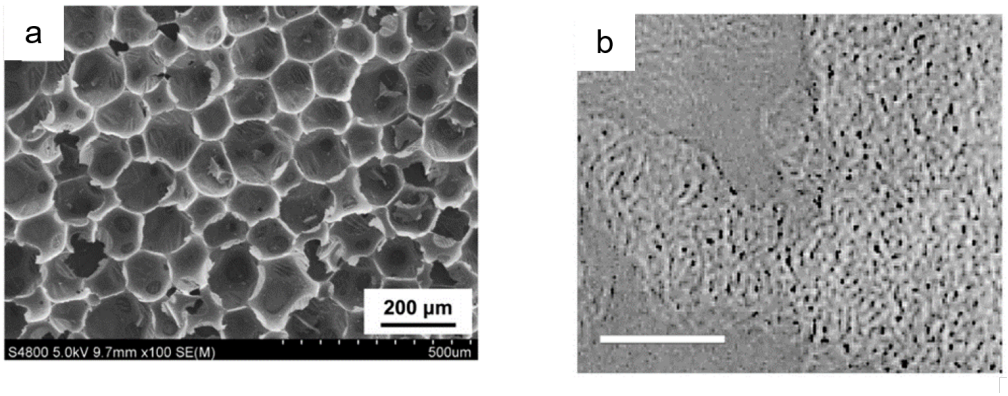

Figure 1.4: a) SEM, b) TEM image of carbon foam, Figures adapted with permission from Feng et al., Materials letters, vol. 65, 23-24, 2011 [14] and Rode et al., Applied Physics A: Materials Science & Processing, vol. 69, 7, 1999 [16].

- *Nanodiamonds* can by synthesized with various techniques: detonation technique, laser ablation, high-energy ball milling of high pressure high temperature diamond micro-crystals, plasma assisted chemical vapour deposition, autoclave synthesis from supercritical fluids, chlorination of carbides, ion ir-

radiation of graphite, electron irradiation of carbon onions and ultrasound cavitation [17]. As the name is implying the carbon lattice has a diamond characteristic but the size of the material is in the nanometre regime. The nanodiamonds keep their characteristics as a diamond in the nanometre regime. They have a superior hardness and Young's modulus, they are biocompatible, keep their optical properties, have high thermal resistivity, high electrical resistivity, good chemical stability and resistance in harsh environments. Their applications range from drug delivery, protein mimics, tissue scaffolds or surgical implants.

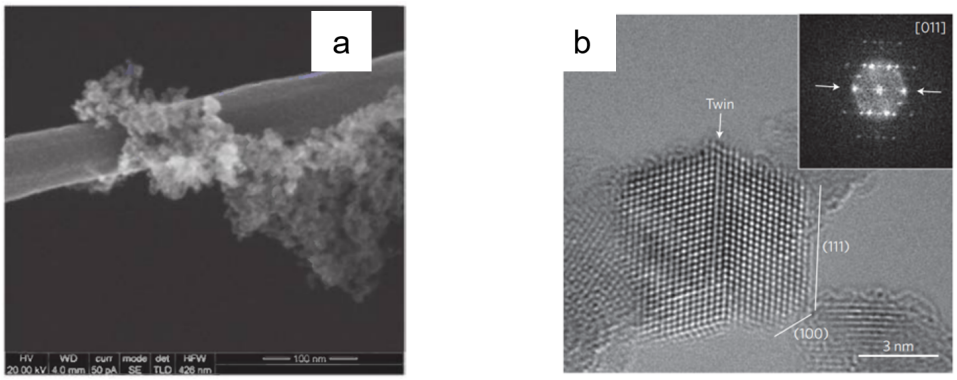

Figure 1.5: a) SEM, b) TEM image of nanodiamonds, Figures adapted with permission from Williams et al., Royal Society of Chemistry, Nanodiamond,2014 [18] and Mochalin et al., Nature nanotechnology, vol. 7, 1, 2012 [17].

- *Carbon black* is an amorphous carbon, it is the result of incomplete combustion of heavy petroleum, but it is also synthesized through thermal decomposition of hydrocarbons [19]. The difference lies in the presence or absence of oxygen during the synthesis. It has a high surface-area-to-volume ratio, which is lower than activated carbon. Its applications lie in reinforcing filler in tires and other rubber products. It is used as color pigment in plastics, paints and inks. The industrially manufactured material consists of aggregates of nearly spherical particles with a range of sized between 100 an 1000 nm. The surface can be treated by various methods to change the oxygen functional groups.

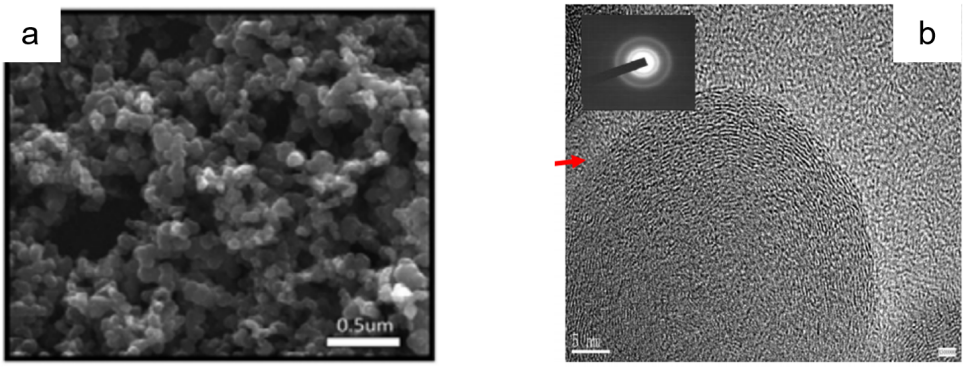

Figure 1.6: a) SEM, b) TEM image of carbon black, Figures adapted with permission from Meng et al., Journal of Materials Chemistry A, vol. 2, 44, 2014 [20] and Hu et al., Wear, vol. 305, 1-2, 2013 [21].

- *Soot* is a randomly formed particulate carbon, also called amorphous, which contains a variety of inorganic and organic impurities [19]. Soot is generally the pre-cursor for black carbon, which is the pure form of it. The formation of soot as in carbon black is the result of incomplete combustion of petrol. The simplest way to form is by dehydrogenation to atomic carbon which condense to solid carbon. On the other hand it is possible for a large hydrocarbon molecule is dehydrogenated to give soot. It is more feasible that there is a process into these two extremes containing a polymerization and hydrogenation step.

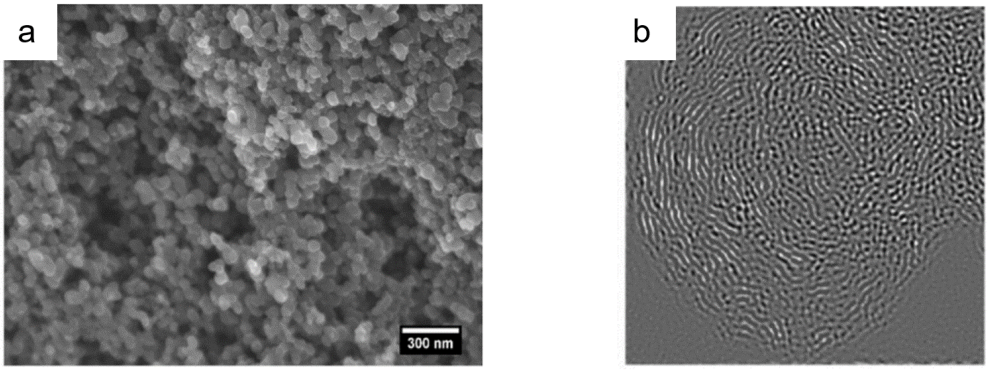

Figure 1.7: a) SEM, b) TEM image of soot, Figures adapted with permission from Esmeryan et al., Colloids and Surfaces A: Physicochemical and Engineering Aspects, vol. 529, 2017 [22] and Mueller et al., Physical chemistry chemical physics: PCCP, vol. 9, 30, 2007 [23].

- *Activated carbon* is basically an assembly of defective graphene layers [24]. Going through a carbonization step (heat treatment in an inert atmosphere

(700-1000 degrees) produces a sp2 structure. Activated carbon have a high surface area up to 3000 m^2/g due to the enhanced porosity of the material. They are typically used for adsorption process such as filtering or sensing applications.

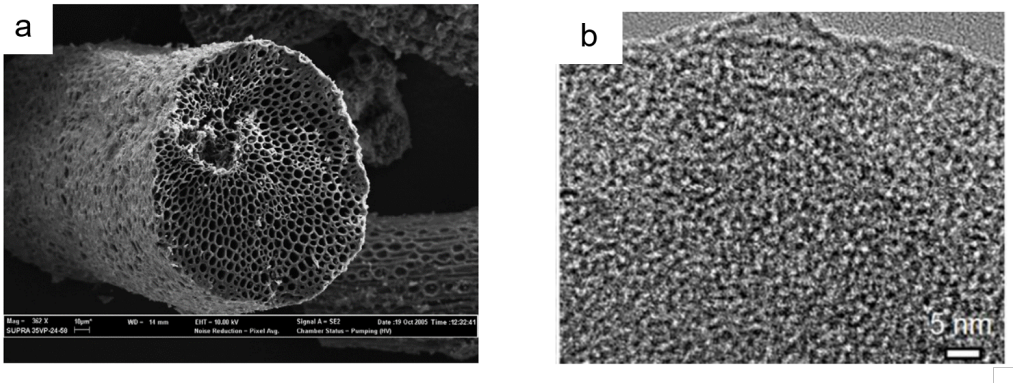

Figure 1.8: a) SEM, b) TEM image of activated carbon, Figures adapted with permission from Tan et al., Chemical Engineering Journal, vol. 127, 1-3, 2007 [25] and Zhao et al., Journal of Materials Chemistry A, vol. 3, 29, 2015 [26].

Although carbon nanomaterials are the most studied so far, there are other materials which form nanostructures. MoS_2 becomes a semiconductor only when exfoliated into its 2D form [27]. Boron nitride is an insulator with thermal properties up to 2000 $W\,m^{-1}\,K^{-1}$ when present in a monolayer [28]. Other materials identified are black phosphorous, a semiconductor with similar mechanical properties to graphene, and silicene, a one atom thick layer of silicon which has also similar properties to graphene but has a tuneable bandgap [29, 30]. Figure 1.9 illustrates the forms of further 2D nanomaterials.

1.1 Nanomaterial Applications

A lot of time has been invested in understanding the nanostructures of various materials and defining the characteristics of the materials. However to incorporate these nanomaterials into applications is an entirely different challenge. There are various ways to take advantage of the materials' properties. For instance, they can be incorporated into a composite structure to enhance a specific characteristic of the mixture. Adding graphene flakes, for example, enhances mechanical properties while reducing weight as less material is needed to achieve the same strength when

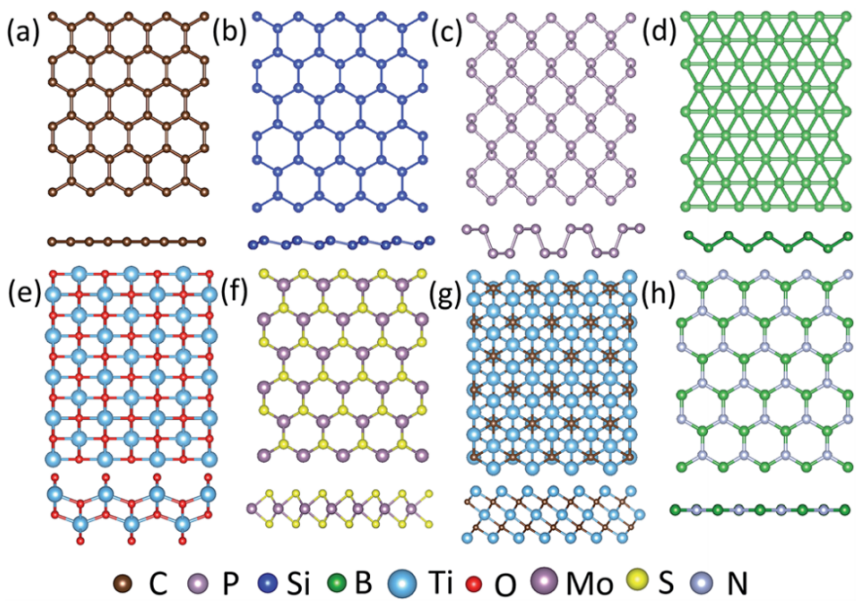

Figure 1.9: Illustration of 2D nanomaterials, a) graphene, b) silicene, c) phosphorene, d) borophene, e) TiO_2, f) MoS_2, g) Ti_3C_2, h) h-BN, Figure adapted with permission from Shi et al., Journal of Materials Chemistry A, vol. 5, 8, 2017 [31].

a material with stronger mechanical properties is incorporated. Boron nitride can be used to enhance thermal capabilities while also reducing weight.

There are other applications where the properties of the nanomaterials are exploited directly. Often the performance of the nanomaterials are able to exceed the bulk material's performances in the same application.

A good example of such an application is gas sensing. Gas sensors measure the concentration of a certain analyte in its gaseous form. There are many industries where gas sensors are important. There are safety applications, for example, the detection of poisonous gas leaks on oil rigs or in mines. Gas sensors can be applied in medical environments to diagnose health issues measuring the different components in a patient's breath. Air pollution measurements require devices able to measure the smallest concentrations of pollutants in the air.

Nanomaterials work well in gas sensing applications because of their high surface to volume ratio. In order to measure analytes in the air they need to adsorb onto the nanomaterial. Because of their high surface area there are a lot of adsorption sites present for gases to attach to the nanomaterials. Due to their low volume even the smallest changes on the surface will influence the properties of the entire film. The combination of many adsorption sites and the sensitivity to small changes makes

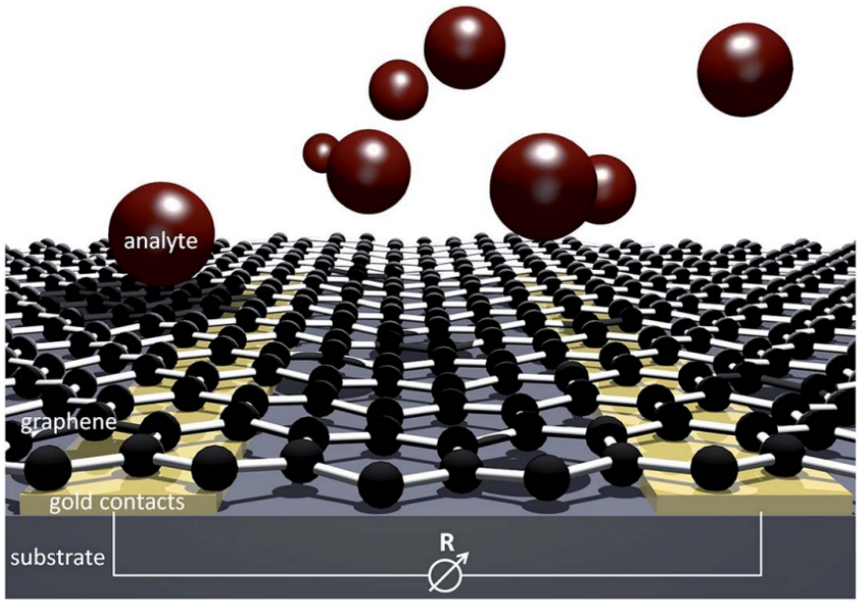

Figure 1.10: Illustration of graphene in a gas sensor structure, Figure adapted with permission from Zopfl et al., Faraday discussions, vol. 173, 2014 [32], Published by The Royal Society of Chemistry.

them ideal for measuring small differences in an analyte's concentration in the air. For example graphene is able to detect individual gaseous molecules [33].

During the adsorption process of a gas, an electron is typically either donated or accepted by the analyte. This influences the electrical properties of the material. Many device architectures have been investigated to measure this change of property. By using a chemiresistor structure, a variation in resistance can be measured when the active layer interacts with an analyte, illustrated in figure 1.10. Alternatively, back-gated transistor structures allow the nanomaterial, working as the source-drain electrode, to interact with its environment. Shifts in the transistor's threshold voltage are monitored as they relate to a present concentration of an analyte [34]. All of these devices are able to monitor small concentrations of analytes and have quick response times.

Despite these promising characteristics, however, there are currently no nanomaterial based devices commercially available in any field. Even though the performance of these materials is ground-breaking there are still many problems related to their synthesis. The quality of the material strongly influences the performance. Production processes need to yield pristine materials in large volumes. To date,

there has been no fabrication method which can combine these requirements. Nevertheless, materials like graphene and boron nitride have started to emerge into the market. Graphene, for example, can be bought in individual, high quality sheets in low volumes or in larger quantities but with poorer quality.

Although these materials are readily available they still are not being incorporated into commercial device architectures. The insertion of the nanomaterials into composites is already possible as it requires simple mixture of two components. Adding nanomaterials into chip size applications is more challenging. Current synthesis methods do not allow materials to be directly deposited onto electrode structures. Often materials are synthesized on a substrate and photolithography and physical vapour deposition is used to deposit electrodes on top of the material enabling an electric readout. Not only is lithography an expensive method of manufacture, it can also alter the properties of the nanomaterials decreasing the performance. To push nanomaterials into device architectures, new fabrication processes need to be developed. They must allow the nanomaterials to be controllably incorporated in a bottom-up approach. For a successful commercialization these fabrication steps should be scalable without altering the nanomaterials' characteristics.

1.2 Aim of this thesis

This thesis has several goals related to applications of carbon nanomaterials. On the one hand, to investigate gas sensor device architectures for currently commercially available graphene. The aim is to create a process flow with only scalable manufacturing methods and create a device which incorporates commercially available graphene.

The second goal is to develop a fabrication process which directly deposits nanomaterials on to readout electrodes. This facilitates the incorporation of nanomaterials into device structures as the fabrication process becomes less complex. The aim is to create direct deposition methods and evaluate the deposited materials in actual applications.

1.3 Organization of the thesis

This thesis focuses on the application of high surface area carbon nanomaterials. The materials investigated are graphene and carbon nanofoam (CNF). Applications studied are gas sensor devices and supercapacitor electrodes for energy storage.

The thesis is written in the style of a papers style thesis. The work done has been published in various journals in concise form. These publications are incorporated into the thesis as individual chapters.

This chapter aims to give the reader a broad introduction into the world of nanomaterials. An introduction is made into the gas sensing applications which is the major application reported in this thesis. It also introduces the current challenges in the applications of nanomaterials. The first chapter is also intended to introduce the reader to the techniques used during the research. A broad introduction is given into the scalable methods used during fabrication. The main techniques used are laser based. The setup of the laser machine used is presented. A deposition technique called Langmuir-Schaefer (L-S) is presented. Beside the fabrication methods, the nanomaterials were characterised using various techniques. The techniques which contributed the most are presented: Atomic Force Microscopy (AFM), Kelvin Probe Force Microscopy (KPFM), Scanning Electron Microscopy (SEM) and Cyclic Voltammetry (CV). A paragraph is dedicated to the process called diffusion-limited aggregation. The carbon nanofoam formation is based on this process.

The second chapter is a literature review. The review is intended as an introduction for someone new to the field. It covers the methods of graphene and carbon foam synthesis. A section focuses on the synthesis method for graphene used in this work. The material, as received, is compared to materials presented in the Literature. Reported results of carbon foam synthesis are summarised, giving a comparison to the CNF used in this work.

An overview is given into the application of graphene and carbon foam into gas sensing. Various device architectures are presented and sensing mechanisms are shown for both graphene and carbon foam. Section 2.5 reports on work done by others on carbon foams in supercapacitor applications.

Chapter three provides an introduction to the gas sensing application. It presents the measurement setup used for the gas sensing experiments in this work. It describes a method of creating a device by industrial laser processes applied to commercially available graphene deposited by L-S. Basic studies of these percolating graphene films are presented where the limit of detection is determined as well as the reproducibility of the device response.

Chapter four reports, further, on the device architectures of chapter three, determining the sensing mechanism within the created device. It is a manuscript published in ACS Applied Materials & Interfaces. Again the fabrication flow is illustrated before the application as a gas sensor is discussed. In the next step the sensing mechanism is determined using two analyte gases which cause opposing resistance changes. Their interaction with the sensing film is analysed with Raman and KPFM showing the opposing behaviour of the gases. Comparing characterisation with actual gas exposures leads to the conclusion of the sensing mechanism in percolating films. We correlate the sensing mechanism to a change at the contacts of the graphene flakes in the percolating system. Further, we are able to experimentally calculate adsorption energies at the edges of the flakes. Knowing that the measured signal originates from a change at the edges allows us to compare the measured values with simulated values in literature.

Chapter five presents the direct deposition of CNF onto electrode structures and a pre-study towards gas sensing using various humidity environments. This manuscript is published in ACS Applied Nanomaterials. The chapter starts with the characterisation of the pre-cursor material before the deposition technique is presented. The deposited carbon nanofoam is characterised using microscopy techniques. Sputtering as a functionalization method is presented. The functionalization has a percolative behaviour. Two different behavioural regimes around the percolation threshold are presented. The functionalized material is exposed to a changing humidity environment in its three states, namely below the percolation threshold, at the percolation threshold and above the percolation threshold. Its conductivity change, when exposed to the analyte, shows opposite behaviour above and below

the percolation threshold. At the percolation threshold the sensitivity to changing humidity is lost. The sensing mechanisms in the three cases are presented.

Chapter six investigates CNF in supercapacitor applications. It is a manuscript published in ACS Omega. The precursor material is characterised again using SEM, AFM and Raman techniques. A fabrication process, similar to the one presented in chapter 5, is illustrated but a water transfer step is added into the process flow. SEM images show a change in morphology during the water transfer. We show, using CV measurements, that this change in morphology more than doubles the weight dependent capacitance. Using Raman spectroscopy we show that the enhanced capacitance originates not only from different pore size distributions but is a combination with internal compressive stress. We relate the change in capacitance to the interaction of capillary forces and the CNF during water transfer.

The last chapters give a conclusion and an outlook to the work done in the thesis. The results are summarized and put into context with the problems stated in the introductory chapter. The outlook presents work and ideas to be done based on the experience gained by research for this thesis.

1.3.1 Status and contributions of publications

The status of the publication manuscript is as follows:

- Title: Edge Selective Gas Detection using Langmuir Films of Graphene Platelets, Status: published in ACS Applied Materials & Interfaces, DOI: 10.1021/acsami.8b05105, Contribution from S.N.: Design, concept, device fabrication, experimental setup and measurement, material characterisation, data analysis, writing manuscript

- Title: Percolating Metallic Structures Templated on Laser-deposited Carbon Nanofoams derived from Graphene Oxide: Applications in Humidity Sensing, Status: published in ACS Applied Nano Materials, DOI: 10.1021/acsanm.8b00246, Contribution from S.N.: Design, concept, device fabrication, experimental setup and measurement, material characterisation, data analysis,

writing manuscript

- Title: Carbon Nanofoam Supercapacitor Electrodes with Enhanced Performance using a Water Transfer Process, Status: published in ACS Omega, DOI: 10.1021/acsomega.8b02118, Contribution from S.N.: Design, concept, device fabrication, experimental setup and measurement, material characterisation, data analysis, writing manuscript

1.4 Technology used during the thesis

Various techniques have been applied during this thesis. Here an overview is given of the techniques contributing most.

1.4.1 Laser processing

Figure 1.11 shows the setup of a MSV-101, a laser processing tool manufactured by M-Solv from off-the-shelf components. It includes various components. The most important ones are the laser, the optics, the scanner and the chuck. Together these components form a basic laser processing setup. Each component contributes to the functionality of the setup.

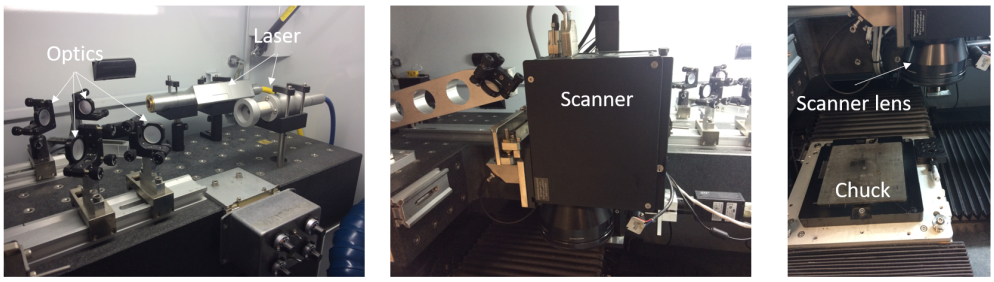

Figure 1.11: MSV-101 laser processing tool setup.

Laser stands for "light amplification by stimulated emission of radiation" and is a phenomenon that does not naturally occur in nature. A laser device emits a coherent beam of light. Lasers exist which emit at various different wavelengths from deep ultraviolet up to high into the infrared [35].

The lasers on the MSV-101 are pulsed, which is an additional adjustable parameter to the laser process. A pulsed laser emits for only a fraction of a second at a

time. Available pulse duration range from microseconds down to picoseconds. The laser (20 W Multiwave MOPA-DY with a wavelength of 1064 nm) on the MSV-101 has a range of approximately 200 ns to 10 ns available from the adjustable pulse-duration fibre laser. The pulsed laser also enables us to choose the frequency between 10 and 200 kHz at which the pulses are emitted. Pulse duration changes the way the laser interacts with a material. The shorter the pulse length the less heat is generated in the surrounding substrate of the laser interaction point [36].

Frequency, together with beam scanning speed, change the number of shot overlaps, during ablation processes. This determines the amount of energy the substrate is exposed to.

Another way of controlling the amount of energy reaching the substrate is by altering the power settings on the laser, which changes the pulse energy. Once the laser beam leaves the laser it is directed to the scanner via optics. The optics are coated to reflect the laser beam with almost no losses. Various things can be achieved with different optics. A mirror steers the beam into a disred direction and a telescope changes the beam size. Attenuation can be achieved using a polarizer and a waveplate.

The laser beam is guided through the optics into the scanner. The scanner is made of two rotatable mirrors which reflect the laser beam coming in. The freedom of movement of the mirrors allow them to guide the laser into any location within the scan field of the scanner. This means the laser can follow complex forms in a 2D plane. The laser leaves the scanner through a f-theta lens, which is designed using mutliple lenses so the focal spot is able to follow a plane and not the curvature of a single lens. The scan field, defined as the maximal area the laser spot can be focused to by the lens, is linearly proportional to the focal length of the lens. This combination of a focused laser beam and the capability to form complex patterns is a requirement for laser materials processing including ablation.

The final component of the system is the sample holder or chuck. The chuck is mounted onto a x, y linear stage stack to extend the processing area beyond a single scanner field, which is defined by the scanner properties and can achieve the size of an A4 paper, but is typically in the 10s of cm. The chuck needs to be planar and parallel to the focal plane of the scanner lens to assure the laser remains in focus

over the entire processing area.

1.4.1.1 Laser ablation

The mechanism of laser ablation depends on the characteristics of the material to be ablated and the laser characteristics to do so. Material properties include absorption, thermal conductivity, thickness and surface roughness. The laser characteristics have been discussed in the previous section.

Laser ablation is defined as removal of material after the exposure to an incident light source. The absorption of the laser induces a transfer of photon energy to energy in the material. Ablation occurs if the absorbed energy in the material exceeds the binding energy of the material resulting, in removal of the material [37]. Removal occurs in the form of vaporisation, evaporation or explosive material. Beside removal of the material the laser can also create new bonds within the material or change its chemical composition or structure [38–40]. Other effects occurring include melting, recasting or redeposition of ejected material.

When a targeted material is illuminated with a laser with wavelengths in the visible light or with higher energy, the entire energy is transferred to the electrons in the material. The electrons are not in equilibrium anymore and need to dissipate the excess energy non-thermally [41]. The non-thermal process occur through electron collision (electron - electron scattering) where kinetic energy is transferred, typically occurring in a femtosecond regime [37]. If the electrons are energetic enough they overcome the Fermi energy, which allows the ejection from the material. This leads to a removal of ions, as the depletion of electrons induces an electric field which then pulls ions out of the material [37]. The resulting ejection of material is a plume of plasma on the target. Thermal dissipation occurs by an energy transfer into the lattice vibrations, this transfer typically happens within picoseconds. The ejected material from thermal processes are a stream of vapour or molten droplets of material. Laser wavelengths with lower energy cause thermal dissipation as the laser excites lattice vibrations.

1.4.2 Langmuir - Schaefer

Figure 1.12 presents the basic procedure to create and pick up a percolating film [42]. A material in the form of platelets or small particles is dispersed in a low boiling point solvent. The dispersion is drop cast into a water sub-phase where the low boiling point solvent spreads on the water surface and evaporates. The platelets remain behind floating on the surface of the water, held by the surface tension. In order to increase the density of the platelets on the surface more material is drop cast into the sub-phase. Movable horizontal barriers on top of the trough then compress the film. During compression the surface tension is monitored, using a Wilhelmy plate and piezo, via isotherms allowing repeatable formation of films. The isotherms have three distinguishable regions where, during compression, three different slopes are visible (see paragraph below for explanation of the slopes). The steeper the slope the denser the film [43].

When the desired surface tension is reached the barriers stop compressing and a substrate is lowered vertically toward the water sub-phase until it touches the film. The substrate is then slowly withdrawn upwards with platelets sticking to it until it is fully removed from the water sub-phase and left to dry. The more hydrophobic the substrate the better the transfer.

This technique found its way from using only amphiphilic molecules, which are surfactants, to use with 2D nanomaterials. L-S is an adaption from the Langmuir-Blodgett (L-B) technique which has a different substrate holder [44].

The L-B technique is well understood with the deposition of surfactants. The molecules float on the water sub-phase with their nonpolar tail in the air and the polar head at the air-water interface. The surfactants undergo a random motion at the water air interface, similar to the Brownian motion of gas molecules. Compressing the surfactants limits this motion in a similar way to a phase transition from gaseous form into the liquid form. Further compression leads to an analogue of a solid phase. Therefore three different regimes are seen in the isotherms and are called gas-, liquid- and solid phase. L-B has been used to create monolayer films of molecules on various different substrates. An example application of the process is antireflection coatings on glass [44]. The nomenclature of the isotherm regimes has been taken over to the 2D film formation [43]. Figure 1.13 illustrates an example of

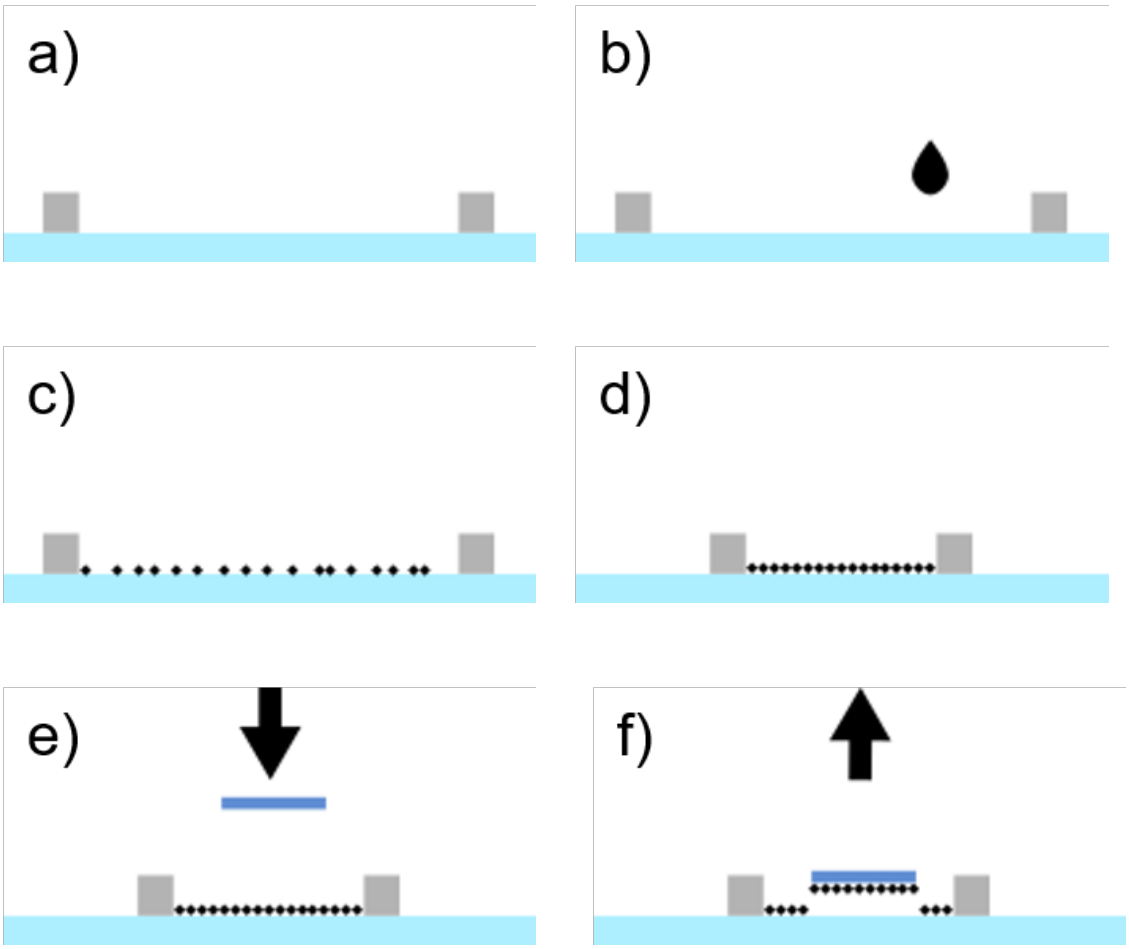

Figure 1.12: Schematic of the Langmuir - Schaefer process, a) a water sub-phase with two movable barriers is the starting point, b) a nanomaterial platelet dispersion in a low boiling point solvent is drop cast into the water sub-phase, c) the solvent evaporates leaving the platelets floating on top of the water sub-phase, d) barriers compress platelets to form a continuous film, e) a substrate is horizontally mounted and moved vertically until it touches the film, f) substrate is lifted taking the film with it.

an isotherm with the different regimes.

1.4.3 Atomic Force Microscopy

AFM is a well-known microscopy technique based on Van-der-Waal forces interacting with the tip of a cantilever [45]. It is typically used to determine the thickness or roughness of films as it is very accurate in the vertical direction. Other applications are for the determination of mechanical characteristics of a sample or the manipulation of individual molecules. AFM does not need special sample preparation and does not have special sample requirements. It can be operated in three different

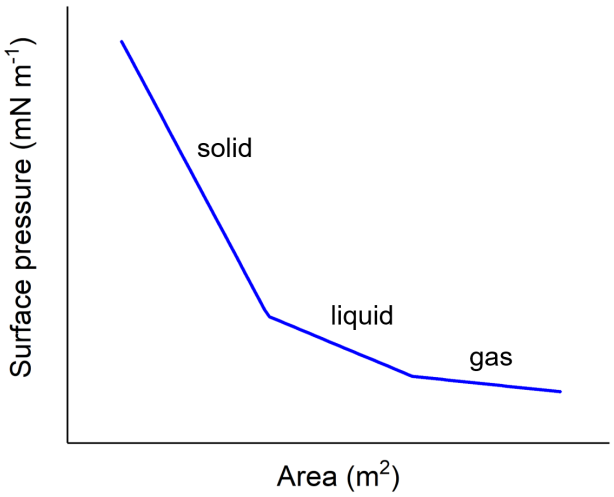

Figure 1.13: Langmuir-Schaefer isotherm example.

modes: tapping mode, contact mode and non-contact mode. Tapping mode and constant height mode allow measurements of the surface without actually touching the surface, leaving the samples measured without any damage.

An AFM cantilever has a tip which has a diameter of only 2 nanometres. Due to the size of the tip it is able to interact with the Van-der-Waal forces of the sample which deflects the cantilever. The Van-der-Waal forces only act when molecules are in very close distance, as seen in the diagram in figure 1.14, it is therefore crucial to bring the tip in close distance to the substrate. The tip gets as close as 0.1 nm to the substrate. In this regime forces in the pN regime are acting on the tip. The tip have a low spring constant in the range of 0.01 N/m, therefore they get deflected in the nanometre regime when the Van-der-Waals forces are applied which can be picked-up using a laser pointed onto the cantilever is reflected and guided on to a photodiode. Movements of the tip are registered by the photodiode as the laser is moved with the tip. Knowing the spring constant, the deflection of the tip can be calculated which can then be correlated to the topography of the sample the cantilever is scanning. A piezo crystal is used to actuate the cantilever via vertical movements, therefore it is not only actuation but it also provides a feedback loop for the different modes. Figure 1.15 illustrates the AFM setup.

Figure 1.16 shows a schematic of the three different modes of the AFM. In non-contact mode the cantilever is actuated with a piezo. The piezo actuator and the

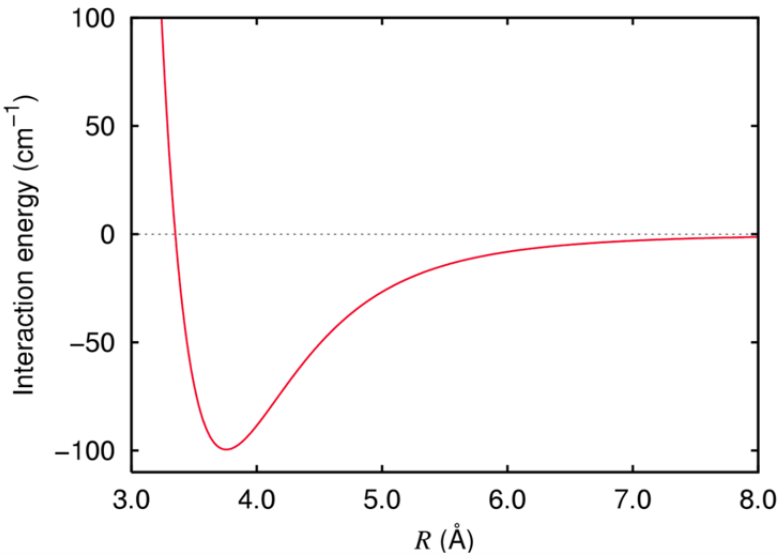

Figure 1.14: Van-der-Waals forces depending on the distance between atoms, Figure adapted from https://en.wikipedia.org, accessed on 17th of January 2019.

cantilever are in feedback. The cantilever is supposed to not move while scanning the sample if operated in constant height mode. The forces interacting between the sample and the tip are maintained throughout the scan. As soon as it is moving the piezo raises or lowers the tip to prevent movement. Measuring the piezo actuation represents the topography of the sample scanned.

In contact mode the tip of the cantilever is in direct contact with the sample and is scanned. The cantilever deflects according to the surface topography, the piezo assures the contact with the sample and the movements of the cantilever are read out with the laser and the photodiode.

In tapping mode the cantilever is actuated into vibration by the piezo. In order to have a large movement of the tip it is operated at its resonance frequency. This facilitates the measurement of the topography as the resonant frequency is acting significantly to the applied forces. During the movement of the tip, at its lowest deflection point it usually sits directly on the sample. However it can also operate in non-contact mode. The cantilever in resonance is scanned across the sample and the amplitude of the vibration changes when the sample's topography changes. It will be smaller when the topography is raised and larger when it is lowered.

The modes are chosen according to the properties of the sample. Contact mode is used on very planar samples as steps can destroy the tip of the cantilever or the tip destroys the sample. The measurements are more accurate compared to the other

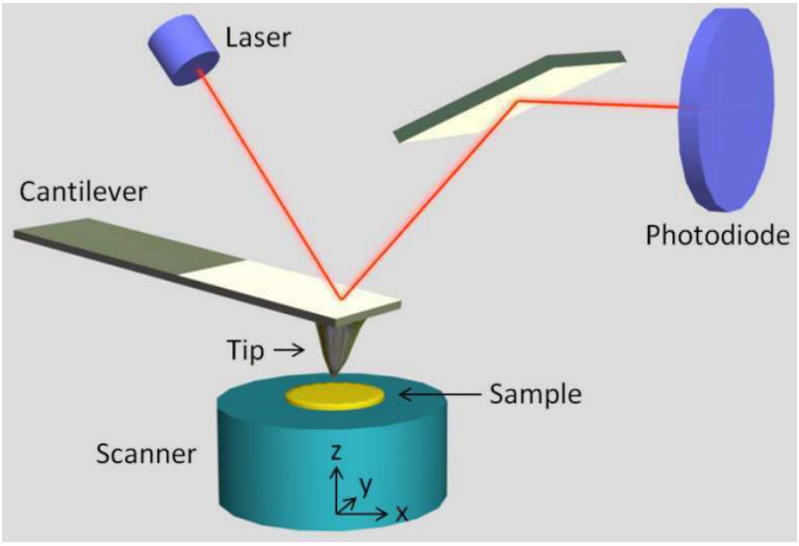

Figure 1.15: Illustration of AFM setup., Figure adapted from [46].

modes. Non-contact mode is used for soft samples, as the tip would compress the sample when interacting with it and falsify the measurement. Tapping mode is the most common mode. It is able to measure most of the samples accurately and the tip is not endangered by varying substrate heights as the tip is only touching the sample in small spots and is not dragged along. AFM is a powerful technique to measure film thickness and roughness accurately. It is also a very delicate technique which requires experience because there are many parameters that need to be considered to get a successful measurement.

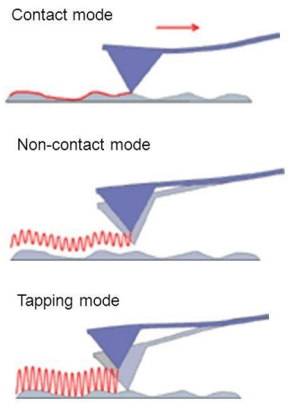

Figure 1.16: Illustration of AFM modes, source: http://slideplayer.com, accessed on 17th of September 2018.

1.4.4 Kelvin Probe Force Microscopy

KPFM is a mode in an AFM setup. Both the tip and sample are required to be conductive. Using KPFM, the contact potential difference (CPD) can be measured which can be related to the work function of the sample because the work function of the tip is a known constant [47]. The CPD voltage V_{CPD} is defined as

$$V_{CPD} = \frac{\phi_{tip} - \phi_{sample}}{-e} \tag{1.1}$$

where ϕ_{tip} is the tip's work function, ϕ_{sample} the sample's work function and e is the electronic charge. The work function is defined as the minimum energy required to remove an electron from its core into the vacuum immediately outside of the atom [48]. This allows the measurement of various electronic properties of a sample, including doping [47].

A DC bias is applied to the substrate where the cantilever has an AC bias at its resonant frequency. The tip and the sample form a capacitor and a force acts between the sample and the tip due to the electrostatic field. Differences in the DC bias and the AC potential let the cantilever vibrate. An additional DC bias is applied to the cantilever by applying a voltage to minimize the cantilever's vibration. This applied voltage represents the CPD between the tip and the sample. Operating the AC bias at the cantilevers resonant frequency improves the sensitivity significantly.

Figure 1.17 illustrates the energy levels principals behind the method. When the tip and the sample are far away from each other the vacuum level of both systems are aligned. In electrical contact the Fermi levels of both systems align, resulting in a shift of the relative shift between the vacuum levels by an offset. This offset is the contact-potential-difference. Applying an external voltage with same amplitude as the CPD energy difference aligns the vacuum levels again. The work function is then calculated from the CPD values recorded during the measurement when the work function of the tip is known (normally given by the supplier).

KPFM is a powerful technique to measure local doping, as doping changes the surface potential and therefore the CPD. In the case of gas sensing the absorbants add or remove charges on the surface which changes the energy level of the active

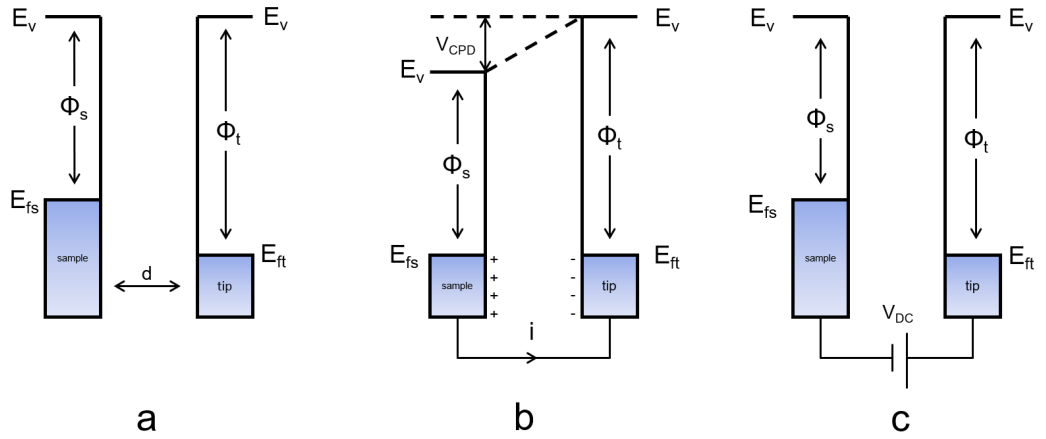

Figure 1.17: Electronic energy levels of the sample and AFM tip for three cases: (a) tip and sample are separated by distance d with no electrical contact, (b) tip and sample are in electrical contact, and (c) external bias (V_{dc}) is applied between tip and sample to nullify the CPD and, therefore, the tip-sample electrical force. E_v is the vacuum energy level. E_{fs} and E_{ft} are Fermi energy levels of the sample and tip, respectively.

material. Accurate measurements are not easy to make as many parameters need to be optimized before a successful measurement can be obtained.

1.4.5 Scanning Electron Microscopy

SEM creates an image of a surface using a focused electron beam which is scanned in a raster along the surface of a sample. The electrons hitting the sample interact with it, creating various phenomena which can then be detected. Figure 1.18 illustrates the types of radiation induced by the focused electron beam source and their emission regions. To create an image of a surface, backscattered electrons or secondary electrons are detected. Whereas the secondary electrons' origin lies within 10 nm on the surface the backscattered electrons originate from within 1 μm in the sample. Energy selective detectors are able to distinguish between the two different electron signals. Amplification and combination of the signals can be related back to the topography of the sample. State-of-the-art SEMs have a sub-nanometre resolution. The created images are basically a difference in "brightness", mostly originating from a difference in the number of emitted secondary or backscattered electrons. Secondary electron emission rate strongly depends on the incident angle of the electron beam. A perpendicular incident angle generates the least secondary electrons and

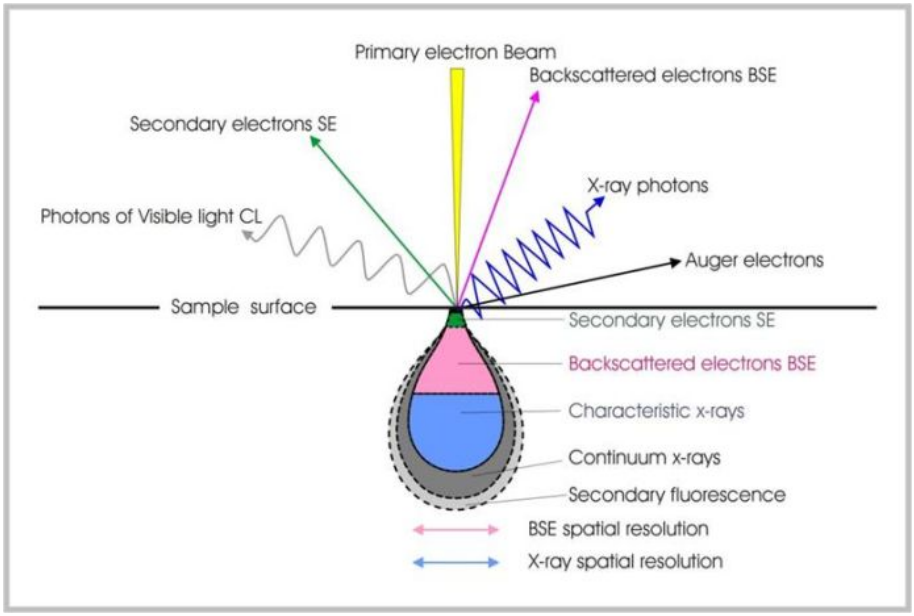

Figure 1.18: Origin of electron irradiation in SEM. Figure source from https://www.gla.ac.uk, accessed on the 17th of September 2018

the emission efficiency increases with decreasing incident angle. A small beam size and the ability to correlate the detected secondary or backscattered electrons with the beam position, results in an accurate image of the surface topography. These images can be used to determine the size of features on the sample surface but not the thickness [49].

X-rays and Auger electrons are also generated by the electron beam. These can be used to determine the chemical composition of the sample with the proper detectors.

SEM requires conductive samples in order to achieve high resolution images as grounded non-conductive sample create a charging effect which repel/deflect electrons and distort the image. A conductive coating can be applied to non-conductive samples in order to image the surface of a sample.

1.4.6 Raman spectroscopy

Raman spectroscopy is able to observe vibrational, rotational and other modes in a system. It uses inelastic scattering, which is also called Raman scattering, of monochromatic light which is usually provided with a laser to the sample. The photons interact with the lattice movements which results in a up or down shift of the laser photons. The weak signal is filtered out of the Rayleigh scattered light and

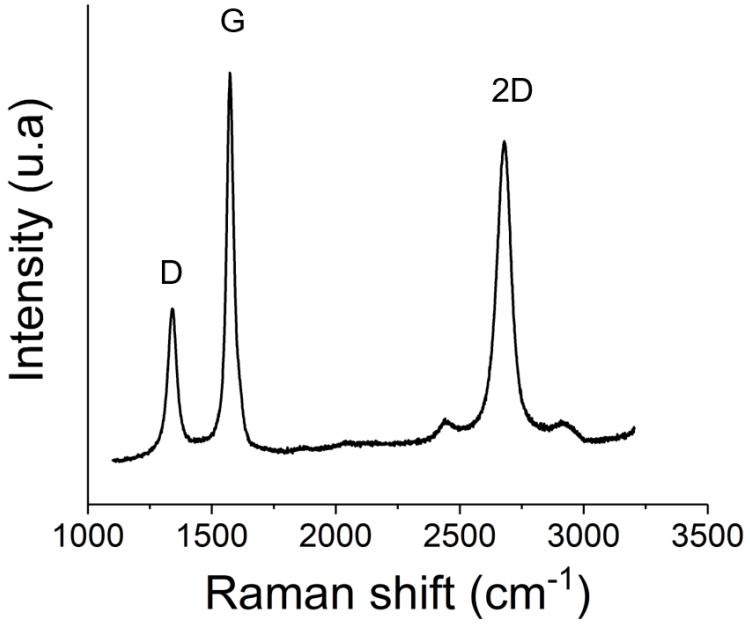

Figure 1.19: Labled Raman spectrum of Cambridge Nanosystems graphene.

collected in a detector.

Raman is specially powerful with carbon materials as there are not many peaks in the spectrum, which can be associated with various properties of the material. In the case of graphene three peaks are of special interest. Pristine graphene only has two peaks around 1580 cm^{-1} and 2600 cm^{-1} As soon as the graphene has defects and increases in number of layers another peak appears around 1340 cm^{-1}. These three main peaks are historically called D, G and 2D peak in increasing wavenumber. The intensity between the D and G peak gives and indication of how many defects are present and if the ratio of the 2D peak and the G peak is higher than one then a single layer of graphene is present. Moreover up or down shifts can be associated with changing characteristics of the materials like stress or doping.

1.4.6.1 Calculation of adsorbents from shift in G-peak

It is possible to calculate the number of the adsorbents from the shift in the G-peak of the Raman spectrum. Kim et al. [50] demonstrated this for the adsorption of HNO_3 on graphene. The calculation they show can be used for any adsorbent. In chapter 4 we use this calculation to calculate the amount of NH_3 adsorbants on graphene. The calculation and the constants are taken from Kim et al. [50]:

$$\hbar \triangle \omega_G = \alpha' |\epsilon_f| = \alpha' \sqrt{n_d \pi} \hbar v_F \tag{1.2}$$

where $\hbar$ is the reduced Planck constant, $\triangle \omega_G$ is the difference in Raman shift in angular coordinates ($\omega[s^{-1}] = 2\pi\upsilon[cm^{-1}]c_0[ms^{-1}]$ where υ is the Raman shift and c_0 is the speed of light), α' is a constant (4.39 10^{-3} at 0K), n_d is the number of molecules adsorbed per area and $\hbar v_F$ is given as 5.52 eVÅ.

1.4.7 Supercapacitor

A supercapacitor works on the same principle as a regular capacitor, which is characterised by the equation

$$C = \epsilon \epsilon_0 \frac{A}{d} \tag{1.3}$$

where C is the capacitance, ϵ the dielectric constant of the insulator between the plates, ϵ_0 the dielectric constant of vacuum, A the surface area and d the distance between the plates.

An ultra-high surface area and a small distance between the opposite charges sums up the characteristics of a supercapacitor. The surface area can be increased by using a very porous material which has a large surface to volume ratio. Carbon nanomaterials fulfill these requirements as they are conductive as well, graphene has a theoretical surface area of 2000 m^2 per gram. In order to decrease the distance between the opposite charges the electrodes are usually immersed in a liquid with added electrolyte, nowadays also solid state electrolytes are available. Immersing a solid into a liquid form a double layer at the surface of the solid. The solvent's molecules cover the entire surface area of the electrodes forming an atomically thick layer (inner Helmholtz plane). When a potential is applied the electrolytes in the solvent are attracted by the opposite charge on the electrode and move towards it. In a perfect supercapacitor the ions cannot penetrate the double layer. A charge accumulation is taking place at the electrode with only an atomically thick layer separating them (outer Helmholtz plane). The distance between the charge layers

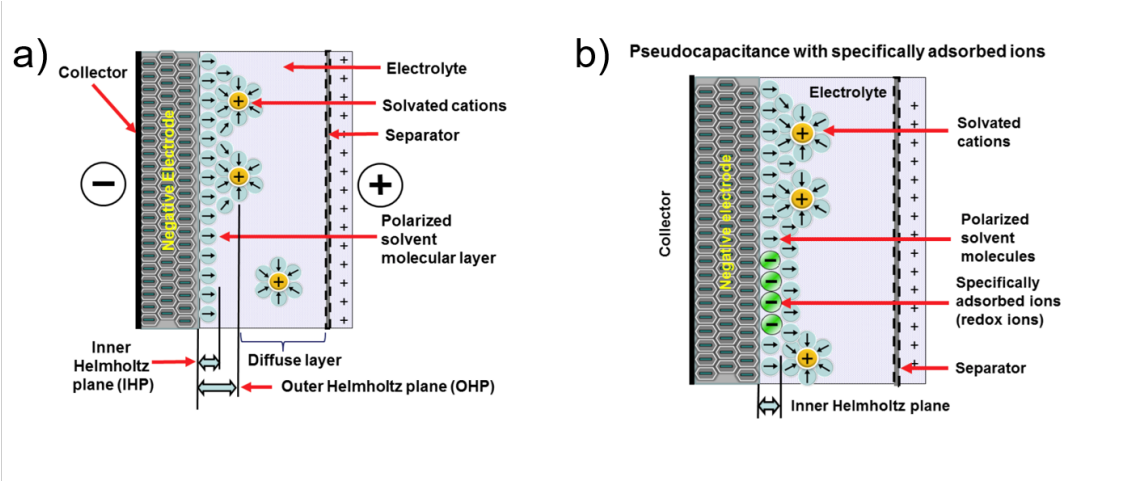

Figure 1.20: Supercapacitor schematic, a) concept of double layer effect with solvent molecules separating electrolyte ions, b) ions penetrating double layer resulting in redox reactions with the electrode. Source: https://en.wikipedia.org/wiki/Supercapacitor, accessed 15th of January 2019

is therefore atomically thin and boosts the capacitance. Figure 1.20 illustrates the double layer effect and the pseudocapacitance.

The double layer can in some areas be penetrated by the electrolyte ions and directly interact in a redox reaction with the electrode. These reactions can boost the capacitance when used correctly. This contribution is usually referred to as faradaic capacitance or pseudocapacitance and is visible in the cyclic voltammetry in the shape of peaks.

1.4.8 Cyclic Voltammetry

A CV measurement consists of a three electrode structure, the working electrode, the counter electrode and the reference electrode immersed in a solvent containing electrolytes (see Figure 1.21). A potential is applied between the reference electrode and the working electrode. The current between the counter and the working electrode is measured. A ”potential window” is applied where the voltage is swept from minimum to maximum and back. This is repeated over as many cycles as required [51].

CV is also used as a first characterisation step for supercapacitor electrodes. Its easy setup allows testing of various solvents, electrolytes and electrode materials in a short amount of time. From the results, the gravimetric capacitance can be estimated if the mass of the sample is known by integrating the electric current in

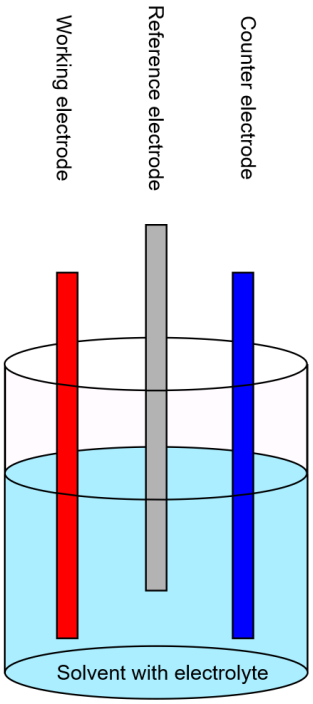

Figure 1.21: Illustration of CV measurement setup.

the CV measurement from the negative to the positiv potential limit and divide it by twice the potential window and the mass in order to obtain the gravimetric capacitance:

$$C_G = \frac{1}{2m(V_2 - V_1)} \int_{V_1}^{V_2} I(E)dE \tag{1.4}$$

where C_G is the gravimetric capacitance, m the mass of the measured electrode, V_i the potential window limits and $I(E)$ the measured current during the CV measurement. A supercapacitor electrode should have a box like current when cycled through the voltage window, meaning a quick change in current at the beginning of the voltage window which then remains constant through the entire window. Ions of the electrolyte form a double layer capacitance on top of the electrode. The ions are separated by molecules of the solvent from the working electrode. Because the distance between the ions and the working electrode is one solvent molecule, the induced capacitance is large. Increasing the surface area leads to enhanced capacitive properties, hence the term supercapacitor.

Many characteristics of a supercapacitor electrode can be analysed using CV.

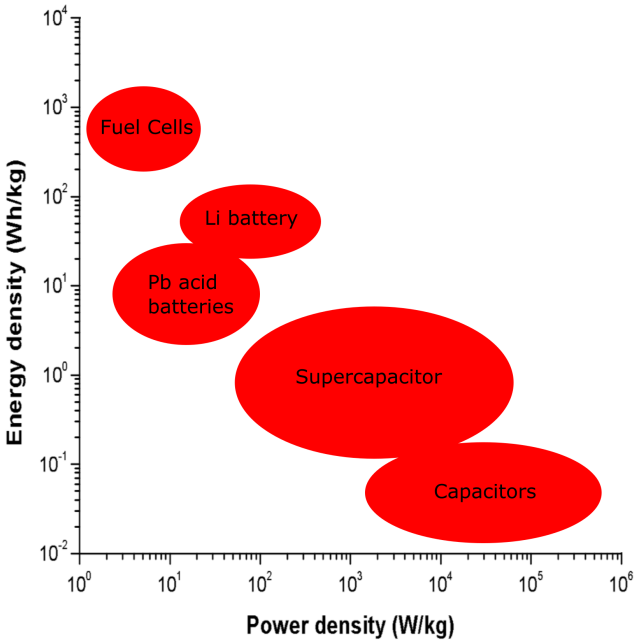

Figure 1.22: Ragone plot showing energy density and power density of different energy storage methods.

Box like currents indicate the pores in the electrodes are readily accessible and that there is good charge propagation through the electrode. This means upon an applied potential the charges accumulate at the interface very rapidly and stay stable over the potential window allowing quick charging. Moreover the ideal scan rate, which is the charging and discharging time, can be determined by changing the speed of the potential sweep. This means the optimal parameters in which an electrode needs to be operated can be determined. Figure 1.22 shows the comparison between normal capacitors, supercapacitors, batteries and fuel cells. Whereas capacitors have a high power density they have a low energy density, this means they can provide a large amount of power over a short period of time. The battery or fuel cell is the opposite, they can give a low amount of power over a long time period. The supercapacitor is somwhere in between batteries and regular capacitors. Ideally a device is in the right top corner of the plot able to provide a high power over a large timespan.

1.5 Formation of carbon nanofoam

One of the materials used in this thesis is CNF. A literature overview of this class of materials is given in chapter 5 where, also, the fabrication process is explained and the experimental parameters are given. The aim of this section is to give a comprehensive understanding of a process called diffusion-limited aggregation which is a fundamental part of CNF formation. Figure 1.23 shows an illustration of a diffusion limited aggregation process with a laser as the energy source. A carbon material is illuminated with a focused laser beam as seen in Figure 1.23a. The laser interacts with the carbon. A dense carbon plasma, is formed which has a diameter of a few nanometres. Carbon diffuses out of the plasma mostly in individual clusters, made out of an accumulation of carbon molecules (Figure 1.23b). These clusters redeposit on the carbon precursor material beside the laser induced plasma, around 5 mm around the plasma. A physical barrier held close, (below 5 mm above the substrate), to the plasma blocks the diffusion and, hence, the clusters aggregate on the barrier.

A simulation of diffusion limited aggregation was done by Witten et al. [52] A transmission electron microscopy image (Figure 1.24) of CNF looks very similar to the simulated structure. This confirms the diffusion-limited aggregation formation of CNF.

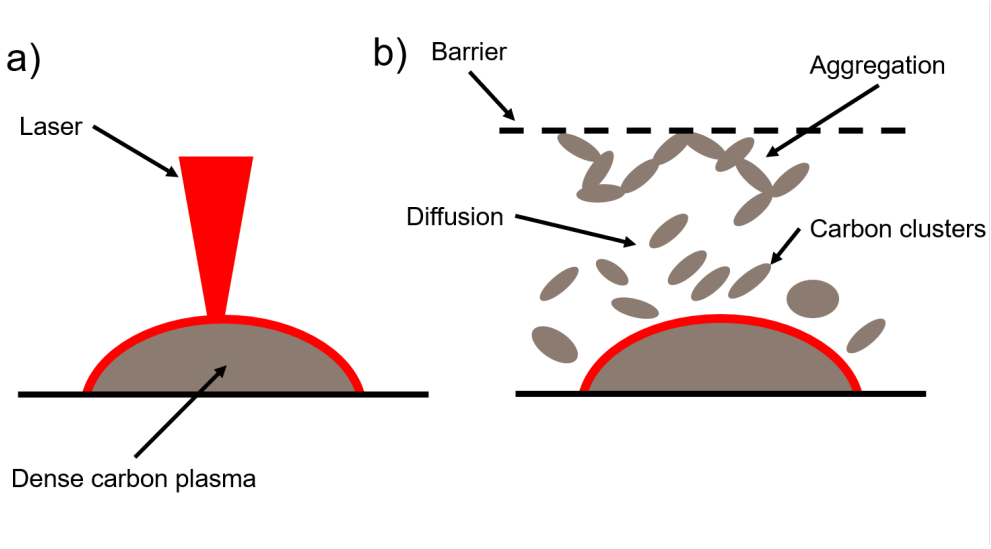

Figure 1.23: Schematic of diffusion-limited aggregation process, a) laser is interacting with carbon target forming dense carbon plasma, b) carbon clusters diffuse out of the plasma and aggregate at a barrier within the diffusion region.

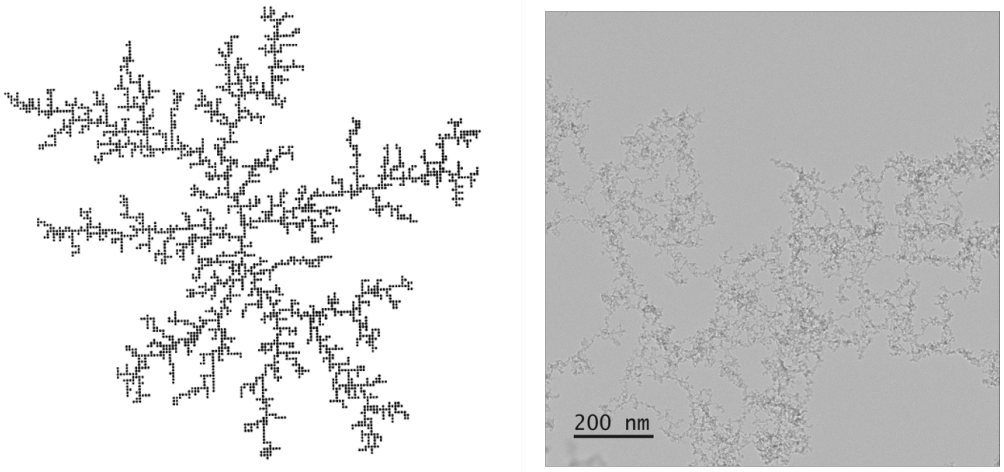

Figure 1.24: a) Simulation of diffusion-limited aggregation process by Witten et al, Figure adapted with permission from Witten et al., Physical Review B, vol. 27, 9, 1983 [52] , b) TEM image of CNF.

Chapter 2

State-of-the-Art

The focus of this work is on the incorporation of nanomaterials (such as graphene and carbon foam) into gas sensor and supercapacitor applications. Device performance for both these applications is dependent on the available surface area. For gas sensors, a larger surface area results in more adsorption sites that the molecules can attach to [53]. For supercapacitor applications, the increased surface area allows for a larger double-layer capacitance which increases the capacity of the device [54]. This literature review focuses on the aforementioned applications, which are the applications researched in this thesis.

The first part of this literature review will provide an overview of the published synthesis methods for graphene and carbon foam. Graphene synthesis methods can be divided into two categories; those that lend themselves to commercial applications and those that are more suitable for research and development purposes. Methods for the synthesis of carbon foam are less diverse and are based on two main concepts of either blowing up a precursor or use a template to create a foam.

The second part focuses on graphene-based gas sensor applications. Other nanomaterials are also used for gas sensor applications. These have been reviewed extensively elsewhere [55–57]. However, they are considered to be outside the scope of this overview. As part of this thesis considers the gas adsorption mechanism in percolating graphene films, a review of relevant research into sensing mechanisms in graphene-based structures is included.

The final section reviews current research into carbon foam use for gas sensor and supercapacitor applications. Carbon foam is a nanomaterial at a relatively

early stage of research and development and, therefore, has not been extensively incorporated into device structures. As such, there is limited literature concerning the application of carbon foam and so, a more general overview is provided.

2.1 Graphene

Ever since the discovery of graphene by Novoselov and Geim [6], significant effort has been invested to both characterise the properties of the material and to investigate potential applications. This single-atom thick carbon layer has excellent electronic and mechanical properties [7].

One of the biggest potential opportunities is to incorporate graphene into the semiconductor industry in order to help maintain Moore's law, described in chapter 1 [58].

Other applications of graphene include its incorporation into composites to increase their conductivity or robustness [59]. Graphene's large surface area to volume ratio means that it is particularly suited to gas sensing and energy storage applications [60]. One of the major drawbacks of graphene is its expensive synthesis and the lack of control of the quality of the graphene itself.

2.2 Graphene Synthesis Methods

Graphene was discovered by mechanical cleavage. During mechanical cleavage graphite flakes are exfoliated with scotch tape until only a single atom-thick layer of carbon remains [6, 61]. These exfoliated flakes are of high quality but the yield is usually low and only small flakes are produced. Another mechanical exfoliation technique capable of synthesising large quantities of graphene is solvent-based graphite dispersion and ultrasonication. The treatment with ultrasonic waves drives the cavitation between the individual sheets of the graphite and tears them apart. The solvent stabilizes the flakes and keeps them from re-agglomeration. Here graphite is mixed with a solvent, for example N-Methyl-2-pyrrolidone (NMP), and sonicated to produce individual sheets of graphene [62, 63]. NMP works well because it has strong interaction with the sheets of graphene and therefore reduces the energetic penalty for exfoliation and subsequent solvation [64]. Exchanging the solvent for water and

a surfactant also results in exfoliated graphene flakes [65]. This method is scalable and has been industrialised by companies such as Thomas Swan Ltd. However, the yield of graphene is currently relatively low. In addition, the graphene flakes are often small (< 1 μm) and agglomerated, meaning that multi-layer graphene is produced rather than single layer platelets.

The most common method used to produce high quality graphene over large areas is a chemical vapour deposition (CVD) technique. Multilayer graphene, in this case 35 layers, was grown for the first time in a CVD process by Somani et al. [66] on a nickel foil with camphor as the carbon source. Silicon and copper have been used to deposit a variety of numbers of graphene layers stacked on top of each other [66–71].

Controlling the number of graphene layers synthesised on the metal substrate is the main challenge in CVD. In order to create a graphene film, the metal substrate is heated to a high temperature (900-1000 degree) before a precursor gas (highly diluted hydrocarbon) is introduced into the deposition chamber. Carbon from the precursor gas diffuses into the metal substrate during the exposure. By cooling the substrate, precipitation of the carbon occurs, forming graphene. Controlling process temperature, gas exposure and cooling rate allow control of the number of synthesised layers [69, 72].

Plasma enhanced chemical vapour deposition (PECVD) is an adaption of the CVD process where a plasma is used to enable deposition at a lower temperature. Graphene has been grown using a PECVD process at a temperature of $\sim$680 °C, which is $\sim$400 °C lower than conventional CVD [72, 73]. The growth mechanism of the graphene and understanding of how to control the number of layers deposited during PECVD has been the focus of investigations in recent years [74–76]. The plasma introduces additional high-density reactive gas atoms and radicals which allows both a more rapid synthesis and lower reaction temperatures [76, 77].

In parallel with the ongoing investigations to improve CVD manufacturing methods, there has also been activity to investigate scaling up graphene synthesis to industrially feasible volumes. One possible method was presented by Bae et al. [78]

using a roll-to-roll production process. The researchers showed the production of a 30-inch diagonal graphene film on to copper substrates with electro-optical properties of approximately 125 Ohms per square and 97.4 % transmittance. Hesjedal [79] demonstrated an atmospheric-CVD process for synthesising graphene on flexible copper substrates without the need for post processing. Yamada et al. [80] showed a technique to lower the temperature to below 400 degree in a roll-to-roll process using microwave assisted CVD, which had the effect of reducing manufacturing time. However, this process only yielded small graphene sheets, which are not suitable for industrial applications. Kobayashi et al. [81] investigated a low pressure roll-to-roll process at high temperatures (1000 degree). The research reported improved film quality, but also described a dependence of the film's defect- and microcrack- density on temperature. Cracks and defects in the film were observed during the process when the temperatures were well above the initial 1000 degree. Chandrashekar et al. [82] developed a process where no post etching of the flexible copper substrate is necessary in order to transfer it to a different substrate (in this case, a plastic substrate was used). Before there was always a deposition and wet etching process step involved to add the targeted substrate and etch the Cu substrate from the graphene to release it. Chandrashekar et al. used a hot water interaction with the native oxide of the copper foil on which the graphene was deposited to detach the carbon and transfer it onto PET. Alrefae et al. [83] used a statistical model to investigate the quality of their roll-to-roll graphene synthesis. The investigation showed the quality of the graphene depends on the gas pressure, nitrogen presence, oxygen presence, and plasma power during the plasma enhanced CVD (PECVD) process. In this case, the graphene quality was limited by the plasma quality during the synthesis. Kidambi et al. [84] developed a graphene roll-to-roll synthesis achieving a speed of 5 $\mathrm{cm\,min^{-1}}$, which is the quickest reported so far.

While the aforementioned methods are the most commonly used in research and industry, other methods to create a single atom thick sheet of carbon have also been investigated.

Graphene can be synthesized through thermal decomposition of SiC and other substrates. In order to achieve this, ultra-high vacuum and high annealing temper-

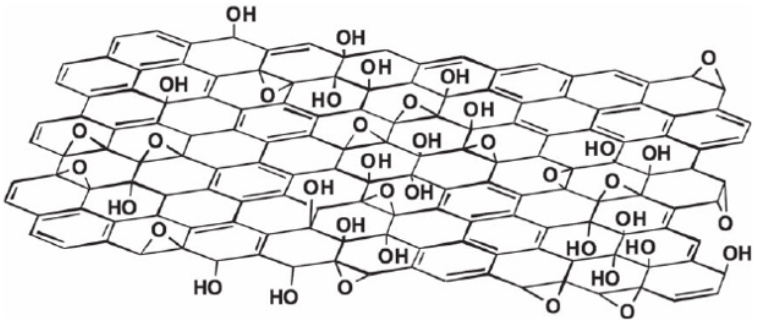

Figure 2.1: Illustration of GO. Figure adapted with permission from He et al. Chem. Phys. Lett, 287 (1998) 53-56 [94].

atures of ∼1200 °C are necessary. Silicon sublimates at this temperature leaving behind carbon which forms graphene [85]. The number of layers deposited is controlled via the duration and temperatures used during the process. However, a common difficulty that occurs during large scale production is the control of the number of layers because the growth pattern changes on different SiC faces. Ideally a continuous film is grown, but individual islands form if the substrate is not chosen correctly. Therefore, a better understanding of the influence of the substrate on the electronic properties of the formed graphene is necessary [86].

Other methods are the unzipping of CNTs into graphene [87–91]. The most frequent method used for the unzipping process is a hydrogen plasma [92], although mechanical unzipping using glass micro blades is also possible [93].

An alternative approach used is the reduction of graphene oxide (GO) to create reduced graphene oxide (rGO), GO is schematically depicted in Figure 2.1. The structure of rGO is similar to graphene but it has many defects [95]. It can be synthesized in large flakes, comparably bigger than graphene flakes and dispersed in water where it remains stable. Simple reduction can be achieved by exposing GO to elevated temperatures of ∼300 °C in air [96]. Alternative reduction methods have been investigated to minimise the defect density of the reduced graphene oxide sheets to achieve a quality which is closer to graphene. A chemical process using hydrazine or hydroquinone results in the reduction of the GO well below the thermal reduction temperatures [97, 98]. Another approach is a sonochemical method where acoustic cavitation in high pressure and high cooling rate environments is used [99–102]. This

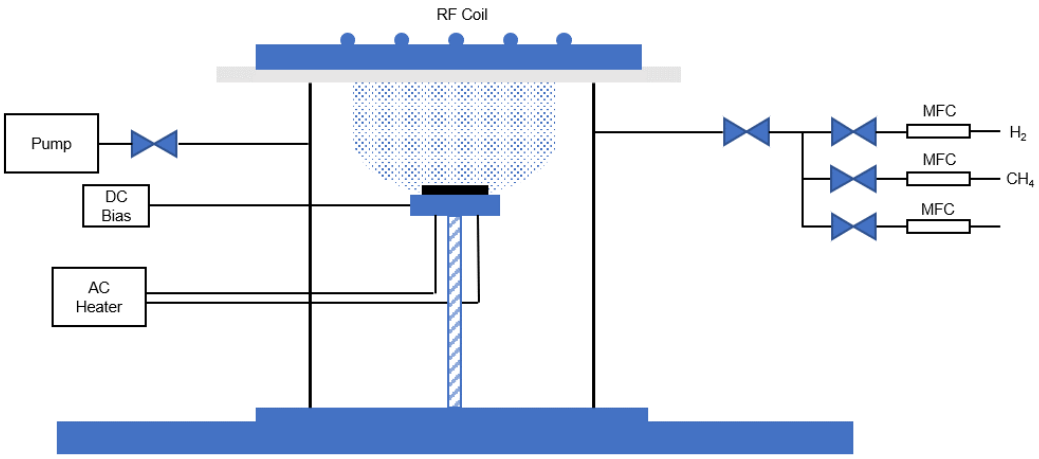

Figure 2.2: Illustration of PECVD synthesis setup, MFC stands for Mass Flow Controller.

process has led to a high quality product with low defects, no oxygen content and a high electron mobility [103].

Local heating by a laser is another method which is increasingly being investigated, enabled by the development of laser technology. A graphene oxide dispersion can be directly reduced by laser irradiation to form rGO [103]. GO films can be selectively reduced to form functional patterns using laser patterning methods [104–112]. Graphene oxide reduction using both a Xenon flash [113] and UV-induced photocatalytic reduction have been demonstrated [114, 115].

2.2.1 Microwave plasma-enhanced chemical vapour deposited commercially available graphene

The graphene used in this thesis was commercially available from a company called Cambridge Nanosystems[1]. A microwave plasma-enhanced chemical vapour deposition process is used to mass produce the graphene. This section is intended to describe this synthesis as reported in literature and compare these reports and results with the material as received.

Literature reports the following on microwave plasma-enhanced chemical vapour

[1] 17 Mercers Row, Cambridge, Cambridgeshire CB5 8HY United Kingdom

deposition of graphene. A substrate (in the study various were used: Si, SiO_2, Al_2O_3, Mo, Yr, Ti, Hf, Nb, W, Ta, Cu and 304 stainless steel) on which the graphene is synthesised is placed in a vacuum chamber as illustrated in Figure 2.2. Multiple mass flow controllers allow the exact control of precursors introduced into the chamber. A plasma is generated in the chamber using a radio frequency (RF) coil operated at 900 W. A heater located beneath the substrate is used to control the temperatures within the chamber. Methane is used as the carbon precursor and the process is operated at approximately 700 °C. This is significantly lower than conventional CVD processes, which use operating temperatures of up to 1200 °C. The elevated temperatures and plasma cause diffusion of carbon into the substrate. Cooling the substrate allows the precipitation of carbon on the surface, which forms graphene flakes. No pre-treatment, except for cleaning, is necessary for the substrate.

SEM images of the produced graphene are shown in Figure 2.3. Individual sheets of stacked graphene layers are visible which do not cover the substrate in a single sheet but can be observed standing up from the substrate.

The synthesis method has been developed to use a microwave assisted plasma rather than a RF plasma. Malesevic et al. [74] were the first to report graphene made in a microwave-assisted CVD process. Figure 2.4 shows the SEM and TEM images of the fabricated graphene. The SEM reveals a similar structure to the RF coil induced plasma process with small sheets of freestanding graphene. TEM shows the few-atom graphene layers of which the flakes are composed. Figure 2.5 shows the Raman spectrum taken from the material. The 2D/G ratio, indication for the number of graphene sheets present, shows the multi-layer character of the fabricated films. The D/G ratio, an indication of how many defects the graphene has, shows that the materials are not pristine and that defects are present.

Alongside the aforementioned materials which were made in a laboratory environment, it is also possible to procure commercially available material. Cambridge Nanosystems have patented a microwave plasma CVD production system, which allows large-scale production of graphene flakes [116]. The synthesis setup is adapted such that the graphene flakes are collected in powder form. The formation of the graphene happens directly in the plasma located in a column, resulting in graphene in powder form. These powders can then be dispersed in water or various solvents.

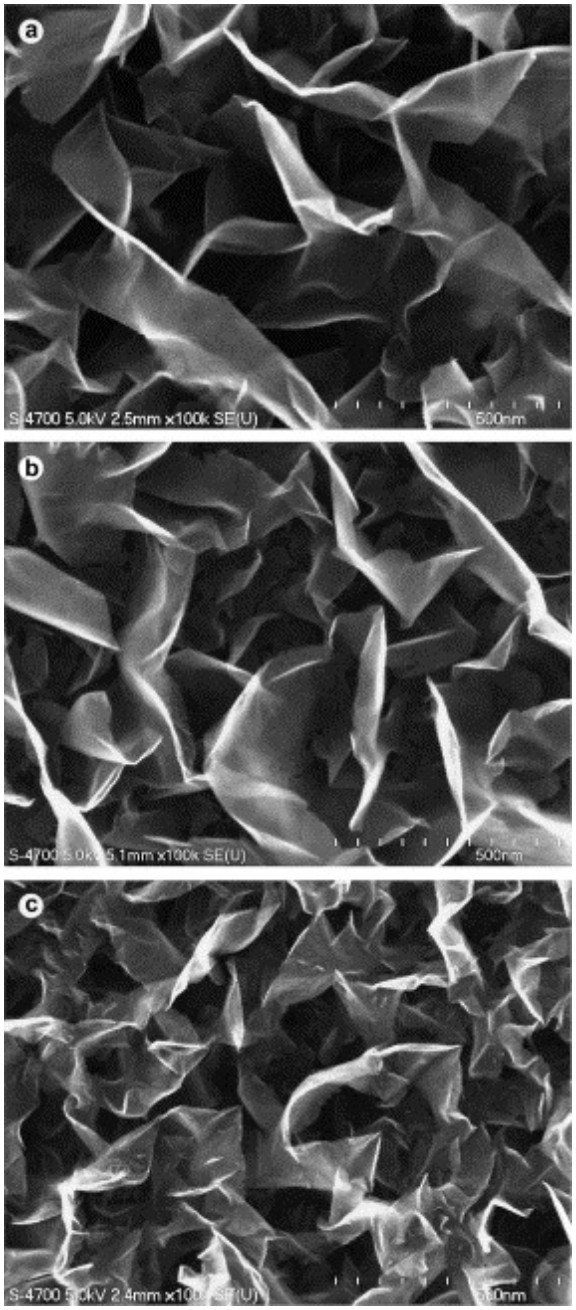

Figure 2.3: SEM image of the PECVD synthesized graphene. Scale bar in images are each 500 nm. Figure adapted with permission from Wang et al., Carbon, vol. 42, 204, 2004 [73].

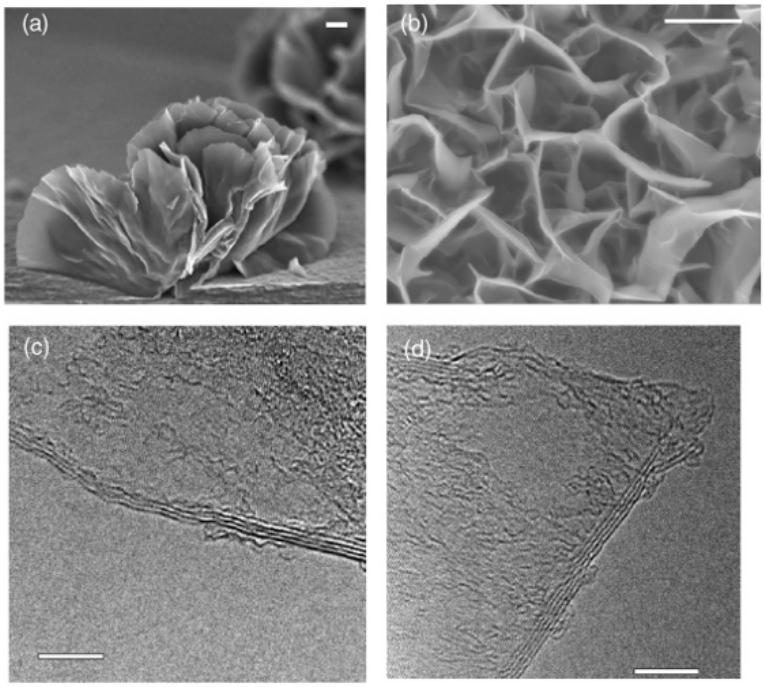

Figure 2.4: a),b) SEM and c),d) TEM of graphene by microwave plasma assisted CVD. Scale bar of SEMs corresponds to 1 μm, in the TEM to 5 nm. Figure adapted with permission from Malesevic et al., Nanotechnology, vol. 19, 30, 2008 [74].

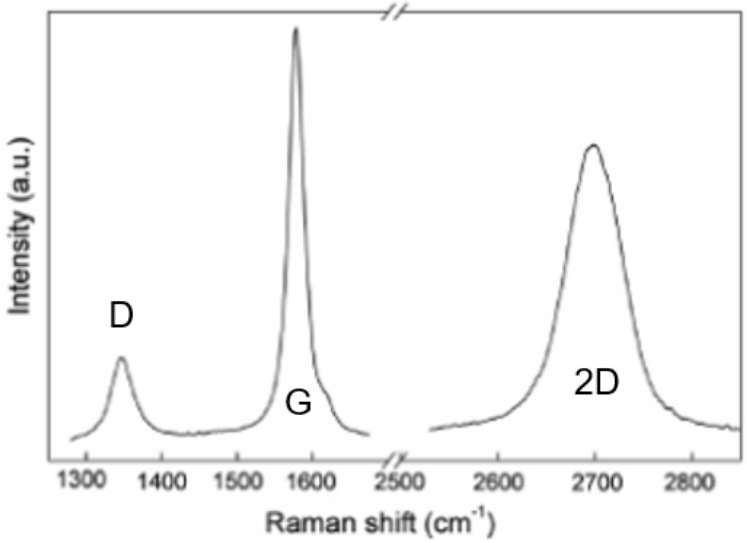

Figure 2.5: Raman of graphene by microwave plasma assisted CVD. Figure adapted with permission from Malsevic et al.,Carbon, vol. 42, 30, 2008 [74].

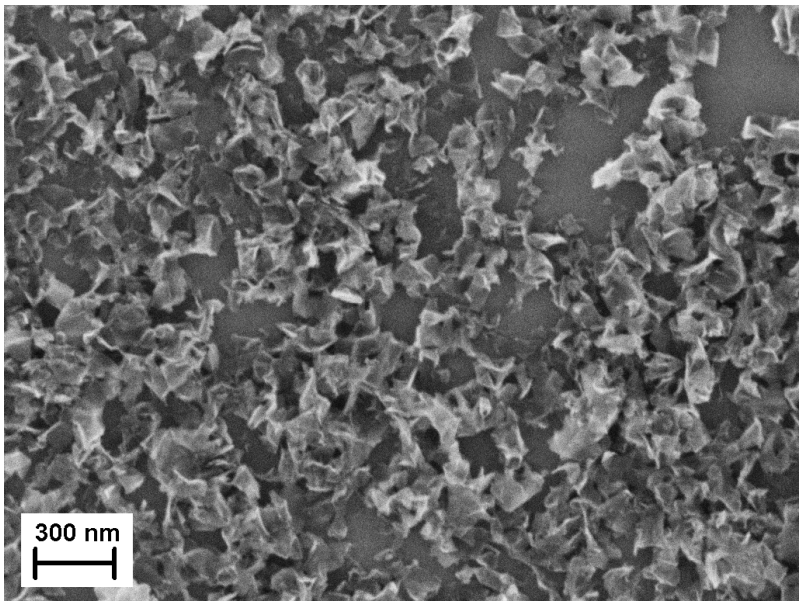

Figure 2.6: SEM image of on glass deposited Cambridge Nanosystems graphene flakes.

Figure 2.6 shows a SEM image of the Cambridge Nanosystems material, as received, in which it can be observed that there are individual flakes present. There are also aggregated materials which have a similar folded structure to the materials reported in the literature [74]. The flake sizes are around 150 nm. Raman analysis (Figure 2.7) of the material shows a similar peak ratio for the 2D/G ratio as the ones reported in literature whereas the D/G peak ratio is lower than the literature values. It is difficult to ascertain if the higher intensity of the D peak is due to defects in the graphene layers or to edge effects in the Raman signal, caused by small flakes. However, it is possible to conclude from analysis of the commercial materials that they are composed of very few layer (3 layers in average, according to the datasheet of Cambridge Nanosystems) graphene sheets with flake sizes around 500 nm.

The received commercially available material was produced on a larger scale than literature-reported materials and whereas the flake size in the scientific literature is commonly of the micron scale, the commercially available materials can be measured in the 100s of nanometre regime. However the quality of the materials are comparable, making this a good example of a scalable material synthesis process. In neither case are the properties of the material pristine and, therefore, if the exact definition of graphene is used (namely a one atomic layer of carbon atoms), the material cannot be categorised as graphene and must be defined as a few-layered

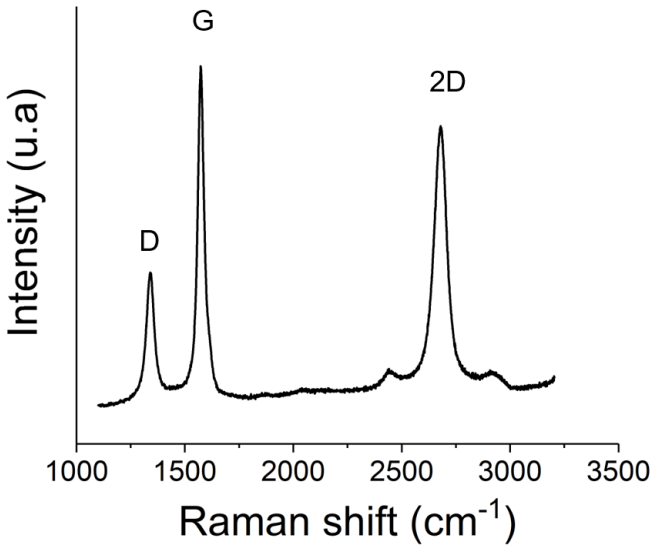

Figure 2.7: Raman analysis of deposited Cambridge Nanosystems flakes.

graphene material. Although the properties of graphene start to appear below 10 atomic layers of carbon, they only fully evolve in the single layer material [117]. Another issue is the aggregation of the flakes, which prevents using them in electronic applications as the properties are bulk-like in these aggregations. However, these materials should show enhanced mechanical stability and are therefore suitable for composite applications.

2.3 Carbon foam

Various methods are available to manufacture carbon foams which can be tuned for pore size and density, and composite structure to improve their thermal and mechanical stability further [118]. In this section, various methods of creating carbon foam are examined, which are inherently different from the formation of the carbon nanofoam using a pulsed laser. SEM images are provided for the different synthesis routes, which each result in a different morphology, resulting in a broad definition of what is considered to be a carbon foam. The formation of CNF is discussed in section 1.5 and in chapter 5. Figure 2.8 shows a SEM image of CNF's structure.

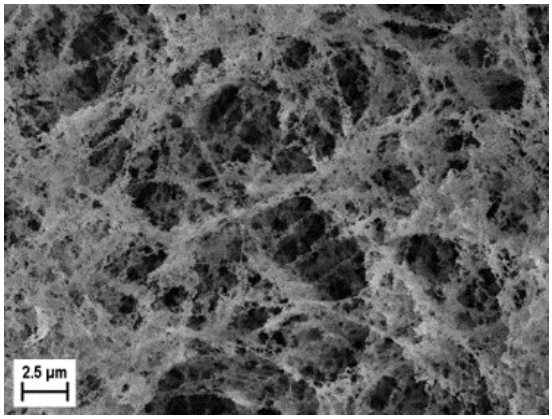

Figure 2.8: SEM image of CNF made in a laser process, at 417 mJ/cm^2 fluence, using GO as a pre-cursor.

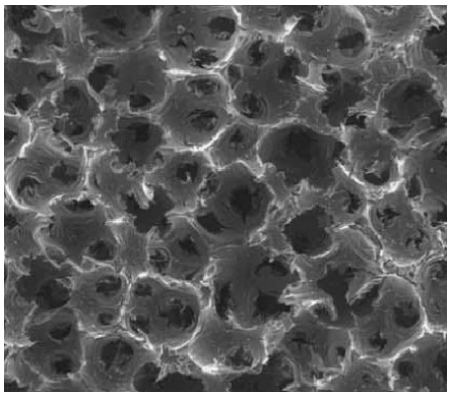

Figure 2.9: SEM image of carbon foam made out of a pitch. Figure adapted with permission from Klett et al., Carbon, vol. 38, 7, 2000 [119].

One way to create carbon foam is by blowing up (increase the volume of a precursor) carbon precursors. There are two different basic methods that are used: pyrolysis and chemical additives.

The pyrolysis method typically starts from a pitch, a carbon based viscoelastic polymer, which is heated (500 K) under pressure (typically around 3 MPa) [119]. The pitch is heated to above its softening temperature, the point where the polymer can be deformed, below this temperature the polymer seems solid. During heating, the pressure is controlled by inserting an inert gas around the pitch. After the long heating step the precursor is cooled down and the pressure is released quickly forming a carbon foam. Figure 2.9 shows a SEM image of the formed foam. The formation of the foam is caused by small bubbles of gases decomposed from the pitch. The

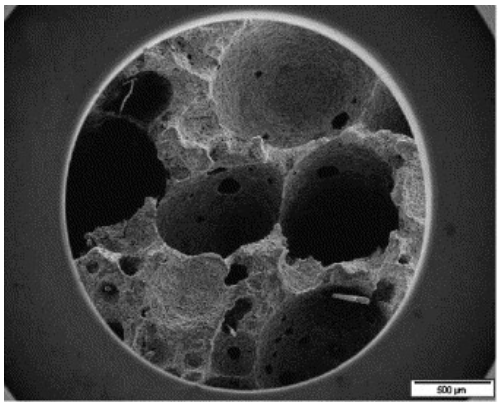

Figure 2.10: SEM image of the carbon foam with incorporated carbon nanofibers. Figure adapted with permission from Beechem et al., Carbon, vol. 44, 8, 2006 [123].

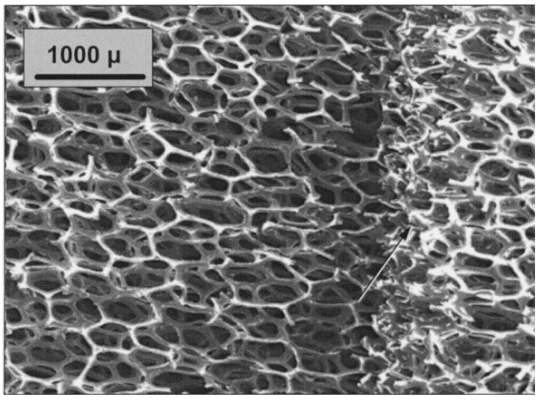

Figure 2.11: SEM image of Reticulated Vitreous Carbon. Figure adapted with permission from Chakhovskoi et al., Journal of Vacuum Science & Technology B: Microelectronics and Nanometer Structures Processing, Measurement, and Phenomena, vol. 21, 1, 2003 [124].

larger porous structures are created by coalescence with neighbouring bubbles and give the foam a cell structure. The aromatic planes of the pitch material tend to align with the walls of the foam cells as it is energetically more favourable [120]. The viscosity and the surface tension are the key parameters to control the cell size and the nanotexture of the foam. Additives like graphitic particles [121], MWCNTs [122], and carbon nanofibers can enhance the mechanical strength of the blown up foam. Figure 2.10 shows an SEM image of the foam with incorporated MWCNTs [123].

Chemical additives, in this case Arylacetylene as carbon precursor, pentane as the blowing agent and Tween 80 as bubble stabilizer, can be used to blow up the carbon precursor by heating up the mixture. This causes thermal expansion and partial evaporation of the carbon leaving the porous carbon behind [125].

Template carbonisation creates carbon foams by treating a precursor foam, often polyurethane, at high temperatures to carbonise it. This process has been commercialised resulting in Reticulated Vitreous Carbon (RVC). Figure 2.11 shows a SEM image of the RVC [124, 126]. The thermal and mechanical properties can be enhanced by electroplating metals on to the foam [127–129]. Polymethylmethacrylate (PMMA) can be used as a template for carbon foam. Figure 2.12 shows a SEM image of the templated foam. When formed into spheres and mixed together with resorcinol (a form of benzendio ($C_6H_4(OH)_2$)) and formaldehyde (RF) precursor, it

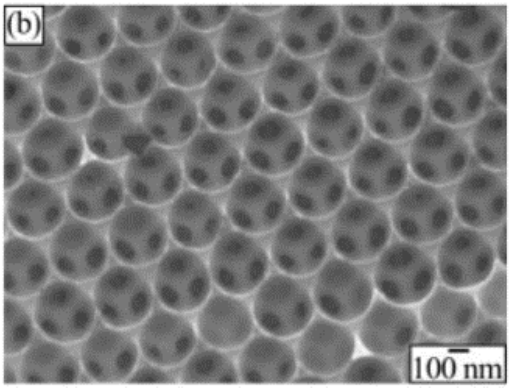

Figure 2.12: SEM image of templated carbon foam. Figure adapted with permission from Lee et al., Advanced Functional Materials, vol. 15, 4, 2005 [130].

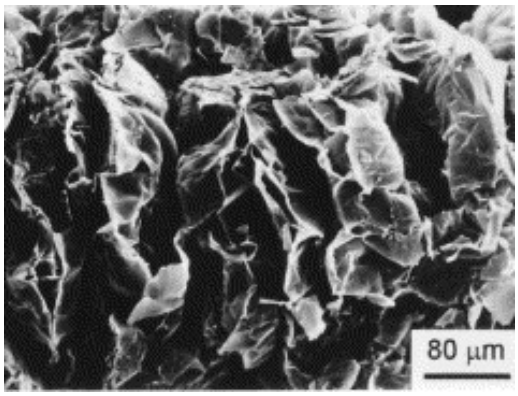

Figure 2.13: SEM image of a carbon foam made in a mould. Figure adapted with permission from Han et al., Carbon, vol. 36, 12, 1998 [132].

is possible to form well controlled carbon foam [130]. RF gels are soaked with water, which is then replaced with acetone by immersion and the acetone is then replaced with liquid carbon dioxide allows use of critical point drying, which then leaves a porous structure [131]. The critical point drying is necessary so no capillary forces act on the foam destroying the porous structure.

Sodium chloride can be formed into a bar structure before annealing, which results in a porous structure. A phenolic solution is poured into the salt and the solvent evaporates leaving the resin behind, which is then pyrolyzed. Removing the salt and freeze drying results in a carbon foam structure [133].

It is also possible to create a carbon honeycomb from a RF hydrogel. It is firstly carbonized at 1000 degree and then freeze dried. The freezing is controlled in one direction resulting in an aligned porous structure in the synthesized carbon foam [134]. This method allows the synthesis of directional carbon foams, with walls aligned in one direction. This geometry allows enhanced mass transfer in one direction beneficial for applications like catalysts or energy storage devices.

Carbon foam can also be created via compression of exfoliated graphite placed in a limited space mould [132]. Figure 2.13 shows a SEM image of a foam so-formed. This foam is proposed for heat pump applications, where high porosity materials are used to facilitate the flow of the working fluids. Commercial exfoliated graphite has been incorporated into carbon foam structures to improve the thermal capabilities for eventual use in heat storage devices [135].

A more recent approach uses assembly of graphene nanosheets to yield carbon

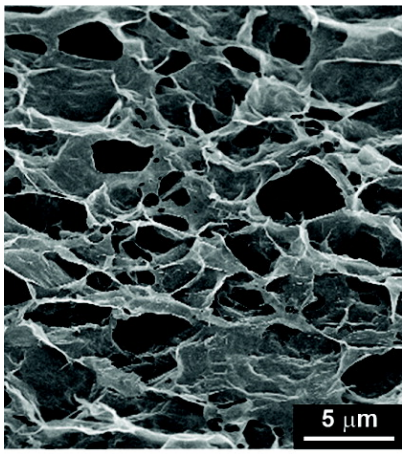

Figure 2.14: SEM image of carbon foam made in a freeze drying process. Figure adapted with permission from Xu et al., ACS Nano, vol. 4, 7, 2010 [136].

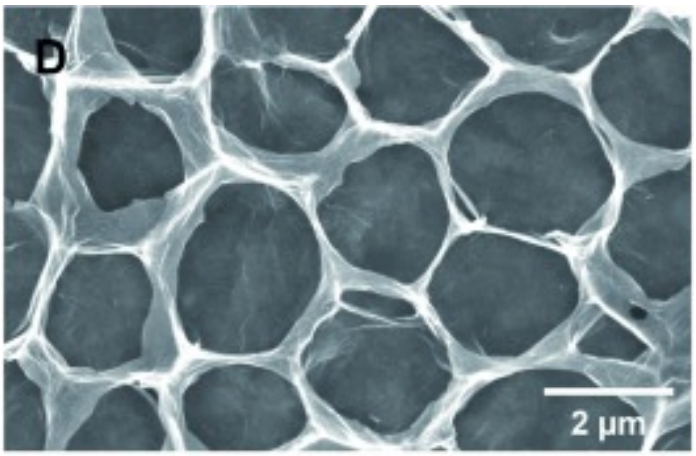

Figure 2.15: SEM image of carbon foam made out of graphene through lyophilization and supercritical drying. Figure adapted with permission from Lee et al., Angewandte Chemie, vol. 49, 52, 2010 [142].

foam. The most common method is the hydrothermal reduction of GO via freeze drying (Figure 2.14 shows the structure of the resulting foam [136]). During the freeze-drying process, the GO becomes rGO and becomes hydrophobic. The sheets repel each other and form an assembly of flexible nanosheets in a volumetric porous form with no requirement for a carbonisation step [137–141].

Aqueous droplets of the GO are used as a template for casting carbon foams with graphene sheets (Figure 2.15 shows the graphene foam) [142]. The density of the aerogel can be tuned by varying the precursor of the foam. Incorporating CNTs into the process can allow very low density materials to be formed (0.16 mg/cm^3) [143], whereas, when the concentration of the rGO in the precursor is increased, a very dense carbon foam can be synthesized (1.58 g/cm^3) (Figure 2.16 shows the dense structure formed by adding rGO [144, 145]).

Carbon foams have also been created by using microwave irradiation to expand a precursor made out of graphene oxide [141]. This method reduces the GO while it forms the aerogel with robust mechanical shock absorption capabilities.

Another method is to deposit graphene flakes on to a Ni foam template by CVD. The template was then removed with an etching process leaving behind a foam structure consisting of graphene films (Figure 2.17 shows the CVD grown foam) [146].

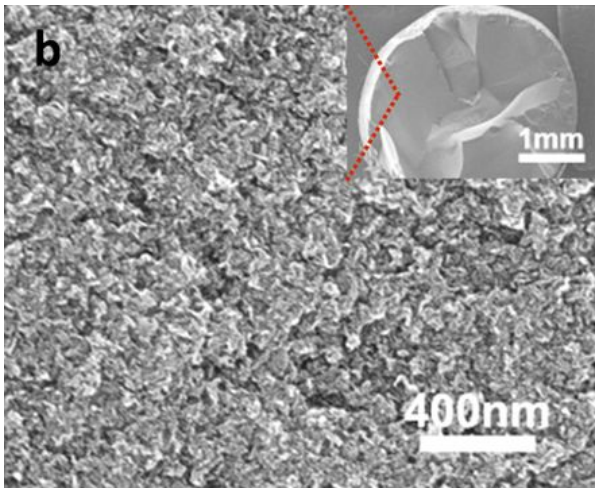

Figure 2.16: SEM image of a carbon foam with added rGO forming a dense morphology. Figure adapted with permission from Tao et al., Scientific Reports, vol. 3, 7, 2013 [144].

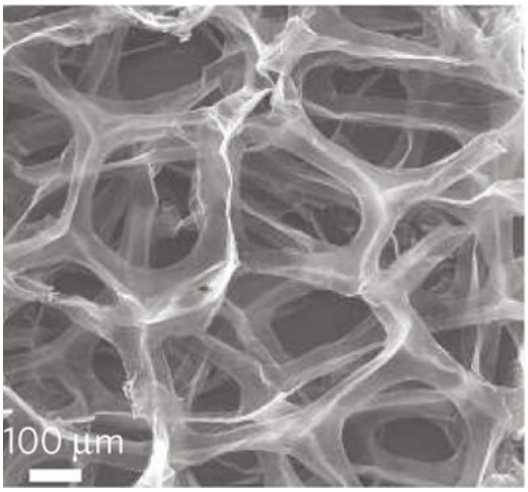

Figure 2.17: SEM image of a carbon foam grown in a CVD process. Figure adapted with permission from Chen et al., Nature materials, vol. 10, 6, 2011 [146].

Carbon source	Method	Density [g cm^{-3}]	Pore size [μm]	Application	Ref
Vicsoelasticr polymer	Heating	0.2	275	Thermal management	[119]
Viscoelastic polymer	Heating	-	40	Mechanical enhancement	[123]
Viscoelasticr polymer	Carbonisation	-	500	Field emission cathod	[124]
Resorcinol (benezendiol)	Templated carbonisation	0.36	0.273	Batteries	[130]
Graphite powder	Heating	0.1	0.55	Thermal pumps	[132]
Graphene oxide	Freeze - drying	0.002	1	Supercapacitor (160 Fg^{-1})	[136]
Graphene oxide	Templated casting	-	1.5	Supercapacitor (103 Fg^{-1})	[142]
Graphene oxide	Freeze - drying	1.58	0.002	Supercapacitor (373 Fg^{-1})	[144]
Graphene	CVD	0.005	100	Batteries	[146]

Table 2.1: Summary carbon foam synthesis

2.4 Gas sensing

There are many different device structures commercially available for gas sensing. The market is forecast to grow over the coming years as part of the growth in popularity of the Internet of Things (IoT) concept [147]. It is predicted that sensing applications will focus on volatile organic compounds, CO and NO_2, which are major contributors to environmental air pollution. Whereas volatile organic compounds (VOCs) and CO_2 are commonly measured in parts per million (ppm), NO_2 is often required to be measured on a parts per billion (ppb) scale. Air pollutants often come from incomplete combustion processes that occur in industry, homes and car engines [148]. Table 2.2 shows the most common air pollutants, their source and associated European emissions limit. This table shows that industry and transport are the major contributors. Air pollution is currently assessed using a small number of static measuring locations and mathematical models. Increased fidelity could therefore be achieved by utilising simple portable gas sensing devices that are able to measure the values at multiple locations, rather than relying on a mathematical model to interpolate the data from the static locations. Mobile measuring devices could be used to monitor a large area, giving reliable, high-resolution data on air pollution to give greater impetus to reducing pollutant emissions.

Pollutant	Origin	EU limit
Ozone (O_3)	chemical reaction in air from other pollutants	100 ppb
Nitrogen dioxide (NO_2)	engine vehicles, industry, gas heaters, gas stoves	40 ppb
Carbon monoxide (CO)	carbon fuels, incomplete combustion	10 ppm
Sulfur dioxide (SO_2)	combustion in power plants	125 ppb
Ammonia (NH_3)	Agriculture	25 ppb

Table 2.2: Most common air pollutants, their origin and the European Union limit of allowed concentration in the air. Source is the Department for Environment Food and Rural Affairs (DEFRA) in the UK. Forms are added in the Appendix.

Current state of the art gas measuring systems are based on mass spectrometers, which are able to detect very low concentrations and identify molecules accurately. However, these systems are very expensive and bulky. There are optically-based

systems, based on photoionization using a laser as irradiation source, which can measure concentrations down into the single digit part-per-billion level at high speed, but they are not able to determine which molecule they are detecting (also known as selectivity). The ionized gas molecules move towards the negative electrode after ionisation where a current is generated and then converted into a concentration unit. Electrochemically-based systems use conductive materials which adsorb certain gas species and change their conductivity upon exposure. Due to the available range of materials, which respond to different gases, these sensors can be made more or less selective and can reach an acceptable limit of low ppb sensitivity for NO_2 and ppm sensitivity for other gases. Current electrochemical sensors are based on metal oxides, mostly ZnO, which need to be heated up to 300 - 400 °C, resulting in high power consumption, poorly suited to autonomous IoT devices [149]. In addition, they need to be heated to even higher temperatures to desorb the analytes from the functional sites to which they are absorbed. The focus for research in the field of gas sensing has tended towards reducing power consumption, lowering the limit of detection and improving the selectivity of the sensing devices.

Nanomaterials are of particular interest for electrochemical gas sensor applications because of their high conductivity, which reduces the noise level. Large accessible surface areas also make them an ideal candidate for the adsorption of gases. There are multiple sensor architectures that are able to take advantage of the properties of nanomaterials.

The focus of this review is on plain-material devices as functionalised materials are outside the scope of this thesis which examines the development of a new device architecture for graphene and carbon nanofoam sensors, which have not been used for electrochemical sensing previously.

2.4.1 Graphene based electrochemical gas sensor device structures

In the following section, different device structures are examined, each with the ability to use graphene as the sensing element. It should be noted that graphene has previously been incorporated into field-effect transistor (FETs) structures, but the advantages of graphene incorporation only became apparent at a later date,

as understanding of the sensing mechanism advanced. This is shown by the first graphene FETs being operated at 0 V gate bias, which effectively renders the transistor a straightforward chemiresistor measuring the resistance between source and drain.

2.4.1.1 Field effect transistor

The transistor configuration is based on the fabrication process from the complementary metal oxide semiconductor (CMOS) industry. The gas transistors are FETs constructed from a back-gate (usually silicon), a dielectric (usually silicon oxide) and the active material, in this case graphene [150]. Gate-, source- and drain-electrodes are then contacted using metal. This back-gate approach allows gases to interact with the sensing layer of the material. Figure 2.18 illustrates the device architecture and the different gate - bias possibilites. Depending on n or p behaviour of active layer a conductive channel is formed between source and drain allowing a current to flow or enhancing the already existing conductivity when the gate is biased. For p-type material a conductive channel is formed for a negative bias, for a n-type material with a postivie bias. Upon increasing the concentration, the conductivity signal of the material then increases or decreases depending on the gas. Graphene has p-type behaviour at room temperature in a humid enviornment [151]. Interacting gases are either n- or p-type gases, so they either donate electrons (n-type) or absorp electrons (p-type). N-type gases donate electrons to the p-type graphene, adding minority carriers, therefore decreasing the conductivity. P-type gases absorp electrons of the p-type graphene, removing minority carriers, therefore increasing the conductivity of the graphene.

Schedin et al. [33] were the first to incorporate graphene into a FET structure. They exfoliated the graphene 2D layer using the scotch tape method and inserted their transistor into a strong vacuum whilst exposing it to a strong magnetic field. The graphene was acting as a Hall bar structure. The Hall bar is cooled and exposed to a strong magnetic field vertcial to it. The Lorentz force then allows the measurement of the resitivity along and across the hall bar structure. The gate voltage was kept close to the neutrality point as they detected the biggest response in this configuration. The resistivity in this structure at low temperatures (4 K in this case)

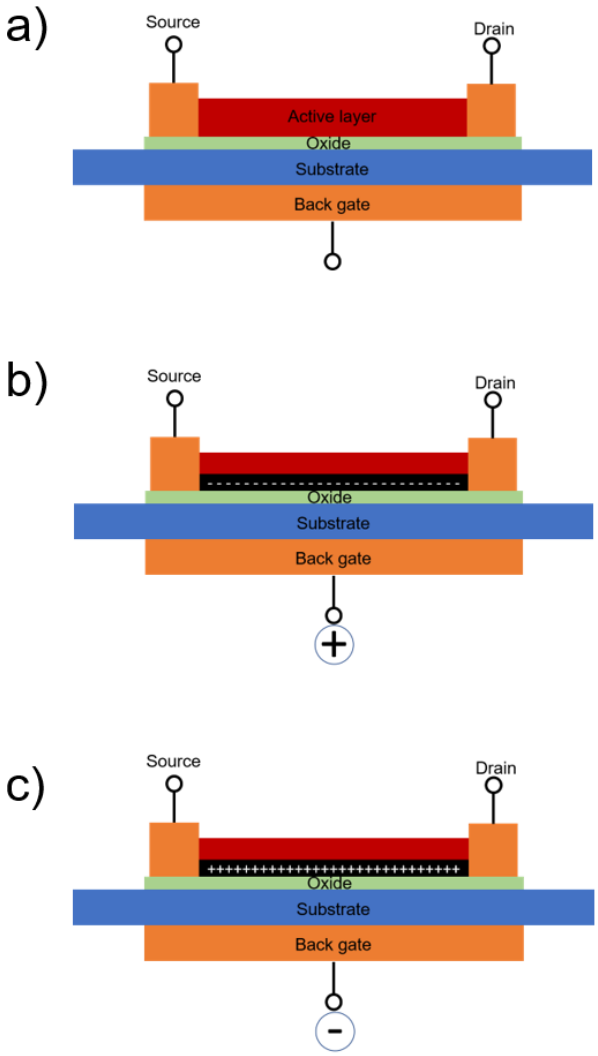

Figure 2.18: a) schematic of a back gated FET structure, the active layer is exposed to the atmosphere around it, the oxide separates the active layer from the substrate, source and drain are fabricated onto the oxide, the gate structure is fabricated on to the substrate, source, drain and gate can be biased, b) upon positive gate bias, negative charges accumulate close to oxide in the active layer, c) postive charge accumulate close to oxide in active material upon negative bias.

becomes quantized. When very dilute NO_2 was inserted into their measurement chamber, individual molecule adsorption and desorption steps were observed. As these measurements were performed at low temperatures and subjected to a high magnetic flux, they are not feasible for day to day applications. However, it does show the advantageous properties of graphene.

Rumyantsev et al. [152] studied the Gaussian noise of graphene when exposed to different gases. Graphene was exfoliated and back gated. During the measurements, the gate voltage was kept at zero and so the material was kept in its p-characteristic state. This configuration prevented instabilities in the conductivity caused by hysteresis. This hysteresis often occurs, caused by trap sites within the material and also at the contacts with the electrodes or the dielectric in the transistor configuration.

Kulkarni et al. [153] used CVD-grown graphene in a FET configuration, in which they kept the gate voltage at 0 V. Rather than exploiting the conductivity of the graphene directly, they investigated the modulation between conductivity fluctuation (modulation of the charge density) and AC current applied. This kind of read-out enhances speed of detection and the limit of detection. By using the cis and trans configurations of the targeted molecules (Chloroform, Toluene, Chlorobenzene, Dichloromethane, 2-propanol, 1,4-dioxane, Acetone, Ethanol) they determined that the sensing mechanism in this configuration was based on the dipole interaction of the graphene with the gas molecules.

Aziza et al. [154] investigated the influence of the lower dielectric on the response of the CVD graphene to ammonia. They found that a mica substrate leads to an enhanced performance compared to SiO_2. This was attributed to substrate doping and the hydrophicity of the mica leading to a shift of the graphene fermi level which leads to a larger overlap with the highest occupied molecular orbital of ammonia and thus a stronger interaction.

In all these FET configurations, it should be noted that the device structure has exclusively been used to characterise the material but not to influence the sensor behaviour. This is because the transistors are operated as simple chemiresistors, only applying a source drain voltage.

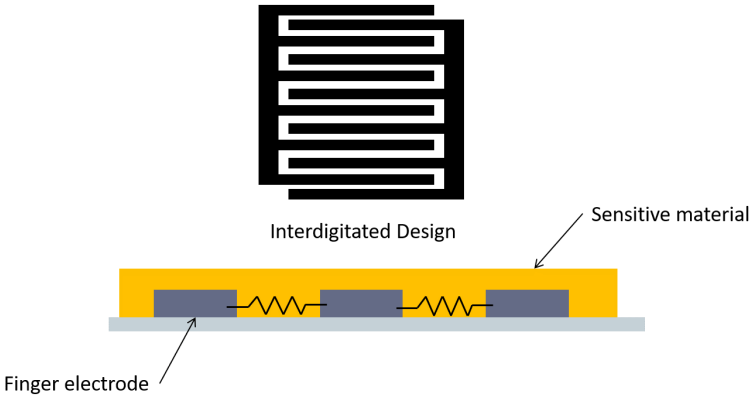

Figure 2.19: Electrode structures for chemiresistors ofen have an interdigitated design, the individual fingers act as parallel resistors, so even small changes can be detected. The finger electrodes are covered with a conductive active material which changes its conductivity upon changes in its environment.

2.4.1.2 Chemiresistor

Chemiresistor structures are the simplest and most common gas sensor structures when nanomaterial use is considered. In this section, the basic structures, based on pristine graphene materials are examined. The field is broadened when the graphene used can be either functionalised or modified [55, 155, 156]. Figure 2.19 illustrates the chemiresistor architecture.

Single sheet graphene is the benchmark when it comes to determining the response of the graphene with respect to different gases. Behaviour is usually tested in ambient conditions at room temperature which represents the environment in which the devices are intended to be used. Yoon et al. [157] transferred exfoliated graphene on to a silicon substrate using a PDMS stamp and contacted the graphene using photolithography. When exposed to CO_2, a reproducible change of conductivity was observed. Yavari et al. [158] exposed a CVD graphene sheet to NO_2 and NH_3 and measured the conductivity. The limit of detection for NO_2 was found to be 100 ppb and 500 ppb for NH_3. The sensor showed incomplete recovery at room temperature but excellent signal to noise ratio. Chung et al. [159] treated the CVD grown graphene with ozone in an attempt to improve the performance of the device. The treatment led to an increased change in the conductivity upon adsorption of NO_2 compared to a pristine material. Additional oxygen functional groups added through the ozone treatment are responsible for the increase in amplitude. An increased amout oxygen functional groups increases the absorption sites

Material	Gas	LOD	t_{90}	Ref
Exfoliated graphene	CO_2	10 ppm	10 sec	[157]
CVD graphene	NO_2 NH_3	0.1 ppm 0.5 ppm	40 min 240 min	[158]
CVD graphene treated with ozone	NO_2	0.2 ppm	10 min	[159]
Chemically exfoliated graphene	NO_2	1.5 ppm	-	[160]
Few layer graphene	CO_2	3 ppm	11 sec	[161]
Flexible CVD graphene	NO_2	0.2 ppm	1 min	[162]

Table 2.3: Summary chemiresistive graphene device performance. LOD stands for limit-of-detection, to lowest possible concentration detectable, t_{90} is the time needed to reach 90% of the saturated value when exposed to a gas.

for NO_2, therefore a bigger change in conductivity is expected when more functional groups are present. Massera et al. [160] used chemically exfoliated graphene sheets and drop cast them onto electrodes to measure the conductivity. The graphene reacted to single digits ppm of NO_2 and showed a lasting drift (change of electrical signal over time without any external influence) upon gas exposure. Nemade et al. [161] investigated few-layer graphene chemiresistor performance. The limit of detection for CO_2 was found to be 3 ppm and for Propane around 4 ppm. Choi et al. [162] created a flexible chemiresistor from polyamide and CVD-grown multilayer graphene. A limit of detection of 200 ppb was reached for nitrogen dioxide in this device structure and showed a slight increase in response in a bent state compared to the initial flat state.

2.4.1.3 Capacitive

Capacitive gas sensors are based on the general capacitor equation

$$C = \epsilon\epsilon_0 \frac{A}{d} \tag{2.1}$$

where C is the capacitance, ϵ the dielectric constant of the insulator separating the two plates and an the same time is the gas absorbant, ϵ_0 the dielectric constant of vacuum, A the area of the capacitor plate and d the distance between the plates. Figure 2.20 illustrates the parallel plate capacitor.

In sensing applications, a change in capacitance occurs when the adsorbate

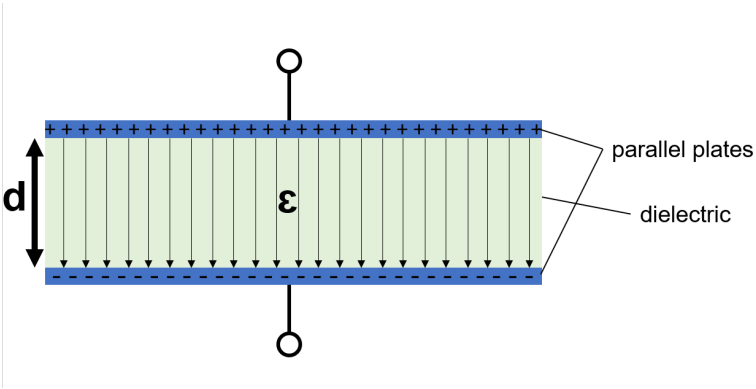

Figure 2.20: Schematic of a parallel capacitor with two parallel plates separated by a distance d. An insulator with the dielectric constant ϵ lies between the parallel plates. When charges opposite charges sit on the parallel plates forming an electric field through the insulator depicted as arrows. The dielectric can be choosen so it changes its dielectric constant upon absorption of a gas, or it changes the separation betwen the plates changing therefore the capacitance.

changes the dielectric constant of the adsorbent or when the distance between the plates is changed. Polymers are often used in gas sensing applications as the adsorbate changes the dielectric constant of the adsorbent. Polymers tend to swell when absorbing materials and, if the device is well designed, the polymer can only swell in one direction which is then measurable, as it not only changes its dielectric constant but also changes the plate separation [163].

2.4.1.4 Sensing mechanism

In order to improve gas sensing performance, it is not only crucial to find the right architectures of device to measure the properties of the material, but also to gain an understanding of the interaction of the gases with the material. The interaction of gases with 2D materials is not yet well understood. Theoretical approaches to determine the process and location of the gases' adsorption site on the material have been investigated but are not experimentally proven yet. There are experimental approaches that attempt to show how the different defects of graphene influence the sensing behaviour, these measurement are not yet able to prove the adsorption theories though.

Chen et al. [164] showed that the conductivity of the graphene can be modified by changing the carrier density within the material. Potassium was deposited on to graphene to introduce charged impurities into the material. Upon increased dop-

ing, the conductivity range with different gate voltages increased. With the first, proof of concept, gas sensor devices, the gas sensing properties of graphene were studied further. The effect of dopants and defects in the graphene was investigated by Zhang et al. [165]. Simulations show enhanced reactivity to gases with heavily doped or defected graphene compared to pristine graphene. It is also stated that pristine graphene is not an ideal material for gas sensing. Romero et al. [166] investigated the adsorption and desorption of ammonia onto graphene. The graphene was included in a FET structure and the shift of the Dirac point, the point where the conductivity between source and drain is the highest when the gate voltage is swept across a voltage range, was monitored showing a left shift in the presence of ammonia and a right shift when degassed. It was observed that adsorption occurs quickly on the outer surface of the graphene and much slower on the interface with the underlying dielectric. Using mechanically exfoliated graphene with very few defects, the measured adsorption corresponds to theoretical values of pristine graphene. Dan et al. [167] found contaminated graphene to be more reactive with gaseous vapours after a photoresist removal during the device fabrication process. The device showed no response after a cleaning process where the graphene was treated in a high temperature and H_2/Ar atmosphere. It was concluded that the enhanced reactivity to vapours comes from functionalization introduced by residues of the photoresist which dope the graphene. Levesque et al. [168] investigated the interface of graphene and the underlying dielectric further. It was found that switching the dielectric material alters the water vapour and oxygen response. They were able to minimize the effect of water using parylene, a CVD deposited aromatic polymer, as the dielectric material. A tuned dielectric was suggested in order to enhance the selectivity of the graphene gas sensor. Denis et al. [169] investigated various defects existing in graphene using density functional theory calculations, which concluded defects increase the reactivity. The increase in reactivity depends on the functional group that is attached at the defect and the number of functional groups being attached. Hydrogen, fluor and phenyl groups were investigated for reactivity and it was found that the most reactive site is a single missing carbon atom in the lattice and the least reactive one is pristine graphene.

Recently, Liu et al. [170] investigated the adsorption process on graphene in more

detail. A model was derived to distinguish adsorption at defect sites and intrinsic adsorption directly on the carbon lattice. A graphene FET was operated using a quasi-static gate voltage in the linear region of the transistor. By reading out the DC and the AC current simultaneously using a lock-in-amplifier, they are able to extract the carrier density and the field effect mobility at the same time. With these two values, it was possible to distinguish if a single point impurity defect is compensated or if lattice adsorption took place. This showed that the defect induced adsorption is taking place before any lattice adsorption as the defects show stronger reactivity to the gases. Chemical compensation (having a steady concentration of a different kind of gas than the one to be measured in the background) allows measuring pure intrinsic adsorption. As different gases react differently with the point defects and the lattice, Liu et al. also proposed a way to enhance the selectivity of graphene by analysing these two types of adsorption on to the lattice.

The main body of work in this field focuses on theoretical models that aim to describe the adsorption behaviour of various gases. With the work of Liu et al. [170], an experimental approach has been found to explain the adsorption process of gases on the graphene. Previous experiments have showed a more generic approach where basic charge transfer is experimentally shown. In addition, the change of performance due to different architectures of the device does not enhance the understanding of the adsorption process on the graphene.

The work done here to investigate the sensing mechanism in percolating films is primarily focused on enhancing and improving the understanding of sensing mechanisms. As it has been shown that adsorption primarily happens at the contacts between the flakes, the investigation of the adsorption process at defects and lattice adsorption can be neglected in these films (Figure 2.21 illustrates the sensing behaviour in percolating films). The analysis of the desorption at different temperatures proposes a way on how to experimentally measure the bonding energy proposed in the vast numbers of DFT calculations in the field, contributing to the understanding of the molecule-graphene interactions.

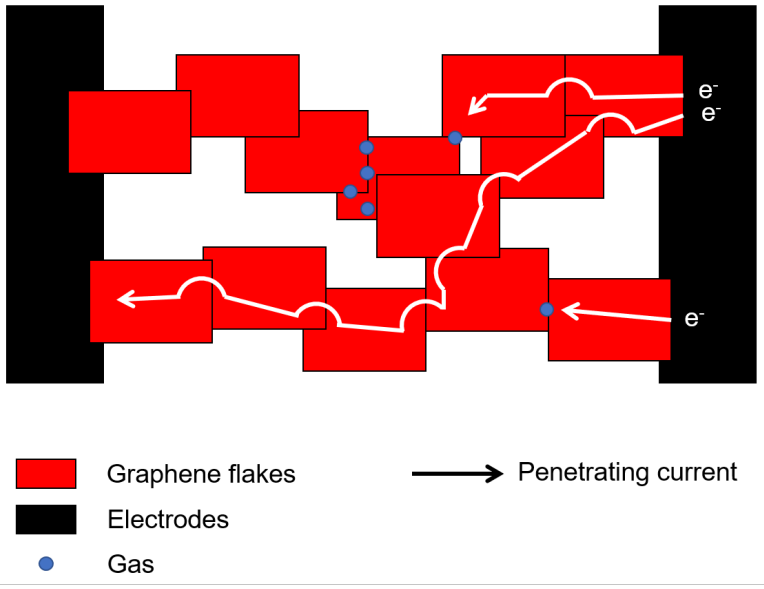

Figure 2.21: Sensing mechanism in percolating graphene films. The current can be considered to only change when crossing between individual graphene flakes. A adsorped gas molecule at the edge blocks the current forcing it to look for a different path to reach the other electrode, therefore changing the conductivity of the entire film

2.4.2 Gas sensing with carbon foams

In the literature, two terms are used to describe the porous volumetric structure of carbon, namely carbon foam and aerogel. If strictly applied, all these porous systems should be defined as aerogels as a foam is by definition air or liquid completely trapped by a surrounding solid. SEM images of the porous forms show open structures which are, by definition, aerogels. Other definitions within the field distinguish the systems by the pore size, defining materials with micropores and nanopores as foams and aerogels respectively. However, this is not consistently followed in the literature and there is no industry standard for it. In this overview, the nomenclature given in individual literature is used.

There has been limited investigation into porous volumetric carbon structures for gas sensor applications. The first measurements using carbon foams were reported by Yavari et al. [171]. A foam structure using few-layer graphene sheets was used as a chemiresistor. Exposure to ammonia and nitrogen dioxide led to two opposite responses of the network. By measuring the resistance in pulses they were

able to joule heat the system between the pulses which enhanced the desorption process resulting in the foam recovering back to its baseline. These workers contacted the carbon foam using silver paste as electrodes. Liu et al. [172] functionalised graphene aerogel made from graphene oxide with SnO_2 nanoparticles to enhance the performance and the selectivity to NO_2. The porous structure, working at room temperature showed enhanced performance by 2 % compared to a SnO_2 only device which requires an operational temperature of 200 °C exposed to 10 ppm NO_2. For specific applications such as toxic or flammable gas detection, low temperature operating devices are advantageous in order to avoid introducing energy into the toxic system to make it more reactive. The research used a tube painted with the active materials as the experimental setup. Li et al. [173] used Co_3O_4 functionalised carbon foam to measure gaseous ethanol at 15 ppm. The dandelion-like nanostructures were added to the freestanding carbon structure by soaking the carbon in a nanoparticle suspension. In order to prepare the sensor, the nanomaterials were mixed with a solvent to create a suspension which was drop cast on the electrodes. This resulted in improved gas sensing performance with the hybrid structure compared to straightforward Co_3O_4 semiconductor materials. Co_3O_4 is a metal oxide which are proven to have high sensitivities towards gases as at elevated temperatures they form depletion layer on the surface where gas molecules undergo adsorption. Adding a more sensitive material to an already sensitive material increases the sensitivity of the overall structure. Comparative ethanol concentration measurements were made by heating the devices to elevated temperatures above 200 °C, which does not change the limit of detection but increases the response to 100s of ppm. In another structure, Li et al. [174] took SnO_2 nanocrystals and incorporated them into a graphene aerogel to detect nitrogen dioxide, measuring the sensor response at 55 °C and 70 °C. The sensor was manufactured in the same way as previously, by drop casting a suspension on to electrodes. This work is comparable to Liu et al. [172] with the difference of using rGO rather than GO and modified nanocrystals. Comparing the performance of the two does not show significant differences between the systems.

Liu et al. [175] also incorporated Fe_3O_4 nanoparticles into a graphene aerogel. The Fe_3O_4 functionalised foam showed an enhanced response compared to the raw rGO aerogel. Introduction of ZnO into a graphene aerogel was also shown to improve

the sensor response at room temperature compared to ZnO on its own [176].

Li et al. [177] have continuously improved their Co_3O_4 functionalised graphene aerogel. Whereas previously, the limit of detection was 15 ppm of ethanol, the improved sensor can detect 0.2 ppm at 100 °C. The crucial change lies in the structure of the Co_3O_4 material, where 2-D like sheets were used, rather than micro-sized particles which greatly increased the surface area.

Long et al. [178] synthesised a hybrid aerogel using a graphene scaffold and MoS_2 sheets. The limit of detection for nitrogen dioxide was 50 ppb at room temperature and at 200 °C. The speed of adsorption and recovery after exposure decreased with increasing temperature to under one minute at 200 °C. The selectivity was significantly improved by incorporation of the MoS_2 sheets.

It can be shown that drop-cast techniques are used for the majority of these applications. This method is not ideal for aerogel deposition unless they are mechanically stable. If this is not the case, the volumetric structure of the foam is likely to be disrupted by capillary forces in the liquid a reduction of surface area and, therefore, device performance. Initial research investigating the use of foam for gas sensing is limited as it is explicitly stated that all the measurements were made with one single device which does not demonstrate repeatability. In addition, while the performance of some of these structures are promising (such as the 50 ppb sensor from Long et al. [178]), currently the devices are manufactured using methods which are not practically scalable for large scale applications.

Material	Gas	LOD	t_{90}	Ref
Few layer graphene	NO_2 NH_3	20 ppm 20 ppm	400 sec 400 sec	[171]
Graphene oxide with SnO_2	NO_2	10 ppm	350 sec	[172]
Carbon foam with Co_3O_4 metal oxide	Ethanol	15 ppm	44 sec	[173]
Graphene aerogel with SnO_2 metal oxide	NO_2	14 ppm	-	[174]
Graphene aerogel with Fe_3O_4 metal oxide	NO_2	30 ppm	275 sec	[175]
Graphene aerogel with ZnO metal oxide	NO_2	10 ppm	149 sec	[176]
Carbon foam with Co_3O_4 metal oxide	Ethanol	0.2 ppm	50 sec	[177]
Graphene scaffold with MoS_2	NO_2	0.05 ppm	10 min	[178]

Table 2.4: Summary carbon foam device performance.

2.5 Carbon foam supercapacitor

Carbon foam has been incorporated into supercapacitor structures by either synthesizing the porous structure or by using the carbon foam as a scaffold for an additional material to boost the specific capacitance. In this section, plain carbon foams in supercapacitor applications are discussed before an overview of scaffold carbon foam is given.

Carbon foam was first used for supercapacitor applications by Mayer et al. [131], measuring around 20 $F\,g^{-1}$ in an aqueous electrolyte. A pressure chamber was used to replace acetone with CO_2 from their chemical synthesis step to achieve the porous structure. Xue et al. [179] created carbon foam using GO as a precursor. The sample was then freeze-dried before being doped with nitrogen. This showed carbon based electrodes are able to replace metal based counter electrodes in energy storage devices when using an organic electrolyte. Fan et al. [180] prepared carbon foam from a biomass precursor in a cost-effective one step carbonization and activation step. This achieved 336 $F\,g^{-1}$ in an organic electrolyte. Sui et al. [181] created nitrogen doped graphene aerogel in a hydrothermal process using GO and ammonia which resulted in a 3-D porous structure with a specific surface area of 830 $m^2\,g^{-1}$. 223 $F\,g^{-1}$ was reached during cyclic voltammetry in an aqueous solution.

Chen et al. [182] fabricated carbon foam from a melamine foam which was then carbonised and nitrogen doped. A gravimetric capacitance of 238 $F\,g^{-1}$ was reached in an aqueous solution. Sawant et al. [183] created carbon foam in synthesis from melamine foam which was then frozen and dried before being calcinated resulting in a nitrogen doped carbon foam. This achieved a gravimetric capacitance of 799 $F\,g^{-1}$ and reached 80% retention within 1500 cycles. Xin et al. [184] used a liquid foam template to create nitrogen doped carbon foam. An activation process using potassium hydroxide (KOH) increased the specific surface from 207 $m^2\,g^{-1}$ to 1120 $m^2\,g^{-1}$. This increase in surface area resulted in an increase by a factor of 3 to 182 $F\,g^{-1}$ when KOH was used as the electrolyte. Woodward et al. [185] created carbon foam with an emulsion template. This reached 1820 $m^2\,g^{-1}$ specific surface area which resulted in a specific capacitance of 26 $F\,g^{-1}$.

Miller et al. [186] were the first to functionalise the foam using ruthenium to increase the gravimetric capacitance from 96 $F\,g^{-1}$ of the plain aerogel to 200 $F\,g^{-1}$ with the functionalised material using H_2SO_4 as the electrolyte. Fan et al. [180] deposited polyaniline (PANI) on to a porous carbon monolith. This hybrid structure reached a specific capacitance of 2200 $F\,g^{-1}$. The large specific capacitance was associated with surface enhancement caused by the electrodeposition of PANI on to the carbon foam. Fischer et al. [187] used two different pH values during their deposition method to put down MnO_2 on carbon foam. This doubled the specific capacitance of the initial foam to 110 $F\,g^{-1}$ when functionalised with MnO_2 at neutral pH. Spanakis et al. [188] functionalised laser deposited carbon nanofoam with gold particles using sputtering. This increased the specific capacitance from 40 $F\,g^{-1}$ to 140 $F\,g^{-1}$ in an organic electrolyte. He et al. [189] deposited nitrogen doped CNTs on to a carbon foam scaffold using a CVD method. The addition of the CNTs led to an increase in specific capacitance of up to 120 $F\,g^{-1}$ using KOH as electrolyte. Chen et al. [182] introduced nanoparticles into their foam structures, whilst investigating synthesis of carbon foam for supercapacitor electrodes. Use of $NiCo_2S_4$ nanoparticles increased the specific capacitance from 238 $F\,g^{-1}$ to 1089 $F\,g^{-1}$. Zhang et al. [190] constructed a foam architecture using carbon nanofibers, melamine and graphene oxide which formed a nitrogen doped carbon aerogel. The porous structure maintained its gravimetric capacitance around 250 $F\,g^{-1}$ after multiple compression steps

Method	Capacitance [$F\,g^{-1}$]	Electrolyte	Ref
Chemically derived	20	aqueous	[131]
Carbonization of biomass precursor	336	organic	[180]
Graphene aerogel	223	aqueous	[181]
Carbonization of malamine foam	238	aqueous	[182]
Freeze drying and carbonization of malmine foam	799	aqueous	[183]
Templated carbon foam	182	aqueous	[184]
Templated carbon foam	26	aqueous	[185]
Carbon nanofoam	40	organic	[188]
Pt functionalised aerogel	200	aqueous	[186]
PANI functionalised pitch carbon foam	2200	aqueous	[180]
MnO_2 functionalised carbon foam	110	aqueous	[187]
Gold functionalised carbon nanofoam	140	organic	[188]
CNT functionalised carbon foam	120	aqueous	[189]
$NiCo_2S_4$ functionalised carbon foam	1089	aqueous	[182]
Carbon nanofibers, malamine GO aerogel	250	aqueous	[190]

Table 2.5: Summary carbon foam supercapacitor performance.

showing robust mechanical behaviour.

Table 2.5 summarizes the various methods and the performance of the carbon foams in supercapacitor applications. It can be seen that carbon alone does not reach the highest values. More often a functionalisation of the foam is necessary to reach high levels of specific capacitances. In order to get these high values the synthesized structures need to be robust and the pores need to be consitently accessible.

Chapter 3

Commercial Graphene Ammonia Gas Sensor Based on a Scalable Manufacturing Process

3.1 Introduction

The occurrence of ammonia is common as it is a byproduct of many industrial processes. Ammonia is a side product of fermentation processes in the food industry [191], a major component in fertilizer production and is used directly as a feedstock material in chemical processes [192]. However, concentrations of ammonia in the air are a concern for many environmental agencies as it is a pollutant [193]. Low concentrations in the parts-per-million range can lead to serious human health effects [193, 194]. At higher concentrations, ammonia becomes explosive presenting a security threat [192]. The presence of ammonia in many different processes requires accurate concentration measurements. A plethora of device structures has been proposed to achieve these measurements [191]. In recent years nanomaterials, in particular graphene, have found their way into ammonia gas sensing devices [154, 155, 158, 166, 192, 195–198]. The simplest device architecture is a chemiresistor structure that utilizes the electrochemical interaction between a target gas and the sensitive material to measure a concentration via the change in device conductance [192]. There are reports where pristine graphene has been incorporated into device structures for ammonia sensing applications. Chemiresistors based on

exfoliated graphene have been shown [166] as well as devices based on CVD-grown material [195]. Significant advances have been made using reduced graphene oxide for this purpose [55, 199]. Reduced graphene oxide is a good sensing material due to its oxygen functional groups at the many defects and edges where targeted gas can interact with. Adsorption at these sides leads to doping of the active material, therefore a change in conductivity [200].

The fabrication of graphene-based devices often involves process steps that are prohibitively complex or expensive, preventing scaling of device production and widespread adoption. Here we demonstrate a device fabrication approach based on liquid-phase exfoliated graphene. Liquid-phase exfoliation is a scalable manufacturing method for producing high-quality graphene sheets [63], which has resulted in commercial availability of readily processable graphene materials. Gas device architectures produced using these materials have been proposed using methods such as screen printing onto electrodes [161] as well as a Langmuir-Schaefer transfer of exfoliated platelets [201]. We recently proposed a device fabrication for gas sensor devices based on laser ablated interdigitated electrodes (IDE) and a Langmuir-Schaefer transfer, which are both scalable methods [196]. We reported the sensing mechanism in percolating graphene films. Whereas in rGO films the basal plane doping from defect/edge binding is the dominant sensing mechanism inter-sheet tunnelling effects are responsible as sensing mechanism for Langmuir graphene films. The pristine structure with few defects allows this effect to have such a large influence. Here we investigate in the performance of these films when exposed to ammonia, a study missing in the previous work.

3.2 Experimental

The substrate material used was a sputtered thin film of molybdenum on glass purchased from AimCore Technology (Hsinchu 30351, Taiwan). An MSV-101 (M-Solv Ltd, UK) laser-processing platform was used to pattern an interdigitated electrode design into the thin metal film using a galvanoscanner and a pulsed infrared laser (1064 nm, Multiwave, set to 150 kHz repetition rate, 10 ns pulse length) with a fluence of 3 $\mathrm{J\,cm^{-2}}$ at a mark speed of 1000 $\mathrm{mm\,sec^{-1}}$.

The Mo-coated glass is supplied as 300mm x 400mm sheets with a price of $10's per piece. The MSV-101 can pattern a 1cm^2 IDE in approximately 1s and automatically pattern a full sheet with 100s of IDEs. Device singulation can be performed by a conventional or laser-based "scribe and crack" process. IDE production by this method is cost-effective and scalable to automated high-volume manufacturing.

Commercial graphene from Cambridge Nanosystems (Cambridge, UK) was purchased as a 1 mg mL^{-1} dispersion in isopropanol. 600 μL of the dispersion was spread drop-by-drop onto the water sub-phase of a Langmuir-Schaefer trough (NIMA 102A) with an initial area of 72 cm^2. The barriers were closed to compress the Langmuir film to a final area of 22 cm^2. The interdigitated electrode was used to pick up the densified graphene film using the horizontal (Schaefer) approach. The devices were left to dry at room temperature.

The cost of the graphene flakes needed to make a device is approximately $1.50. Langmuir deposition processes are easily automated using conventional robotics, indeed tools are commercially available from vendors such as KSV NIMA. Thus, the graphene deposition process is also cost-effective and scalable. For volume production the sensors could be connected to the read electronics by, for example, flexible printed circuit (FPC) bonding via asymmetrically conductive adhesive film (ACF). Apart from the Langmuir Schaefer transfer, all these techniques are used routinely on a fully commercial basis in the M-Solv printed electronics manufacturing facility. This factory operates on a foundry basis and with the addition of an L-S tool would be suitable for volume production of these sensors.

Raman was performed using a Renishaw inVia microscope with a 5 mW, 532 nm solid-state laser, x20 objective, 10 second integration time. A Bruker Dimension Icon atomic force microscope (AFM) was used in peak force mode to measure the topography of the graphene flakes. Samples were imaged with a Zeiss SIGMA field emission gun scanning electron microscope (FEG-SEM) using a Zeiss in-lens secondary electron detector. The FEG-SEM working conditions used were 2.5 kV accelerating voltage, 20 μm aperture, and 2 mm working distance.

The sensor device was mounted in a gas measurement system based on Alicat mass flow controllers, nitrogen and a pre-diluted (100 ppm) ammonia nitrogen mixture (schematic shown in Figure 3.1). The sensor was placed in a measurement

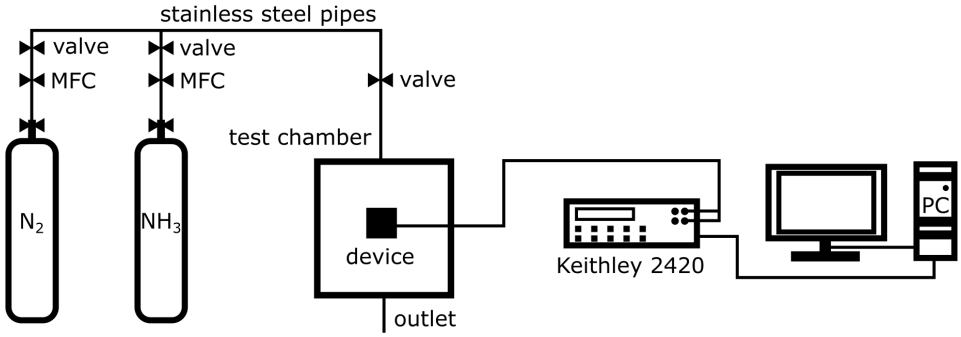

Figure 3.1: Measurement setup for testing chemiresistor devices.

chamber and connected to a Keithley 2420 which was controlled by LabView. During the measurement the device current was kept constant and the voltage was measured. Prior to exposure, the measurement chamber was purged for 10 minutes with nitrogen until the sensor signal reached steady state. Using the mass flow controllers small concentrations of ammonia were added to the nitrogen flow. The devices were exposed to ammonia for 10 minutes and purged for 10 minutes before the next measurement.

3.3 Results and Discussion

An optical micrograph of the laser ablated interdigitated electrodes is shown in Figure 3.2a. The metal is completely removed and straight trenches are visible with a track width of 28 μm. A SEM micrograph of the deposited graphene is shown in Figure 3.2b showing a percolating network of small graphene platelets in between the electrodes on the glass. The average flake size is 300 nm. The Raman spectrum of the graphene is shown in figure 3.2c, with a D-peak at 1340 cm^{-1}, a G-peak at 1571 cm^{-1} and a 2D peak at 2678 cm^{-1}. The D/G peak ratio suggests either a high number of basal plane defects in the graphene sheets, or that the average lateral size is low (which agrees with the SEM image of Figure 3.2b). The ratio between the 2D and G-peak is below one suggesting that material is multilayered. AFM image shows agglomerations of graphene when deposited on glass with a height of 90 nm when agglomerated and single flakes have a thickness of 9 nm. This confirms the observation in the SEM image of the graphene flakes showing flakes which are not flat on the surface, flakes which seem to stand out of the plane in a wrinkled fashion.

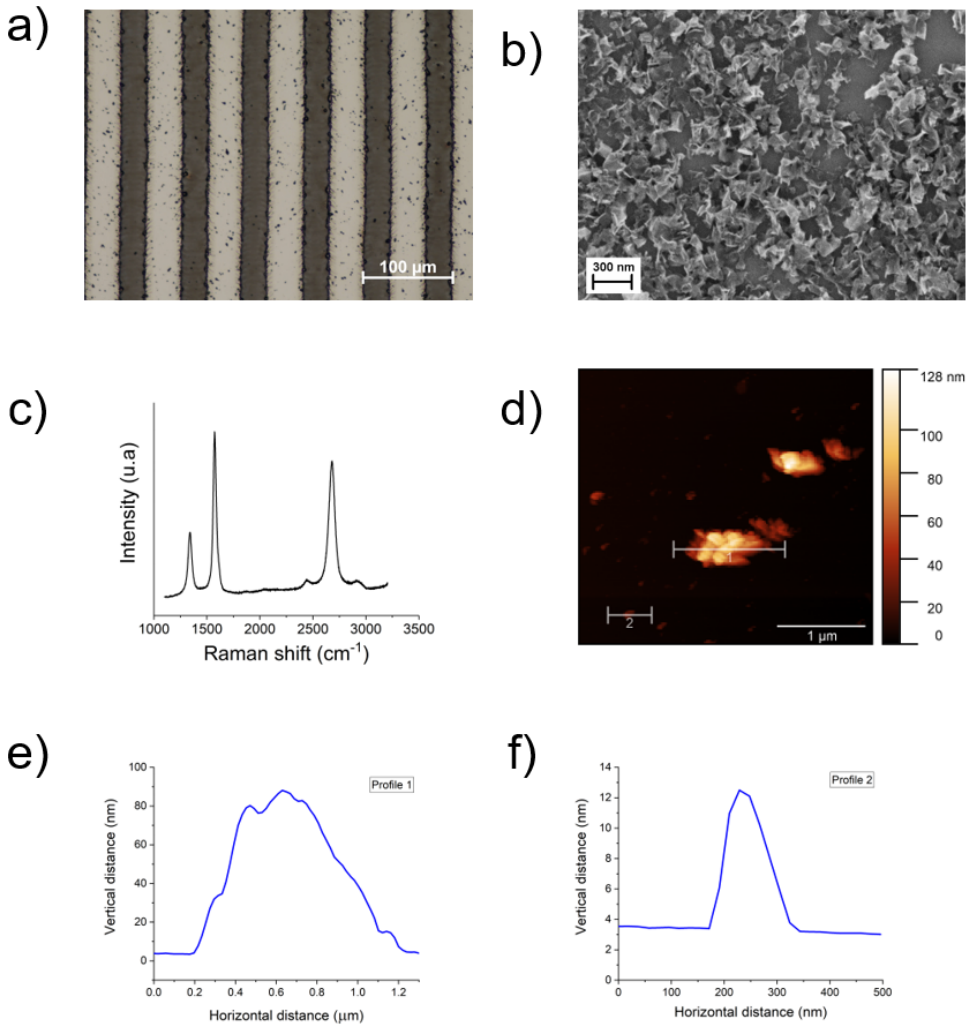

Figure 3.2: (a) shows an optical image of the laser ablated interdigitated electrodes, (b) SEM image of the deposited graphene platelets into the trench of the interdigitated electrodes, (c) Raman spectrum of the deposited graphene platelets, d) AFM topography of graphene flakes, e) height profile of agglomerated graphene, f) height profile of single flake graphene.

Figure 3.3a shows the device response to various concentrations of ammonia. Figure 3.3b shows a sensor response of the device when exposed to 20 ppm of ammonia several times. Figure 3.3c shows a long term exposure of the device at 20 ppm ammonia concentration. There is a drift present in the baseline in all the measurements which has been subtracted out of the data in Figure 3.3c for clarity. The raw signals can be found in Figure 3.4. The drift was subtracted using the trendline function in Excel, where a single straight line was subtracted from the sensor signal.

Further work is required to understand this drift. There are several origins of the drift. Charges trapped in the surroundings of the graphene flakes influence the doping of the graphene flakes [154]. A back-gated transistor structure might help compensating for this effect [202]. A film with less material would also improve the drift as gases and charges can be trapped between the flakes.

The device fabrication yields a well-defined chemiresistor structure with a percolating network of graphene platelets connecting the individual electrodes. The fabrication process is quick; the laser patterning of the IDEs takes of the order of 1 second and the deposition of the percolating film can be done within several minutes. This indicates good process scalability when the device design is downscaled, such that many devices can be prepared in the same fabrication run at the wafer scale.

The smallest concentration resolved is around 750 ppb, and the limit of detection with a signal-to-noise ratio of 3 is around 1 ppm. The sensor response stays constant for several exposures suggesting a good repeatability. The positive drift in the measurements originates from the measurement setup which does not allow enough recovery time for the sensors for multiple exposures. A single long term exposure shows a recovering baseline when purged with pure nitrogen, which suggests no further treatment is necessary to clean the device after exposure, even at room temperature. From the long exposure the response time T_{res}, defined as the period of time needed until 90 % of the sensor response is reached when exposed to a gas, is 90 seconds. The recovery time T_{rec}, defined as the time needed until the sensor signal is reduced by 90 % of its value when exposed to the gas, is 18 minutes. The power consumption of the device is around 12.5 mW which is 50x lower than that used by commercial metal oxide semiconductor gas sensors [203, 204].

This device structure can compete with previously reported graphene-based am-

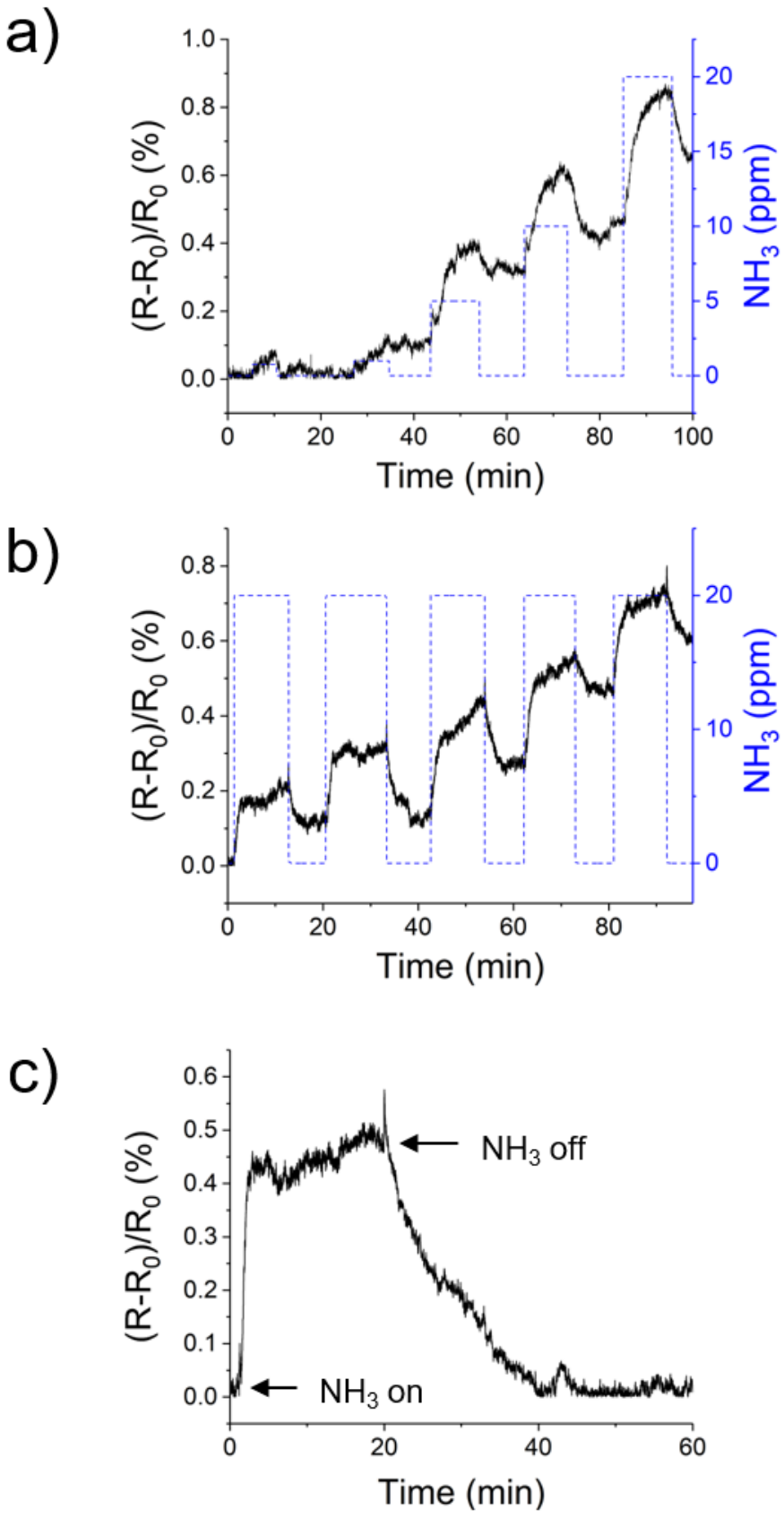

Figure 3.3: (a) Sensor response to various concentrations (0.75, 1, 5, 10, 20 ppm) of ammonia in nitrogen, (b) sensor response to 20 ppm ammonia for several times, (c) long term exposure to 20 ppm ammonia.

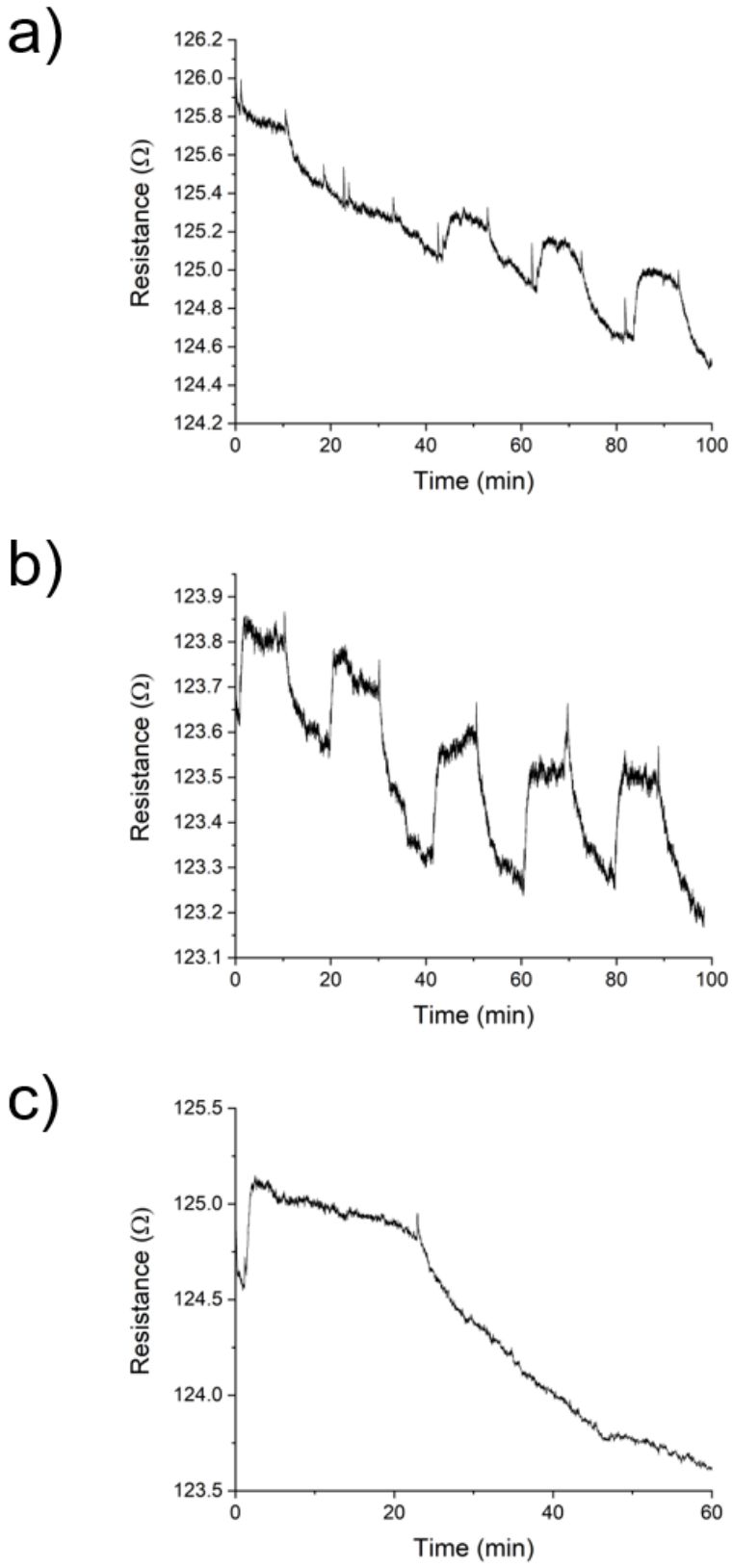

Figure 3.4: a) Raw resistance measurement from limit of detection measurement, b) Raw resistance signal of repeatability measurement, c) Raw resistance signal of long exposure to ammonia.

monia sensors. A measured limit of detection is in the 1 ppm region. Also, the response and recovery time are competitive with other structures [154, 158, 166, 195, 197, 198].

3.4 Conclusion

We have proposed a scalable fabrication process for graphene-based gas sensors using laser ablation and Langmuir-Schaefer deposition of commercial liquid-dispersed graphene sheets. A percolating graphene film creates a chemiresistor structure between interdigitated electrodes. The sensor shows a detection limit of 1 ppm and a repeatable signal. Long exposures suggest the device recovers by itself when purged of the analyte gas. The devices presented have a low power consumption and a simple manufacturing method compared to metal oxide sensors or conventional electrochemical sensors which comprise a can containing multiple macroscopic electrodes immersed in an electrolyte which is contained by a gas-permeable membrane. The performance of the commercially available graphene is comparable with both lab-prepared graphene-based gas sensors for ammonia and the commercially available sensors mentioned above.

Chapter 4

Edge Selective Gas Detection using Langmuir Films of Graphene Platelets

4.1 Introduction

Graphene has shown many potential applications in electronic devices such as solar cells and transistor configurations [205]. It has also shown promising results in electrochemical and bio-sensors [206]. Specifically for gas sensing applications [207] promising results have been demonstrated; such as the detection of individual NO_2 molecules in a Hall bar structure [33], a chemiresistor with an estimated detection limit of 158 ppq (part per quadrillion) [208], or sensor arrays based on reduced graphene oxide which are selective and overcome the problem of device-to-device variations [209,210]. Pristine graphene is known to interact with multiple gases [211], and chemical functionalization of graphene is used to enable selective detection of different gases [212]. Various device structures to characterise the graphene response to gas exposure have been investigated; among them, chemiresistor structures [213] or the transistor configuration [152]. Rumyantsev et al. [152] were able to distinguish applied gases in the low-frequency noise of pristine graphene when fabricated into a transistor configuration. Graphene has also been incorporated into hybrid structures, such as with silver nanowires, for gas sensing [214].

Graphene is becoming a commercially available material, with products con-

sisting of small graphene platelets (of the order of 100 nm to 1 μm) that can be purchased in powder form or as dispersions in a variety of solvents or surfactants. Often graphene applications use exfoliated materials or CVD grown sheets which are transferred to a targeted substrate where further photolithography steps are required to fabricate a device [215]. Materials created with these methods are not yet available in industrial quantities, even though simple one step CVD processes have been demonstrated [216], and photolithography is an expensive method to create electrodes for chemiresistor devices. To make a step towards industrial fabrication of graphene based gas sensors scalable and inexpensive methods of manufacturing electrodes are necessary. Pulsed laser ablation [36] is a fast and efficient method for creating interdigitated electrodes which are required for chemiresistive devices. This method requires structuring the electrodes before the deposition of the sensing material and a scalable method for producing percolating thin films from small-platelet graphene dispersions. Langmuir-Schaefer deposition is a method of controllably producing thin material films on electrodes. Percolating graphene films from Langmuir-Schaefer deposition have been shown [43, 217], as well as the sensitivity of such films to hydrogen [201]. Due to the nature of such networks the electrical resistance is dominated by the inter-sheet resistance rather than the basal plane conductivity of the graphene nanosheets [217]. Here we show that Langmuir-Schaefer deposited commercial graphene platelets on laser ablated IDEs can be used to produce gas sensors in which the signal depends on the change in the contact resistance between the nanosheets in the network. KPFM and Raman spectroscopy are used to analyse the doping of the network and the response of the sensor is characterized using ammonia as an electron donor gas and acetone as an electron acceptor gas.

4.2 Results and Discussion

Figure 4.1a and 4.1b show the manufacturing method of the chemiresistor structure as described in the experimental section 4.4.

Figure 4.1c shows an optical micrograph of the fabricated device where the graphene film connects the individual fingers of the IDE structure. The typical response of the sensor when exposed to NH_3 is shown in Figure 4.2. The resistance of

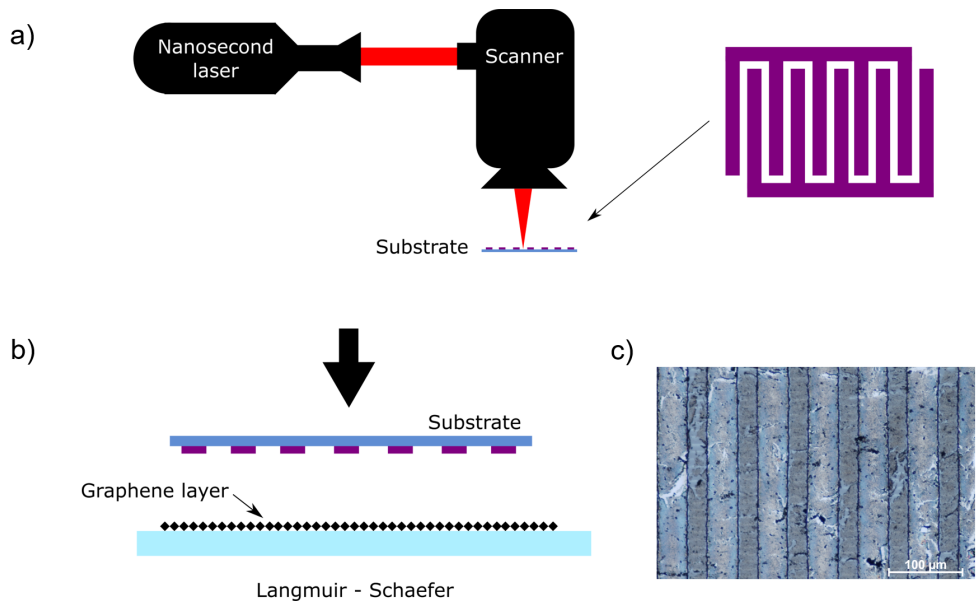

Figure 4.1: (a) Experimental laser setup used to ablate interdigitated electrodes into a metallic substrate. An infrared nanosecond laser is guided into a Galvoscanner which scribes the designed pattern into the substrate, (b) Langmuir - Schaefer was used to directly deposit graphene on to the IDEs, (c) optical micrograph of the fabricated device.

the device increases with increasing concentration of NH_3 but responds consistently when repeatedly exposed to the same concentration. A drift in the sensor signal is visible which is due to desorption processes which happen over much longer timescales than the measurement cycle time. A Langmuir adsorption fitting in the form of $S_0 = S_{max}KP/(1+KP)$, where S_0 is the sensor response, S_{max} is a constant K is an equilibrium constant of the adsorption and desorption, P is the concentration of ammonia. The Langmuir fitting works well for K = 0.005 Pa^{-1}.

Figure 4.3 shows a long-time exposure of the sensor showing the resistance of the device drops back to its baseline when the desorption time is long enough. Figure 4.4 shows the device response to various levels of humidity and it is evident that the device behaves in opposite direction in a humid and in a dry environment. Figure 4.5 shows the difference in response to humidity and when ammonia is applied. Kelvin force probe microscopy [47] was used to determine the doping of the deposited film due to exposure to ammonia.

Figure 4.6a and 4.6b show the contact potential difference before and after exposure to ammonia of the deposited film shown in Figure 4.6c. The shift is quantified in figure 4.6d with the histogram of both exposures.

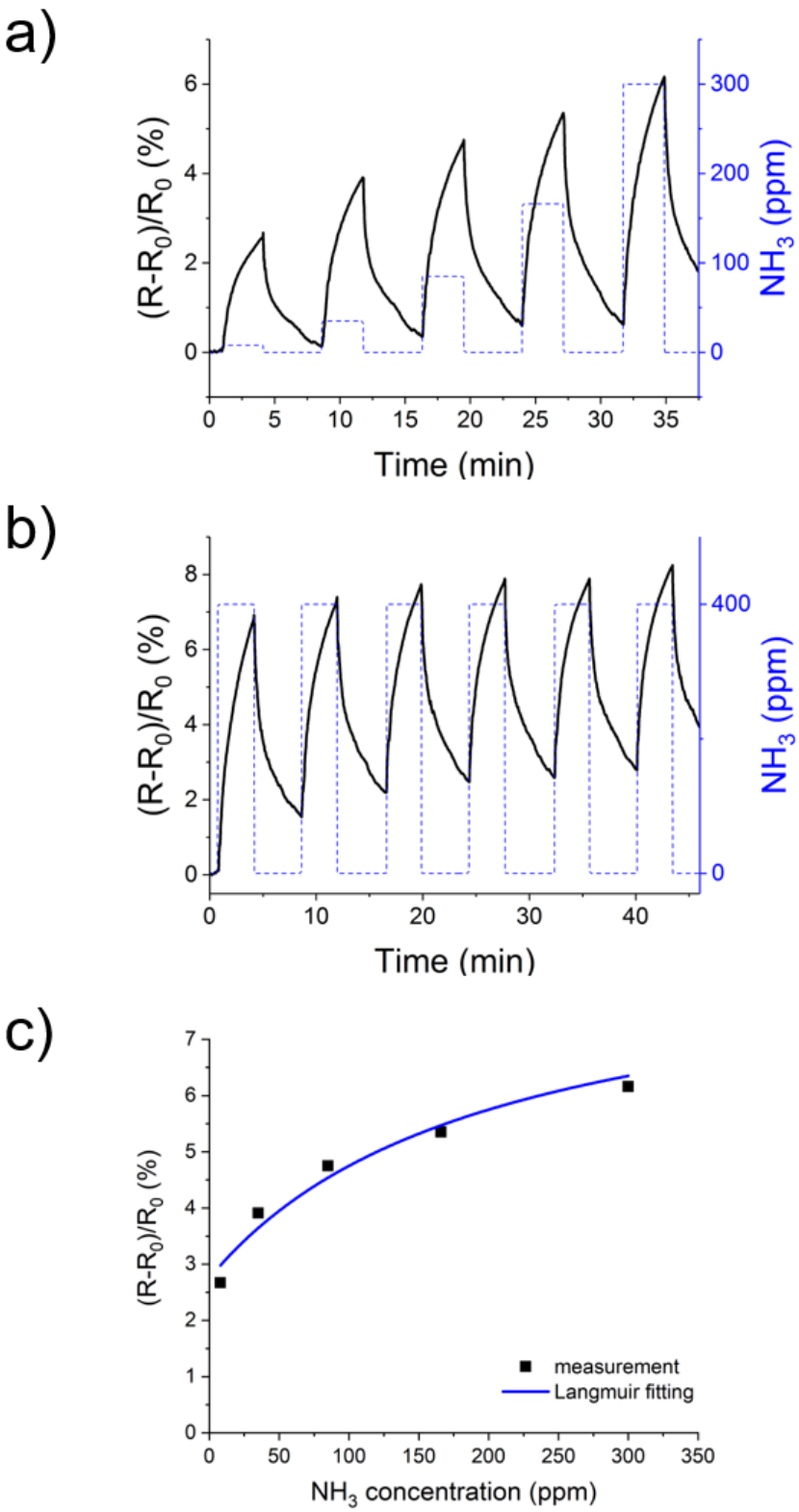

Figure 4.2: (a) relative signal to various concentrations of NH_3, (b) relative signal to a repeated concentration of 400 ppm NH_3, (c) calibration curve of the sensor exposed to differnent concentrations of ammonia, Langmuir adsorption curve fitted into measurements.

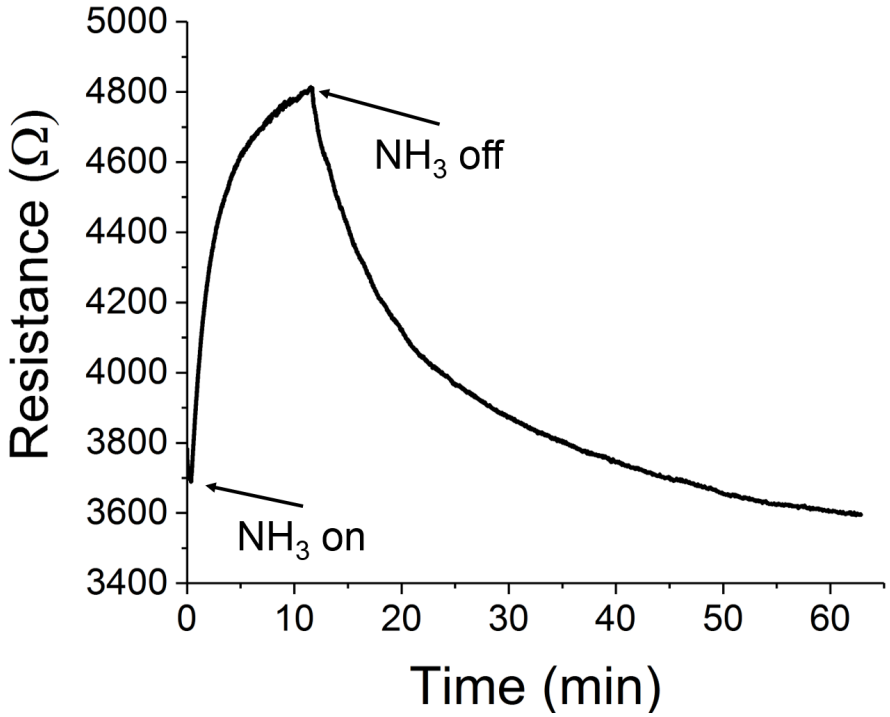

Figure 4.3: Exposure for 12 minutes to 150 ppm NH_3 and a desorption time of 45 minutes after which the device reaches its baseline.

The shift in CPD is around +50 meV showing the work function of the material is lowered. To confirm the doping, Raman spectroscopy was used before and after the exposure to NH_3; see Figure 4.7.

A shift in the D, G, 2D and G' features is visible due to doping; also the D' shoulder in the G peak has become more prominent. The shift in the G peak can be used to calculate the number of molecules adsorbed on the graphene [50] resulting in an estimate of $\sim$1.5x10^{12} cm^{-2}.

Comparing the potential shift from the KPFM analysis and the amount of molecules adsorbed with the dopant analysis of Das et al. [218] the shift of the potential for 1.5x10^{12} cm^{-2} adsorbed molecules is consistent with the 50 meV potential change measured. From the shift of the 2D peak in the positive direction n-doping is confirmed for ammonia exposure [218].

Graphene at room temperature in a humid environment is naturally p-doped due to adsorbed water molecules [151]. NH_3 interacts predominantly with oxygen functionalities and defects in graphene and dopes the basal plane with electrons, thus reducing the number of majority carriers (holes) leading to an increase in sample

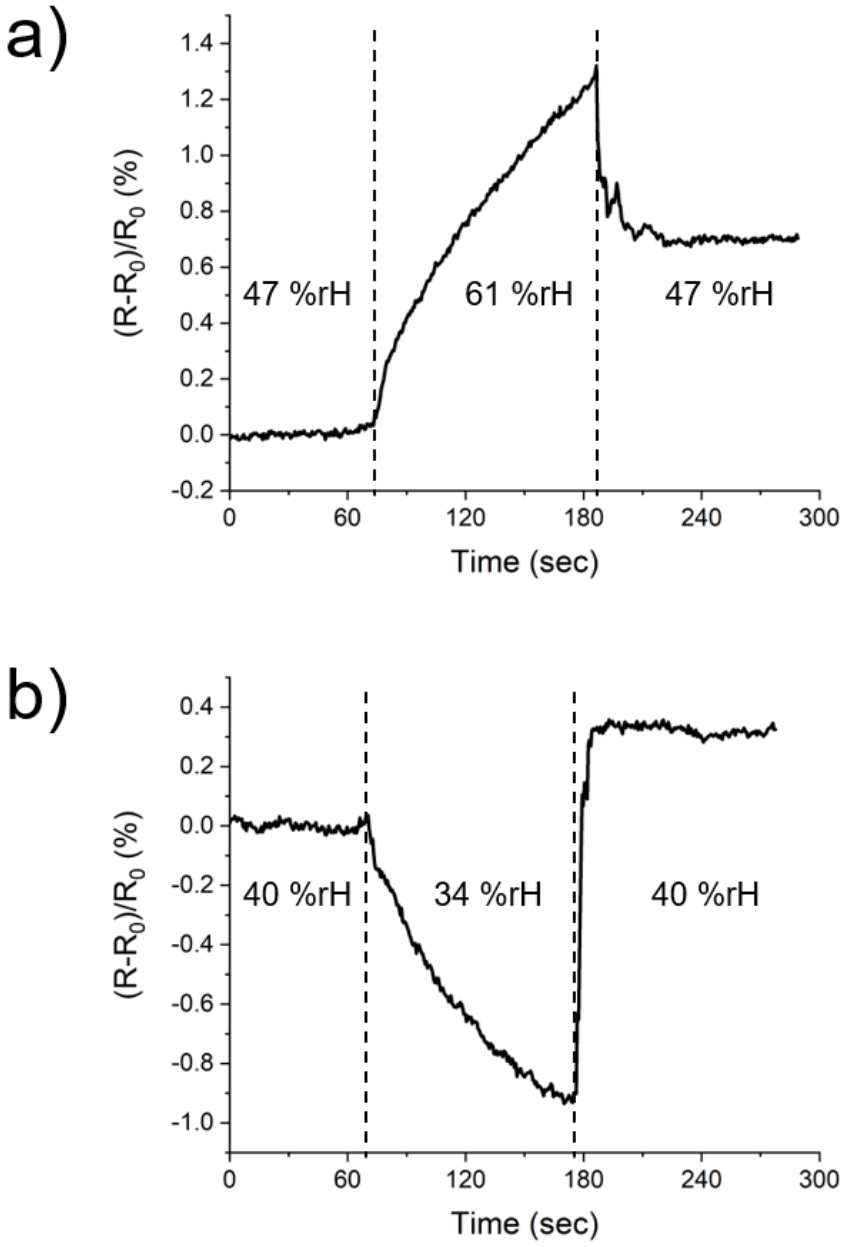

Figure 4.4: L-S device exposed to wet(a) and dry air(b). The device resistance increases when exposed to a humid environment and decreases when exposed to a dry environment.

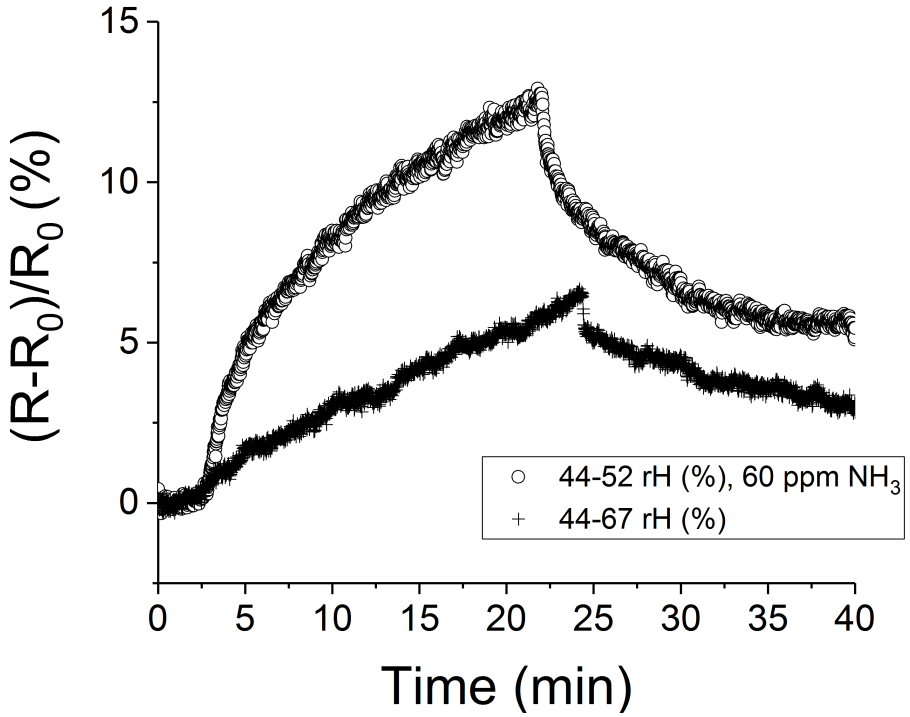

Figure 4.5: Gas device exposure to a change in humidity (rH(%)) and exposure to a change of humidity in the presence of ammonia.

resistance [195] as we have observed and is confirmed by Kehayias et al. [219] who analysed a reduced graphene oxide gas sensor in the same way.

These measurements do not confirm the sensing mechanism yet, as characteristically the conductivity in a percolating network is dominated by the contact resistance between individual particles rather than the bulk resistance of the material. In the case of carbon nanotubes the contact resistance is four orders of magnitude higher than the resistance of the tube itself [220], therefore the contribution of the change in the conductivity upon adsorption at the contacts needs to be considered as well. First-principles studies have shown that the binding energy of NH_3 on graphene edge sites is six times higher than on the basal plane [221, 222]. These values indicate the edge site adsorption is dominant over the basal plane adsorption, both of which contribute to the basal plane charge carrier density.

The ammonia adsorbed on the basal plane induces doping, causing a change in the resistivity of the film. At the edge sites of the percolating graphene platelets the adsorbed ammonia changes the inter-sheet resistance.

Since both the doping and inter-sheet resistance contributions to the chemires-

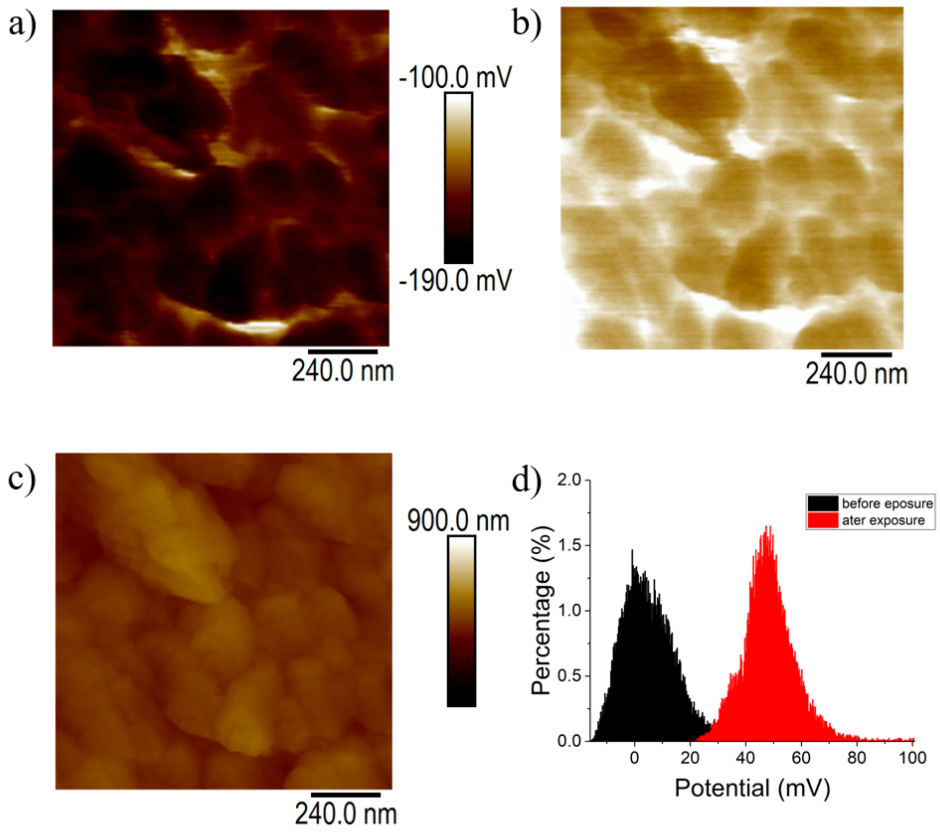

Figure 4.6: KPFM measurements of the surface CPD (a) before exposure and (b) after exposure to ammonia, (c) topography of measured percolating network using AFM, (d) pixel-wise histogram of surface CPD measurements, showing an approximately +50mV shift after ammonia exposure.

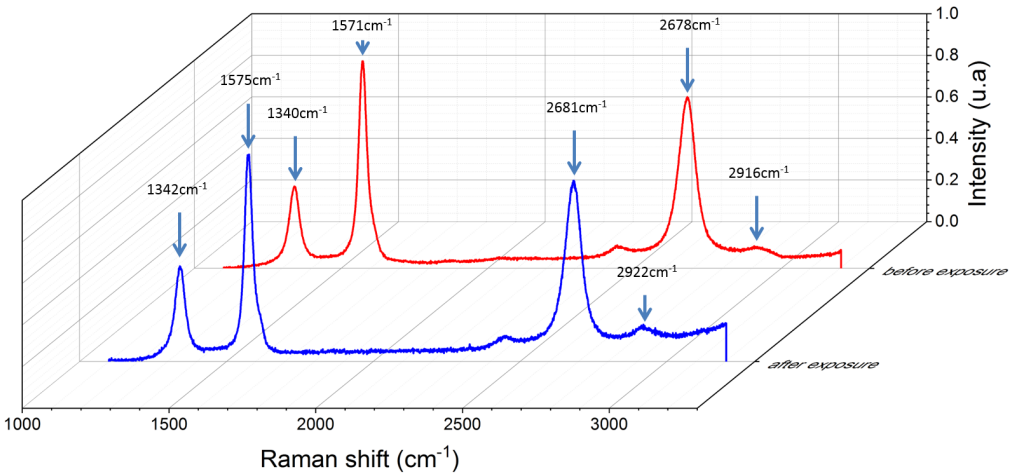

Figure 4.7: Raman spectrum before and after exposure to ammonia. Shifts in the D, G, 2D and G' peaks in positive direction are visible. The shifts correspond to doping of the graphene, the positive shift of the G and 2D peak indicates p-doping of the material and allows to calculate the number of adsorbed molecules resulting in $1.5.x10^{12}$ cm^{-2}.

istance signal act to increase the sample resistance, we cannot directly isolate which contribution is dominant (if either).

In order to understand the relative contributions of doping of the basal plane and inter-sheet resistance changes due to gas adsorption an identical measurement was performed using acetone (which acts as an electron acceptor [223]). Figure 4.8a shows the KPFM analysis of the graphene nanosheets exposed to acetone, alongside a comparable resistance response (Figure 4.8b) to that shown in Figure 4.3.

The potential shift is in the opposite direction to that of the ammonia in Figure 4.6d. Figure 4.8b shows the response of the sensor to acetone exposure. The device resistance is seen to increase despite the increasing density of majority carriers (holes) due to depletion of electrons by the acetone. This indicates that the sensing mechanism is dominated by change in inter-sheet contact resistance rather than doping of the basal plane, as this would show up in a decrease of resistance upon acetone exposure. The phenomenon of dominated response due the edge adsorption has been seen using dielectrophoresis as deposition method for rGO which creates a similar film to L-S deposited ones [224].

The direction of the signal does change when exposed to dry air. Here a different sensing mechanism is taking place compared to the edge adsorption. It is well

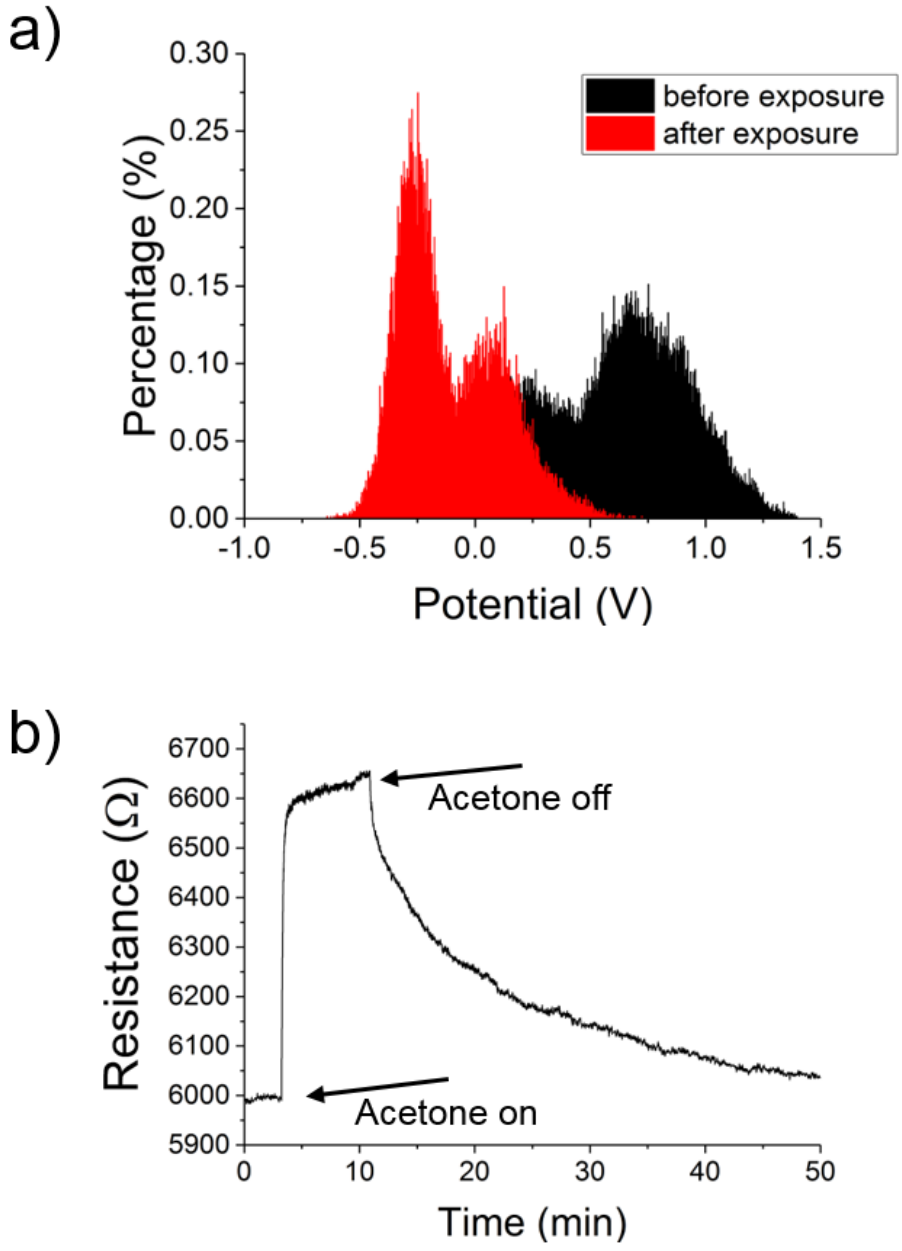

Figure 4.8: (a) Histogram of surface CPD before and after exposure to acetone, measured using KPFM. The peak at 0 V originates from areas of the substrate which were not covered by nanosheets, and which do not shift with acetone exposure. (b) sensor resistance response to acetone exposure.

known that carbon materials at room temperature form a continuous water layer on top. [151] The conductivity of the film is strongly influenced by this water layer and changes the conductivity when reduced [225]. The mechanism taking place is based on the Grotthuus chain reaction [226] where the conductivity is dominated by the transfer of a hydrogen atom between the water molecules [227].

The binding energy of a molecule to the graphene can be inferred by exposing the system at different temperatures and fitting an exponential decay function, of the form

$$R = R_0 + \sum_i A_i exp(-k_i t) \tag{4.1}$$

to the desorption response using the least square method. The pre-exponential factors A_i dictate the relative contributions to the sensing response of the processes i each with a rate constant k_i. An example of this fitting to a single device exposure, using two exponential terms, is shown in Figure 4.9a. Figure 4.9b shows fitted rate constant k of the edge adsorption as a function of device temperature plotted as $1/k_bT$, where k_b is the Boltzmann constant and T the absolute temperature.

The Arrhenius function

$$k(t) = A_0 exp(-E_a/(k_bT)) \tag{4.2}$$

where A_0 is a temperature-independent pre-factor, and E_a is interpreted as the binding energy of the contributions of the ammonia molecules to the graphene, is fitted to the measurements taken at different temperatures in Figure 4.9b.

The fitted value for the binding energy in this case is 100 meV. This is broadly consistent with theoretical predictions for the binding energy of ammonia molecules to the edge sites of graphene nanosheets [221]. This measurement confirms that edge-site binding is the dominant contribution to the chemiresistive response of these devices to ammonia exposure.

However, the desorption response is also influenced by the humidity in the measurement chamber which is not directly controlled in our experimental setup. This

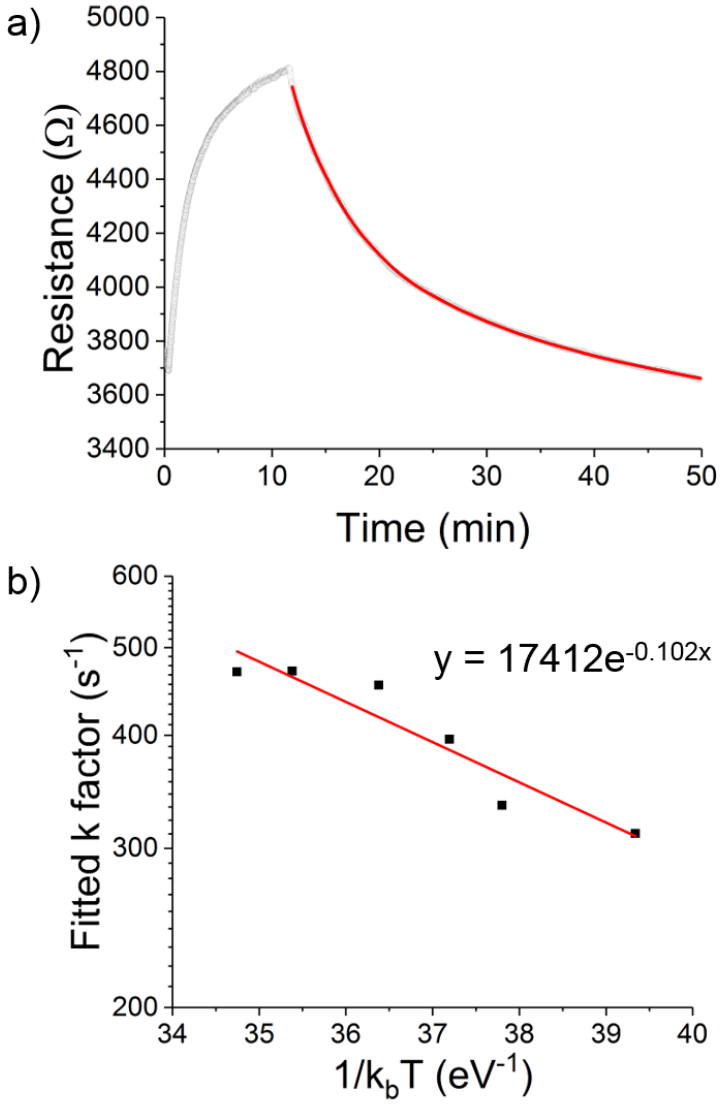

Figure 4.9: (a) Exponential fit to desorption of long term exposure to ammonia, (b) time constants at different temperatures with Arrhenius fit and corresponding equation.

is due to the use of a bubbler as an ammonia source, which limits the accuracy of the binding energy measurement and makes the investigation of other processes more challenging. Nevertheless, this type of analysis is a promising method for understanding microscopic graphene-gas interactions using macroscopic, ensemble measurements.

4.3 Conclusion

We have demonstrated chemiresistive gas sensing by preparing devices using commercially available graphene and scalable production methodologies, such as L-S film deposition and laser electrode manufacturing. We have investigated a sensor structure consisting of percolating graphene platelets deposited using the L-S method.

We confirm electronic doping of the basal plane using KPFM and Raman spectroscopy. Ammonia was found to n-dope the graphene whereas acetone was found to induce p-doping. The measured resistance of the system upon gas exposure to ammonia and acetone increases in both cases. We conclude from this that the inter-sheet resistance is responsible for the change in the resistance of the network rather than the intra-sheet conductivity. Fitting of the time-dependence of the desorption signal as a function of temperature is used to confirm that ammonia binding at edge sites is the dominant contribution to the overall device response. The binding energy obtained from Arrhenius analysis is consistent with predictions from the literature.

Such understanding of the sensing mechanism and response demonstrates the potential of these films both as a platform to study graphene-gas interactions and as low-cost scalable sensors.

4.4 Experimental Section

The substrates used were obtained from AimCore Technology (Hsinchu 30351, Taiwan); these consist of a glass substrate sputtered with molybdenum forming a 700 nm thick metallic layer. The graphene was obtained from Cambridge Nanosystems (Cambridge, UK) in a 1 $\mathrm{mg\,mL^{-1}}$ concentrated isopropanol dispersion (G1 dispersion). An infrared nanosecond laser (Multiwave, set to 10ns, 1064 nm) and a Galvoscanner were used to pattern the IDEs into the metal. The laser was used in focus

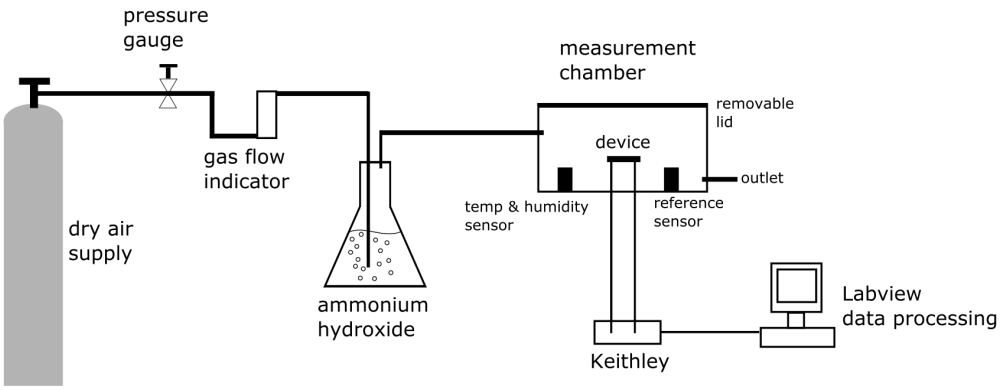

Figure 4.10: Gas bubbler experimental setup.

with a fluence of 3 $\mathrm{J\,cm^{-2}}$ at a mark speed of 1000 $\mathrm{mm\,sec^{-1}}$. The finger electrode pattern was designed in a drawing interchange format (DXF) format created in a computer-aided design (CAD) to feed to the scanner. Graphene films were prepared as described by Fahimi et al. [43] 2 mL of the graphene dispersion was spread onto the water sub-phase to form a Langmuir film at the air-water interface. The film was compressed from an initial area of 450 $\mathrm{cm^2}$ at a rate of 30 $\mathrm{cm^2\,min^{-1}}$ to a final area of 100 $\mathrm{cm^2}$. The IDEs were lowered horizontally into contact with the sub-phase to transfer the compressed film to the device structure. Raman spectroscopy was performed using a Renishaw InVia microscope with a 532 nm solid-state laser, x20 objective, 10 second integration time and 5 mW power.

We setup a gas measurement system using a bubbler and dry air (schematic in figure 4.10) to expose the devices to ammonia which was obtained in a 1 molar ammonium hydroxide solution from Sigma Aldrich. The pressure of the dry air supply was held at 1 bar and the flow rate at 2 $\mathrm{L\,min^{-1}}$. Diluted concentrations of ammonium hydroxide were put into the bubbler to reach different NH_3 concentrations in the measurement chamber. A reference sensor (a1-cbiss (Wirral, UK), GASBADGE PRO, Single Gas Detector, 1 ppm resolution) was used to measure the NH_3 concentration in the chamber. A temperature and humidity sensor was placed inside the chamber to ensure the measurement conditions remained constant. The devices were first exposed to ambient air with open lid and no dry air flow. The lid was closed and the flow regulated. For a short device exposure, the NH_3 concentration was measured after 2 min before the lid was opened to flush the device with ambient air. For a long exposure, the concentration was measured at 2 min and 15

min before the chamber was flushed. A Keithley 2420 and LabVIEW were used to measure the device resistance over time. A small ceramic hotplate was mechanically fixed to the back of the device for exposures at elevated temperatures.

Kelvin probe force microscopy was performed with a Bruker Dimension Icon atomic force microscope system using a platinum-iridium-coated silicon tip in peak force tapping mode using 5 nN contact force.

Chapter 5

Percolating Metallic Structures Templated on Laser-deposited Carbon Nanofoams derived from Graphene Oxide: Applications in Humidity Sensing

5.1 Introduction

It is well understood that laser irradiation can be used to achieve the selective thermal reduction of graphene oxide [111]. The literature discusses the use of numerous laser types and processes to achieve films of reduced graphene oxide with sheet resistance as low as 50 Ω per square [104, 108, 109, 111]. Since this method is inherently selective it can be used to produce patterned structures; [107] such as transistors, [104, 110] supercapacitor electrode geometries [105] and sensor devices [112]. The range of laser fluences used to reduce the GO are typically between 20 $\mathrm{mJ\,cm^{-2}}$ to 400 $\mathrm{mJ\,cm^{-2}}$. In a small window of fluences carbon foam is created as a by-product of the reduction process.

Carbon foam is a low-density, porous form of amorphous nanostructured carbon which can be produced in various morphologies and with different methods. [118] The fundamental formation mechanism is described by Henley et al. [228] Nano-

scale carbon clusters are formed through three processes during the GO reduction: condensation of carbon atoms within the plume of material vaporized by the laser; direct ablation of clusters of the target material, and the subsequent aggregation of smaller clusters. These carbon clusters then grow by the attachment of single carbon atoms. The formation occurs outside of the initial shock wave created by the laser when ablating the target, where the carbon starts to diffuse. Deposition within the shock wave would lead to a dense graphitic film. The individual clusters are formed of between 15 % and 45 % of sp3 carbon, with the sp3 bonding prevalent at the cluster surface; this surface structure is responsible for the bonding between individual clusters [16]. At the nanoscale the assembled clusters form a fractal morphology, with the microscale structure having a web-like appearance.

Rode et al. [16] described the formation of a fractal carbon foam, during the laser ablation of a carbon target, with similar properties to Schwarzites. Rode et al. subsequently coined the phrase "carbon nanofoam" to describe this type of material [229]. Munoz et al. [230] reported clustered carbon foam formation during ablation of an organometallic gold salt in air under ambient conditions, which led to the production of a nanocomposite with gold particles enclosed within the carbon clusters. Zani et al. [231] investigated pulsed laser deposition of carbon foam onto silicon achieving a uniform film across 1 μm^2. Spanakis et al. [188] investigated the use of CNF for preparation of supercapacitor electrodes. They sputtered 2 nm thick gold layers on to the CNF electrodes to enhance their specific capacitance up to 130 F g^{-1}.

The high specific surface area of the CNF makes it an ideal material for sensing applications. The conductivity of carbon materials in sensing applications is strongly influenced by changes in humidity [209, 232–234]. Especially in gas sensing applications humidity results in cross-talk and reduces selectivity of the materials. In order to enhance selectivity the influence of humidity on the materials' response needs to be reduced. One well known method for achieving this is the use of metal functionalisation [55, 235].

In the present work, we investigate the conductivity response of pristine CNF and materials decorated with gold nanoparticles when exposed to changes in humidity. The CNF was deposited using a pulsed infrared laser and a GO target.

Upon decreasing the humidity the conductivity of the pristine CNF decreases due to desorption of water ions from the surface. By contrast, the conductivity of the gold-coated CNF increases when the humidity decreases due to the reduction of depletion regions induced by the adsorbed water on the gold coating. At the percolation threshold of the metallic coating the two counteracting sensing mechanisms appear to cancel each other out, making the CNF insensitive to changes in humidity. This first presentation of CNF for sensing application shows how tuned functionalisation can eliminate cross-talk of humidity in a sensing device.

5.2 Results and Discussion

Atomic force microscopy in Figure 5.1a of the as-received GO material reveals a flake size between 500 nm and 1 μm and a uniform flake thickness of 2 nm. The Raman spectra of the GO after initial heat treatment and the rGO after laser treatment are shown in Figure 5.1b. Figure 5.1c and 5.1d show the window of laser fluence where CNF is formed during the reduction of the GO. In Figure 5.1c the GO is heat treated to various temperatures, whereas in Figure 5.1d the thickness of the deposited GO film before reduction is changed and then heat treated to 250 degrees. The window of fluence where CNF formation is observed appears to be invariant under these different experimental conditions. CNF is only formed in a window of fluences, independent of the substrate processing. The sheet resistance of the rGO is not influenced by the production of the CNF. At low fluences the laser shows no interaction with the GO. At fluences above the CNF production window the ablation threshold of the GO is overcome and clear laser ablated trenches are produced.

The process of depositing the CNF onto a substrate with interdigitated electrodes is illustrated schematically in Figure 5.2. Laser ablated electrodes on glass are separated by an uncoated region so the laser is able to shine through the transparent substrate (Figure 5.2Ai). The GO is transformed into CNF from the interaction with the laser (Figure 5.2Aii) and is deposited onto the electrodes. By scanning the laser up and down the entire electrode areas are covered with CNF (Figure 5.2Aiii). Figure 5.2Aiv shows the electron micrograph of material deposited on pre-patterned electrodes. Figure 5.2Bi illustrates the functionalization process through sputtering

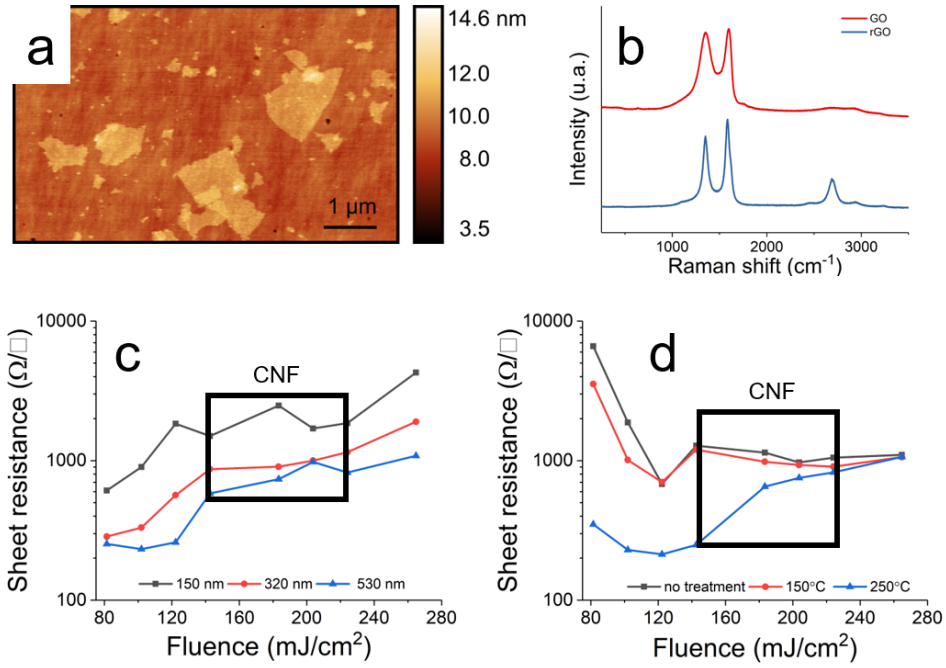

Figure 5.1: a) AFM image of synthesized GO, b) Raman spectra of heat treated GO and laser reduced GO, c) Sheet resistance of rGO for various fluences where the thickness of the GO was changed, inset window shows where CNF occurring, d) Sheet resistance of rGO for various fluences where the temperature treatment of the GO is changed, inset window shows where CNF occurring.

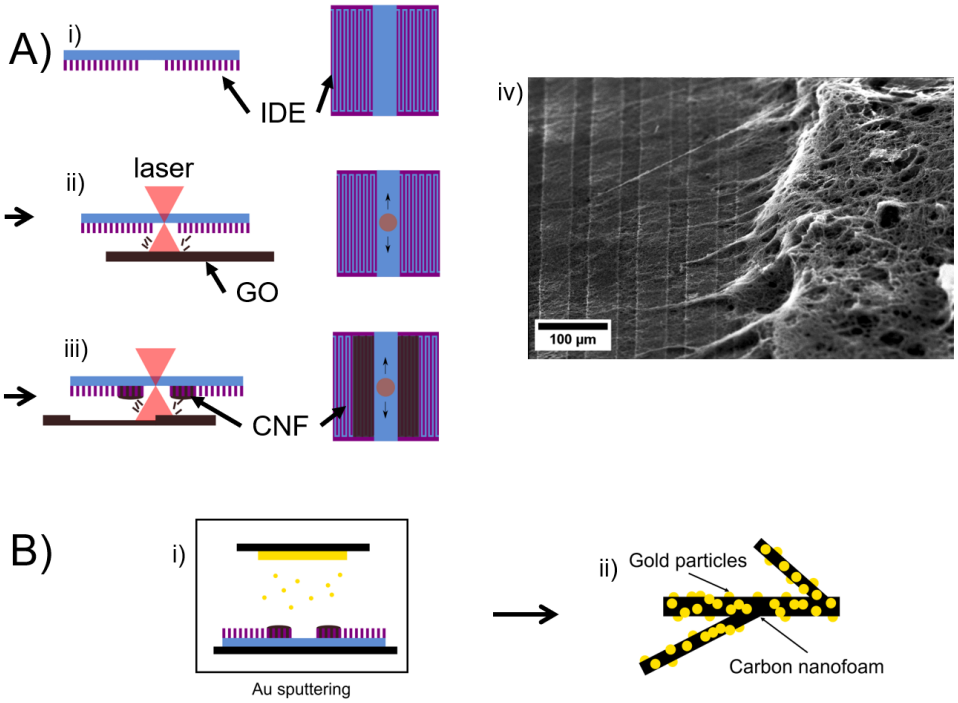

Figure 5.2: Ai) Schematic of laser ablated electrodes on glass substrate where the electrodes are separated in two parts so the laser can go through the glass to ablate the GO target beneath (Aii) to transform the GO into CNF, by moving the laser along the electrodes CNF is deposited over the entire length of the electrodes (Aiii), Aiv) shows an SEM images of the CNF on IDEs, Bi) shows the functionalization process through sputtering, Bii) shows the schematic of the functionalized CNF with Au particles.

and a structure of the functionalized material is presented in Figure 5.2Bii.

The deposited CNF shows a web-like appearance as seen in the SEM image in Figure 5.3a. A transmission electron microscopy (TEM) image, shown in Figure 5.3b, shows the dendritic strings which comprise the web-like structure seen at lower magnification.

Using a low magnification TEM image (Figure 5.4) a fractal dimension of 1.6 is measured, which shows that the strings are dominant in the formation of the overall network. The fractal dimension was calculated using ImageJ software and using the fractal analysis tool.

The TEM images acquired at low temperature in Figure 5.3c show that during the laser processing the GO is not completely transformed into CNF but individual flakes are transferred from the target to the substrate. The GO flakes are reduced into rGO during the transfer, and these rGO flakes are sparsely distributed through

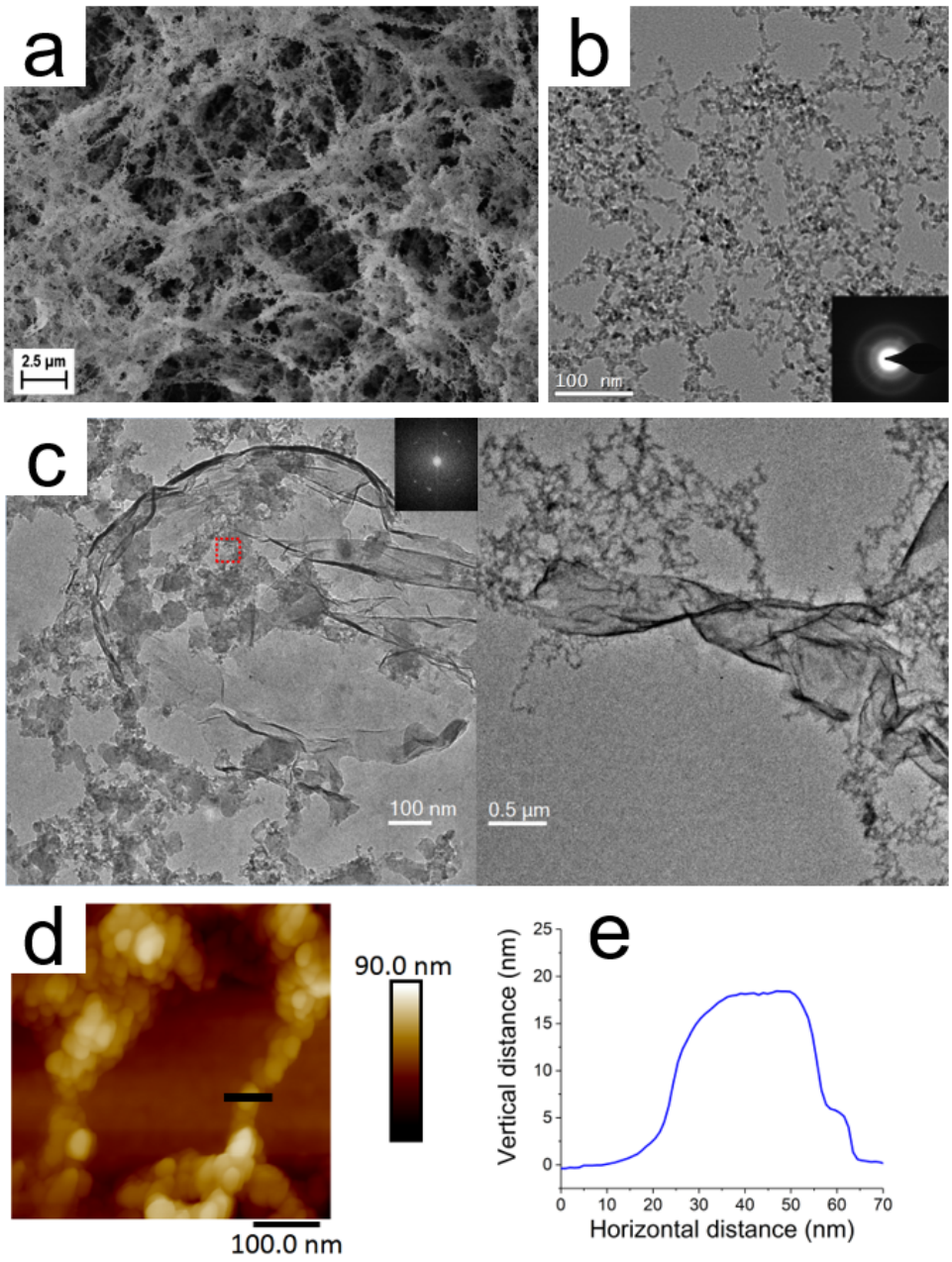

Figure 5.3: a) SEM image of uncoated CNF made from GO, b) TEM image of the CNF, a fractal analysis yields a fractal dimension of 1.6, the inset shows the transmission electron diffraction pattern showing the structure is amorphous, c) TEM images acquired at low temperatures of rGO flake transferred into the CNF, inset FFT shows crystalline structure of overlapping rGO flakes d) AFM picture of a string of the uncoated CNF structure, e) height analysis of insets in AFM image, the measured thickness is 18 nm.

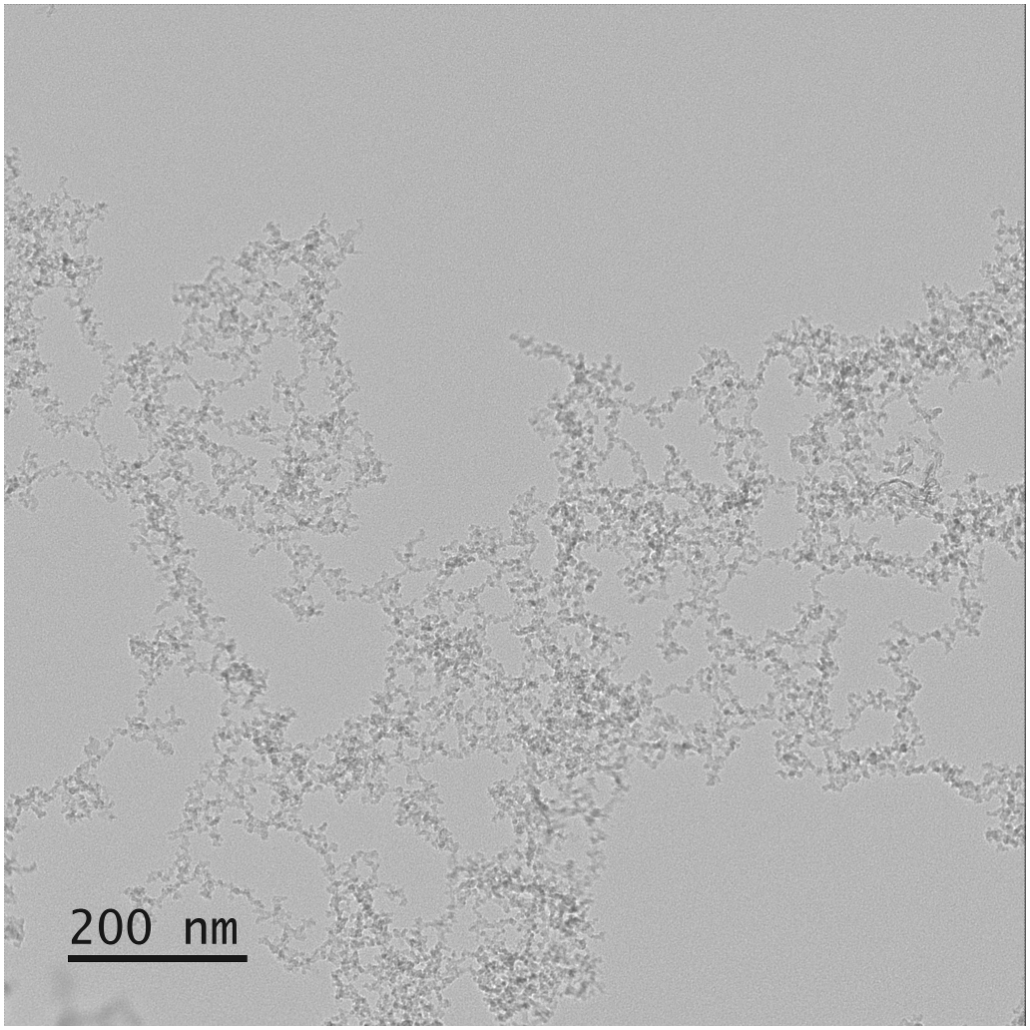

Figure 5.4: Low magnification TEM 2D projection image for fractal dimension analysis.

the CNF film. During laser ablation it is common for some parts of the material to redeposit on the laser target [236]. In the case of reducing graphene oxide not only does re-deposition occur but also a deoxygenation as locally high temperatures are induced, in a so-called laser shock hardening process [106, 111]. The oxygen release in the material induces a pressure build up which can lead to exfoliation of the material being illuminated [108, 237]. This leads us to believe the sheets of rGO in the CNF are a result of a combined process of re-deposition during the reduction of the graphene oxide and the laser induced exfoliation. The distribution of these rGO sheets is so sparse that they are not expected to greatly influence the conductivity of the CNF film.

The AFM micrograph of a foam sample in Figure 5.3d shows the cluster assembly of strings, as seen in the TEM. The dimensions are in the nanometre regime; approximately 18 nm for the region shown in Figure 5.3e. The broad, overlapping D and G modes in the Raman analysis (Figure 5.5) of the foam are indicative of amorphous carbon materials [238]. The dendritic growth seen in the TEM images, the cluster formation visible in the AFM image and the web-like structure over greater length scales in the SEM image is consistent with the explanations of CNF growth by Rode et al. [16, 229] and Henley et al. [228]

The structure and conductivity of the CNF can be modified by sputter coating with gold as shown in Figure 5.6a. While film thickness is poorly-defined for such porous structures, thickness measurements were performed with the focus drive of an optical microscope and an averaged value (film thickness of 100 μm) was used for conductivity calculations. The conductivity as a function of sputtering time is shown in Figure 5.6b.The initial conductivity of the unmodified CNF material was 3 $\mu\mathrm{S\,m^{-1}}$; upon coating with gold this increased to 58 $\mathrm{mS\,m^{-1}}$ after 7 min sputtering time. We can clearly see multiple regimes in the conductivity data of Figure 5.6b. Below 60 sec sputtering time the CNF conductivity does not significantly vary. SEM images of the deposited material at 15 sec (Figure 5.7a) and at 45 sec (Figure 5.7b) show that the CNF maintains its "fluffy" structure, albeit sparsely decorated with gold nanoparticles. Around 60 to 70 sec we observe that the conductivity begins to increase, with the data beyond that point resembling a power law dependence. This behaviour is characteristic of a percolating system, with the parameter space

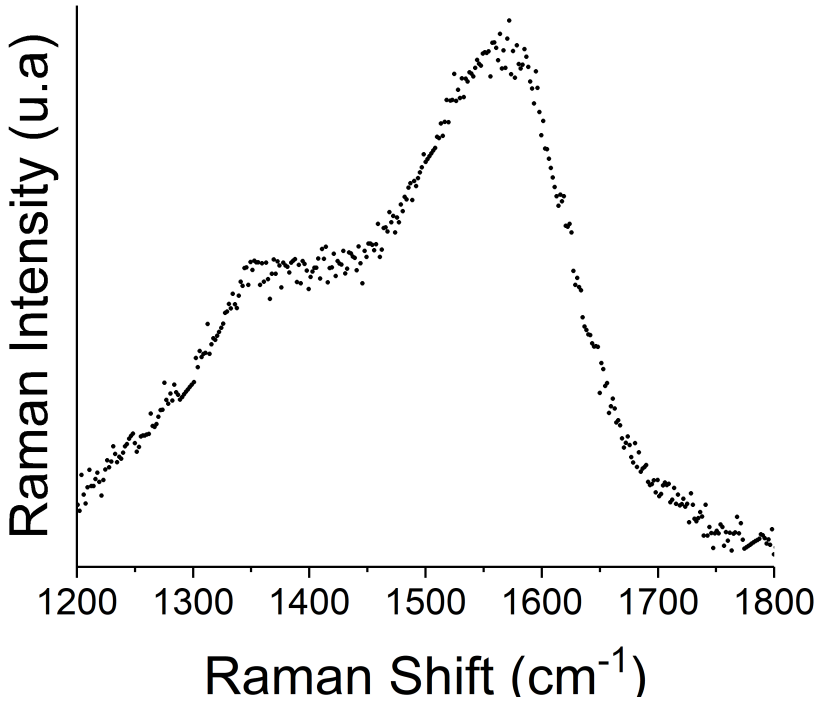

Figure 5.5: Raman analysis of carbon nanofoam.

(sputtering time) separated into below and above percolation regimes [239]. Figure 5.6c and 5.6d show the increase of gold coating on the CNF strings forming a metallic network. Once the density of gold on the CNF surpasses the percolation threshold the gold coating on the CNF begins to dominate the conductivity. The data of Figure 5.6b are fitted using a percolation scaling of the form

$$\sigma = A(t - t_c)^n + \sigma_0 \tag{5.1}$$

where σ is the conductivity; A is a pre-factor; t is the sputtering time; t_c is the percolation threshold; n is the conductivity exponent; σ_0 is the baseline CNF conductivity. We find the percolation threshold sputtering time to be 1 min, equivalent to a 3 nm thick gold layer on a flat surface. The increase in conductivity after the percolation threshold is smeared out due to the porous structure of the CNF. The power law curve would eventually saturate when all the pores are filled with gold.

The CNF inherently has a very high surface area that can be utilised in applications such as sensors or supercapacitors. Figure 5.8a shows the initial conductivity

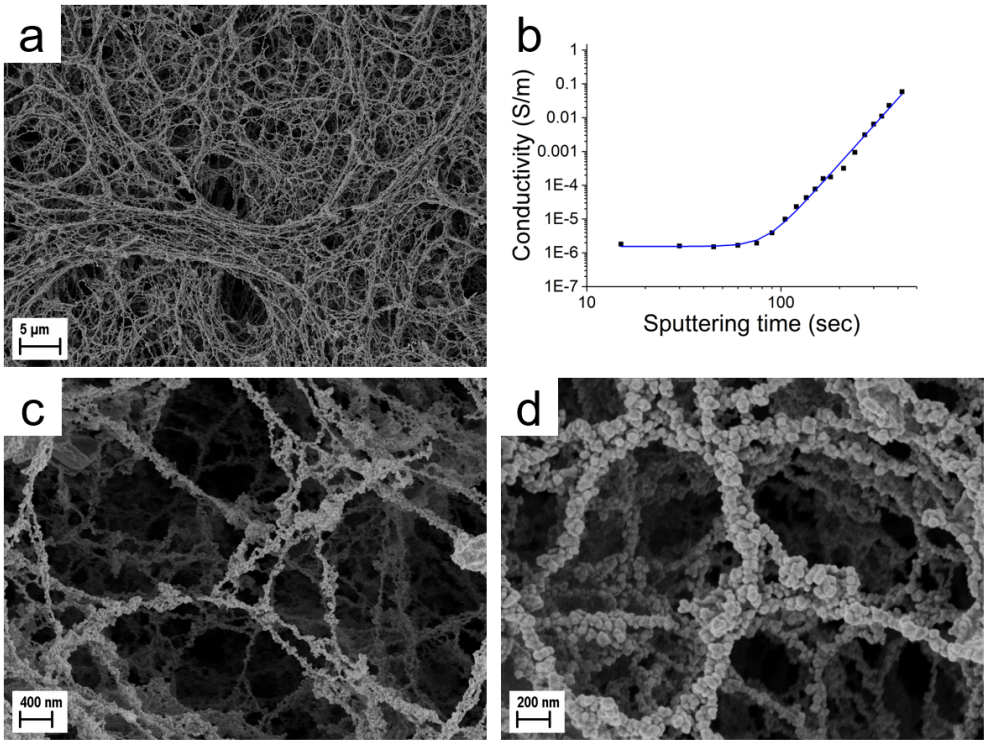

Figure 5.6: a) Low magnification SEM of a metal-coated CNF film. b) Conductivity values over different sputtering times with percolation fitting performed; SEM of CNF film after (c) 2 min , (d) 5 min of sputtering.

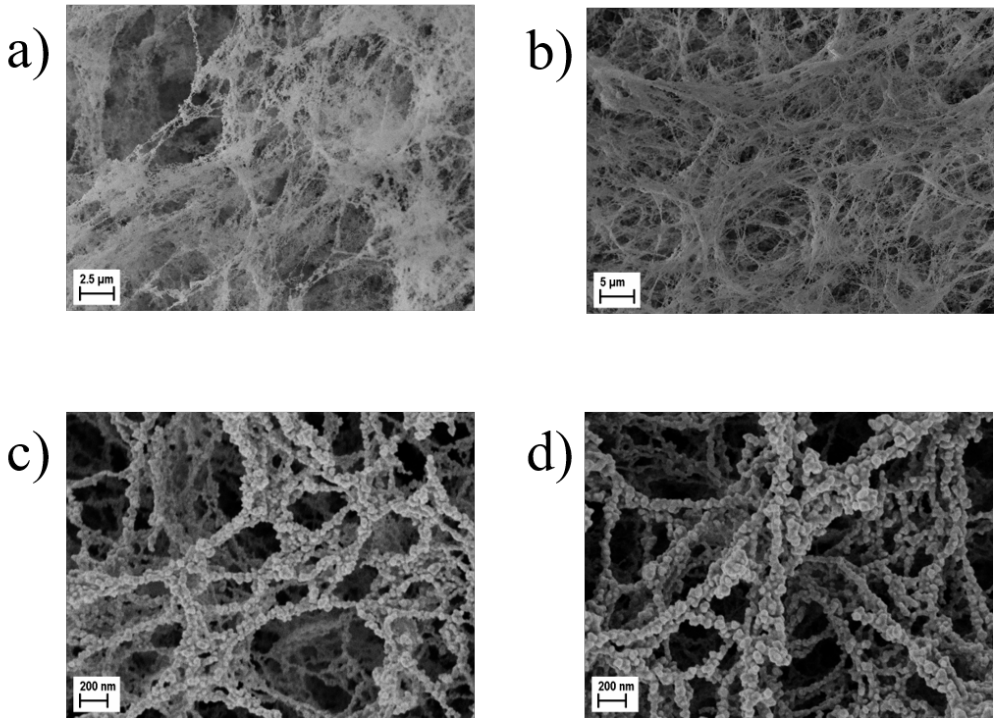

Figure 5.7: a) SEM of CNF sputtered with gold for 15 sec, b) 45 sec, c) 150 sec, d) 4 min.

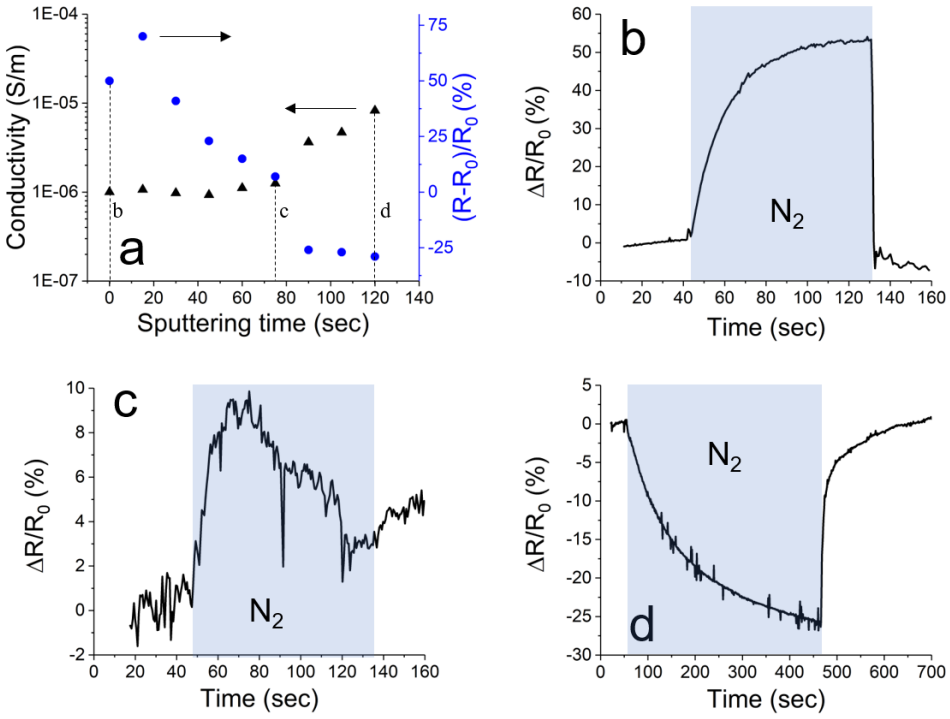

Figure 5.8: (a) Influence of sputtering time to response of sensor and conductivity to relative humidity change of 17 %, (b) Sensor response to a relative humidity change of 17 % of uncoated sample, (c) Sensor response a relative humidity change of 17 % when sputtered for 75 sec, (d) Sensor response a relative humidity change of 17 % when sputtered for 120 sec.

and response of the CNF to a change in humidity from 37 %rh to 20 %rh at different sputtering times. Figure 5.8b shows the time response of the uncoated pristine CNF. We note that below the percolation threshold the sample resistance increases with decreasing humidity, with a rapid recovery to the initial state once the initial humidity is restored. Treating the signal as a rising followed by a decaying exponential, we find time constants (t_{90}, the time required to achieve 90 % of the limiting response) of 13 sec for the water desorption and <1 sec for the subsequent water reabsorption. Above the percolation threshold the opposite effect is observed, with water desorption and adsorption occurring over significantly longer timescales; 32 sec and 65 sec for the desorption and recovery, respectively. Very close to the percolation threshold, the two apparently competing behaviours 'cancel out' to give an extremely low response to the humidity change. Figure 5.8c shows an analogous measurement to Figure 5.8b close to the gold percolation threshold, and Figure 5.8d shows the response within the percolating regime.

The above measurements show how the network changes its sensing behaviour from a carbon response to a metallic response. A decrease in humidity leads to a decrease in conductivity in the amorphous carbon network as the water layer on the carbon becomes discontinuous and slows down the H_2O-H_3O^+ transfer. This ionic transfer is the main water sensing mechanism in carbon-based systems [227]. By contrast, in the Au/CNF network where the conductivity is dominated by the gold, the adsorbed water induces depletion zones in the gold where it is attached. Removing water from the surface of the gold by reducing the humidity reduces the influence of the depletion zones so the conductivity increases [240].

A gold film sputtered directly onto electrodes (without the supporting CNF) with a similar resistance as the gold and carbon nanofoam hybrid (Au/CNF) of Figure 5.8d results in a response of only 7 % in the same experimental conditions. This effect can be attributed to the increased surface area available for the water to interact with the gold in the Au/CNF network and the increased influence of the depletion zones due to the nanometric size of the percolating gold particles.

The response of the sensors prepared to the humidity change in our experiments is high, with a maximum response of 70 % to a change of 18 %rh in the CNF sensor and a response of 30 % in the Au/CNF sensor. The response time of the CNF network is quicker than for the Au/CNF film but both have an excellent recovery time. While we expect that precisely at the percolation threshold the system itself should not be sensitive to a change in humidity, the competing effects of both the carbon response and the gold response can be seen in the device near percolation in Figure 5.8c. Lastly, we evaluate the sensitivity S of our devices, which is defined as

$$S = \frac{\frac{R-R_0}{R_0} \times 100}{\Delta\%rh} \tag{5.2}$$

where R is the measured resistance, R_0 is the baseline resistance, $\Delta\%rh$ is the change in humidity during the exposure [241]. For the CNF and Au/CNF hybrids respectively we find values of 3.89 and 1.70. For this limited range of measured humidity this sensitivity can compete with or exceed existing carbon-based humidity sensors based on a chemiresistor with DC bias [232, 233, 241, 242].

5.3 Conclusion

Carbon nanofoam has been formed as a by-product of the laser reduction of a GO precursor using an infrared pulsed laser. CNF appears only in a small window of fluences during the reduction process. Characterization of the CNF showed dendritic cluster assembly of carbon into fine structures with nanometre sized features. The CNF acts as nanostructured scaffold for sputtered gold. The metallization of the carbon structure results in a different surface doping mechanism compared to the pristine foam. Whereas the uncoated CNF is dominated by the transfer of electrons from the water ion transformation, the metallic structure is dominated by water induced depletion zones within the metal. These two mechanisms lead to opposing conductivity responses in the Au/CNF network. At percolation the two mechanisms counteract each other leading to a suppression of the sensitivity to a change in humidity. The tunability of the conductivity together with the high surface area may enable applications such as supercapacitors or gas sensors with diminished sensitivity to environmental water. The response of the CNF towards a change in humidity can compete with, or exceed, the performance of current sensors based on the same principle. This sensor design allows for increased selectivity by eliminating cross-talk due to humidity.

5.4 Experimental

Graphite oxide was prepared from graphite powder (Sigma Aldrich, Ref. 332461) using a modified Hummers' method as described elsewhere [243, 244]. In brief, 170 mL of concentrated H_2SO_4 was added to a mixture of graphite flakes (5.0 g) and $NaNO_3$ (3.75 g). The mixture was vigorously stirred for 30 minutes in an ice bath. $KMnO_4$ (25 mg) was slowly added while stirring for another 30 minutes. The reaction was then warmed up to 35 degree and stirred overnight. Subsequently, distilled water (250 ml) and 30 % H_20_2 (20 mL) were slowly added in sequence. The mixture was stirred for 1 hour, filtered and washed repeatedly with 400 mL of HCl:H_2O (1:10), and dried in air, thus yielding graphite oxide. Finally, the resulting graphite oxide was dispersed in water at a concentration of 2 $\mathrm{mg\,mL^{-1}}$ and bath sonicated for 2 hours. This led to a brown-colored dispersion of exfoliated graphene

oxide flakes.

The GO dispersion was spray deposited on to untreated soda-lime glass substrates using a hand-held air brush (Badger Model XL2000). The glass substrate was placed on a hotplate to enhance the evaporation rate of the water. Multiple spray passes were used to deposit a film with a thickness approximately 200 nm. The sample was then placed in an oven and the temperature was ramped to 250 degree over 1.5 hours and then taken out cool at room temperature.

An MSV-101 (M-Solv Ltd, Oxford) laser materials processing machine, equipped with a 1064 nm wavelength, nanosecond-pulsed laser (Multiwave MOPA-DY Series Pulsed Fiber Laser, set to 10 ns pulse duration and 200 kHz pulse repetition frequency) and galvoscanner was used for the GO reduction and consequent deposition of the CNF. For the CNF fluence window determination a frequency of 100 kHz and a mark speed of 30 $\mathrm{mm\,sec^{-1}}$ was used. For the deposition a glass substrate with molybdenum on top laser ablated into IDEs was placed 1 mm above the GO target. The laser beam was set up to pass through the (transparent) slide and its 25 μm focal spot was scanned over the GO partly reducing it to reduced GO and partly ablating it which results in the deposition of CNF on to the glass. The slide was kept stationary while the GO target was moved in by 7 μm, orthogonal to the laser scan direction, after each pass of the beam, to expose fresh GO target material. The laser fluence was set to 400 $\mathrm{mJ\,cm^{-2}}$ with a scan speed of 100 $\mathrm{mm\,s^{-1}}$.

Samples were imaged with a Zeiss SIGMA field emission gun scanning electron microscope using a Zeiss in-lens secondary electron detector. The FEG-SEM working conditions used were; 2.5 kV accelerating voltage, 20 μm aperture, and 2 mm working distance.

A Bruker Dimension Icon atomic force microscope was used in peak force mode to measure topography.

The Raman measurements were carried out with a Renishaw inVia confocal Raman microscope with a 532 nm solid-state laser and a $\times$50 objective lens (NA=0.75). GO and reduced GO were probed with 0.6 mW and the CNF with 0.06 mW laser intensity.

Gold was sputtered using a BIO-RAD SC 510 'cool' sputter coater. The current was held constant at 20 mA, the chamber vacuum was held at a constant pressure

of 0.1 mbar. The thickness was controlled by varying the sputtering time.

Humidity measurements were performed using pressurized nitrogen and a Alicat mass flow controller to maintain a flowrate of 500 sccm. The CNF was placed in a small measurement chamber (200 ml volume) contacted to measure its resistance using a Keithley 2420 source meter by applying a constant current and monitoring the voltage across the device. The baseline was measured at ambient with an open lid, the lid was closed and the chamber purged with nitrogen while the resistance was monitored. When the signal reached steady state the flow of nitrogen was interrupted and the lid opened to expose the device to ambient again. The humidity changed from 38 %rh at ambient to 20 %rh in the nitrogen environment. The CNF was deposited onto a on the substrate mounted holey carbon grid. The shape of the nanofoam was imaged using a transmission electron microscope FEI Titan operating at 300 keV. Both bright field TEM and annular dark field scanning TEM modes were used.

HRTEM images were taken at a FEI Titan High-Base microscope equipped with a CEOS CETCOR Cs objective lens corrector, working at 80 keV and a low temperature. Images were acquired using a Gatan 626 single-tilt liquid nitrogen cryo-holder, allowing for the sample to be kept at $\sim$77 K while performing this study.

Chapter 6

Carbon Nanofoam Supercapacitor Electrodes with Enhanced Performance using a Water Transfer Process

6.1 Introduction

Supercapacitors are electrochemical energy storage devices that have gained significant traction in recent years. They have much promise owing to fast charge times typically associated with dielectric capacitors (in the seconds), coupled with high energy densities normally associated with conventional electrochemical batteries. This is achieved through the formation of an electrical double layer at the interface between the high surface area electrodes and an interacting electrolyte.

Carbon nanomaterials, in particular, are well suited to supercapacitor applications [245, 246]. Many allotropes have high electrical conductivities, as well as high specific surface areas, making them ideal electrode materials. Moreover, their high porosity allows greater ion displacement from the electrolyte, greatly enhancing the electrical double-layer capacitance responsible for the overall performance of the device [247]. Multiple carbon nanomaterials have been investigated for use in supercapacitor electrodes; among them carbon nanotubes, pristine graphene, and reduced graphene oxide. These materials are highly structured, and require significant pro-

cessing in order to achieve porous structures that maximize the available electrode surface area. An alternative class of materials are carbon foams, which are volumetric, amorphous and highly porous [118, 248]. The morphologies vary depending on the synthesis method, but all varieties of carbon foam have a very high specific surface area up to 1500 $m^2\,g^{-1}$ [118]. In previous studies supercapacitor electrodes based on carbon foams have achieved up to 330 $F\,g^{-1}$ in aqueous electrolyte, which is highly competitive with other carbon nanomaterials (typical between 50 and 370 $F\,g^{-1}$) [182–184, 190, 245, 249].

Carbon nanofoams are a further sub-class of carbon foam formed during the interaction of laser radiation and a carbon-based target [16, 228–230]. The surface morphology of CNFs varies significantly compared to other carbon foams as it is formed in a diffusion limited aggregation manner rather than by increasing the volume of bulk pre-cursor [228]. The CNF consists of a significant amount of sp2 bonds making the material conductive [16, 229, 230]. Amongst the drawbacks of the CNF are poor mechanical stability and poor substrate adhesion. Although, both factors prevent the use of CNF electrodes in aqueous electrolytes, they are stable in many organic electrolyte systems. This has advantages as while aqueous electrolytes offer low cost and ease of processing, organics allow for a wider potential window and consequently a higher energy density [188].

During the preparation of CNFs, the substrate adhesion is low enough that contact with water is able to delaminate the materials. Interestingly, this phenomenon can be used as a route to transfer the electrode material from an initial substrate to a target by a water transfer process. In this way, the CNF floats on top of the water sub-phase and can subsequently be picked up by withdrawing a submerged substrate from below. While the material is trapped at the air-water interface morphological changes can occur due to capillary forces. This effect is particularly apparent in materials with a small characteristic pore size, due to enhancement of the capillary interaction [250].

In this paper we demonstrate the preparation and characterization of a CNF-based supercapacitor electrode material through laser processing of a graphene oxide target. The prepared CNF is transferred onto an appropriate substrate by use of a water transfer process resulting in a change in the morphology of the foam, which

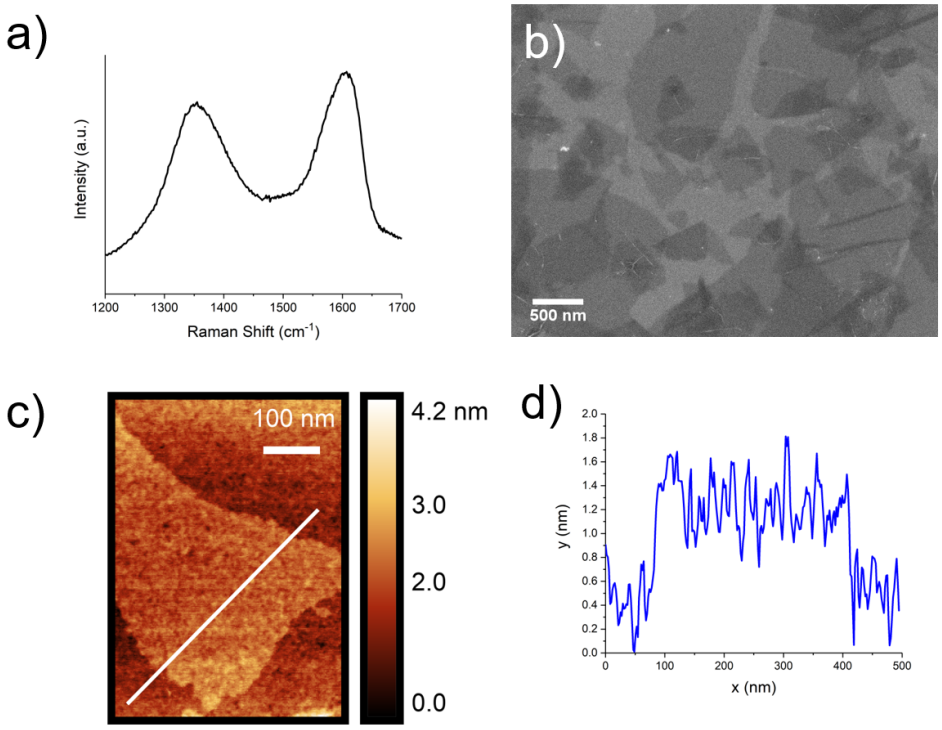

Figure 6.1: Characterisation of prepared GO, a) Raman peaks, b) SEM image to determine flake size, c) AFM topography, d) thickness measurement of prepared flake.

enhances the specific capacitance of the resulting electrodes by a factor of two. Using Raman spectroscopy we relate the electrochemical performance enhancement to compression from the capillary forces during the film transfer.

6.2 Results & Discussion

Figure 6.1 shows the GO characterization used as pre-cursor for the CNF. Raman shows a well-defined D and G peak of the prepared graphene oxide. Flake size of the synthesized GO was between 500 nm and several μm. Flake thickness is 0.8 nm.

Schematics of two fabrication processes to produce CNF on tin-doped indium oxide substrates are shown in Figure 6.2. Figure 6.2a illustrates the direct deposition approach, where the laser is scanned through an ITO-coated substrate above the GO target. The very first line ablates a small track into the ITO through which the laser passes afterwards to hit the target. The laser focus is kept on the substrate. The carbon clusters diffuse out of the laser-formed plasma on the target during the

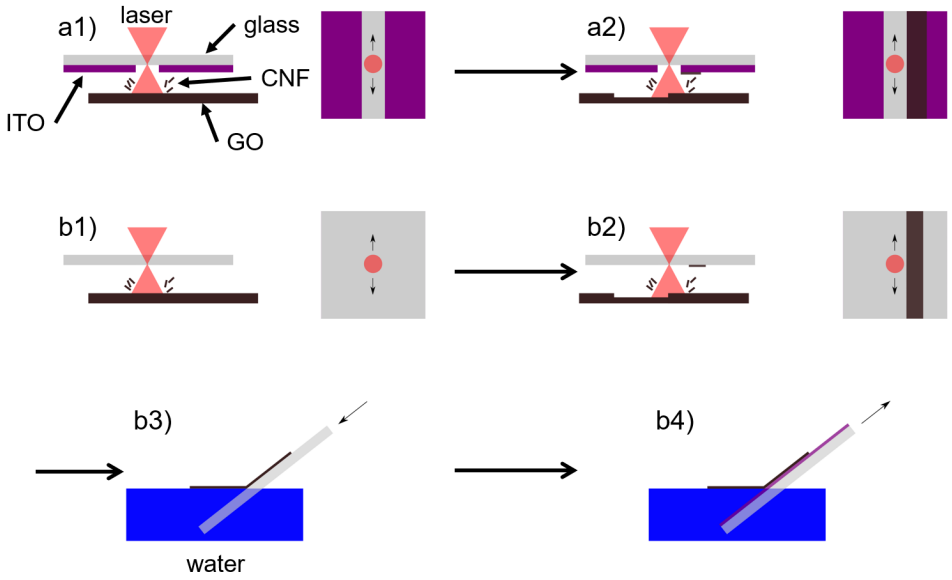

Figure 6.2: Fabrication schematic of CNF samples. a1) ITO on glass is held above the GO target, through which the laser is scanned (using a pre-patterned slit in the ITO layer). a2) A thick layer of CNF is deposited on the ITO by moving the GO target to feed the deposition process. b1) and b2) show the same deposition process except a glass substrate is used. b3) The glass substrate is immersed into water to detach the CNF. b4) The CNF is transferred to the final ITO substrate through a reverse process to b3).

reduction of the GO and deposit on the substrate above. Multiple passes form a thick layer of CNF. Since this process involves the formation of a carbon plasma we are able to prepare CNF with any high-carbon content material, the feedstock is not limited to GO.

The water transfer deposition approach is shown in Figure 6.2b. The glass substrate is immersed into a water bath whereby the CNF detaches and floats on the water surface as it is less dense than water. The cohesion of the foam is strong enough so it does not break apart when immersed. The CNF is then picked up by hand using an ITO substrate, immersed in the water and withdrawn at a shallow angle to the water surface. The speed and the angle of the pick-up are critical in order not to rip apart the CNF floating on the water. Done at a slow velocity and shallow angle does not change the properties of the foam when picked up. The film is up to 5 mm wide and typcially 2 cm long. Picked-up correctly leaves a uniform film without gaps. The thickness of the deposited film changes in the corss-section due to the nature of the laser deposition process.

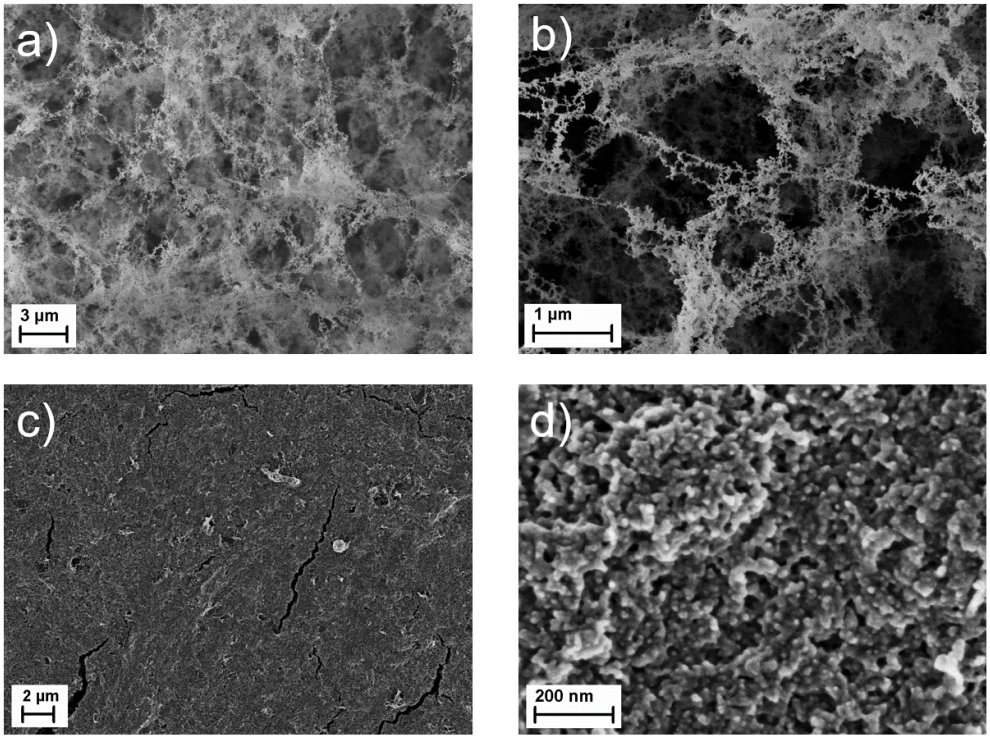

Figure 6.3: SEM images of a) CNF directly deposited on ITO, b) Magnified image of CNF directly deposited on ITO, c) CNF on ITO after the water transfer process of Figure 6.2b, d) high magnification image of water transferred CNF.

Imaging by scanning electron microscopy (Figure 6.3) shows a significant difference in morphology between the two deposition methods. The direct-deposited CNF in Figure 6.3a has a low-density, high porosity structure with a web-like microstructure. This morphology is typical for a diffusion-limited aggregation formation process [225]. The magnified image in Figure 6.3b reveals the porous microstructure formed by the clusters which are then spun into a 'web' like appearance. The volumetric character of the CNF did not allow further magnification without charging effects.

The water transferred sample (Figure 6.3c) appears to be much denser, where the very fine microstructure of the as-formed CNF has seemingly collapsed. The water transfer increaes the CNF's conductivity by more than three orders of magnitude to 740 μS/m from 360 μS/m.

Sets of electrodes prepared by the two methods described in Figure 6.2 were used to perform electrochemical measurements. Figure 6.4 a shows CV analysis of CNF prepared by direct deposition onto ITO, as well as for water transferred films. In both cases the scan rate was 50 mV/s. All samples exhibit a near-ideal

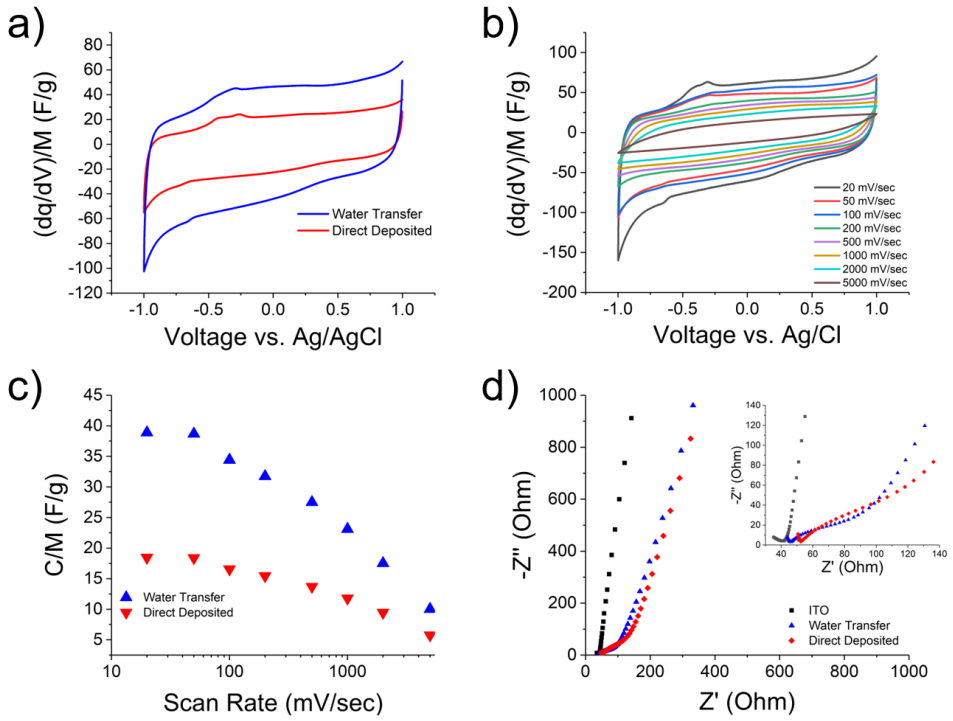

Figure 6.4: a) CV scans of the two different CNF electrode materials at 50 $\mathrm{mV\,s^{-1}}$ *scan rate. b) Scan rate dependence of the water transferred electrode material. c) Specific capacitance of the two samples as a function of scan rate. d) Nyquist plot of spectroscopic impedance measurements of the electrode materials, showing the blank ITO substrate as a reference, inset shows the low impedance region.*

box-like CV character. The two visible peaks around -0.3 V originate from the ITO substrate. Figure 6.4b shows the scan rate dependence of a water transferred sample. It is evident that the capacitance falls with increased scan rate, however it remains constant up to 100 mV/sec scan rate. The box-like shape is maintained at all the scan rates.

Figure 6.4c illustrates the scan rate-dependence of the specific capacitance for the samples shown in Figure 6.4a. The direct deposited CNF shows the lower specific capacitance at around 17.5 $\mathrm{F\,g^{-1}}$, while the water transferred electrode gives a value of 42 $\mathrm{F\,g^{-1}}$. We see immediately that the specific capacitance of the water transferred CNF is more than double the value of the direct-deposited material. The impedance plot in Figure 6.4d shows the characteristic steep slope for all of the electrodes at lower frequencies. The ITO substrate is plotted as a reference showing the active material behaving as a supercapacitor.

The cyclic voltammetry measurements of Figure 6.4a and 6.4b show rectangular

behavior for the different samples, suggesting an ideal propagation of charges within the electrodes [251].

The rectangular shape of Figure 6.4b is maintained up to 100 $mV\,s^{-1}$ scan rate with little variation of the capacitance. The specific capacitance decreases at higher scan rates, because ion mobility and the substrate's resistance limits charge separation in the electrolyte [252]. The carbon maintains the rectangular shape at high scan rates showing good capacitive behavior. The specific capacitance of the direct deposited values measured for the materials presented are comparable with work done on CNF systems created in a pulsed laser deposition process [188].

The results of spectroscopic impedance measurements plotted in Figure 6.4d highlight the quality of the CNF supercapacitor electrodes prepared here. The steeper the angle at low frequencies, indicating non-diffusion-limited accumulation of electrode surface charge, the closer the system behavior to that of an ideal supercapacitor [253]. The region exhibiting a 45 degree angle to the axes is characteristic of Warburg behavior (see inset in Figure 6.4d), which represents the frequency range where ion diffusion within the electrodes limits the capacitance achievable. A greater Warburg region indicates that the electrode structure is inhibiting the diffusion of electrolyte ions [251]. The Warburg region in these devices is smaller for the water transferred samples than the direct deposited ones, showing the pores are easily accessible for diffusing ions. The intersection with the x-axis presents the solution and electrode resistance. The differences lie in the fact that the substrate width was slightly different in all the measurements. The sample with a smaller width showed a higher intersection value.

The increase of specific capacitance between direct-deposited CNF and the water transferred CNF is due to the change in morphology, which we believe is induced by capillary forces during the film transfer [250]. The water transfer creates a different porous structure for ion interaction which results in an increased system capacitance [254, 255]. Porosity is a key parameter in supercapacitor structures as the electric double layer is influenced by the distribution between macro- (>50 nm), meso- (2 - 50 nm) and micropores (0.7 - 2 nm). Macro- and mesopores enable good diffusion of ions into the micropores where the surface area is greatly enhanced to accommodate the ions, whereas solvent molecules penetrate only as far as the mesopores [254]. Beside

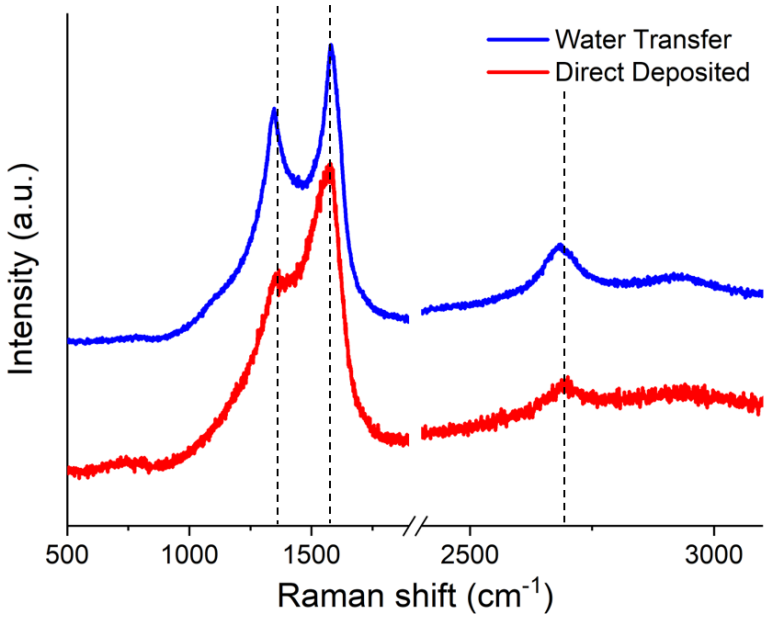

Figure 6.5: Raman spectrum of direct deposited and water transferred CNF on to glass.

the porosity the film becomes denser, therefore increasing the electrical contact between the carbon clusters increasing the conductivity which increases the specific capacitance.

To investigate the influence of the water transfer on the CNF microstructure further we turn to Raman spectroscopy. This technique is able to highlight differences in the bonding character as well as doping or strain in carbon nanomaterials [50, 218, 256–258]. Raman spectra of CNF directly deposited on a glass substrate and a CNF sample water transferred from a glass substrate on to a glass substrate are shown in Figure 6.5. The spectra are stacked and normalized to the G-peak intensity.

We note several changes to the Raman spectra of the water transferred material, when compared to the direct-deposited CNF. All three peaks show a red shift of three wavenumbers after the water transfer. In carbon materials this shift to lower wavenumbers is associated with a mechanical deformation in the material [256, 259–261]. The I(D)/I(G) ratio increases after the water transfer. This is an indication that the disorder in the carbon increases [262]. The shift of the D'-peak is another

indication that the disorder in the material is increasing [263]. The peak showing up around 1100 cm^{-1} origins in the underlying borosilicate glass substrate.

The increase of specific capacitance is not only from the change in morphology but the capillary forces also introduce stress into the material. During the water transfer the water enters the porous CNF and capillary forces start compressing the film. This not only changes the surface structure but induces a compressive stress into the carbon. It is known that compressive forces can enhance the specific capacitance of carbon films, as the surface wettability increases when pressure is applied [264]. The enhanced specific capacitance therefore originates from two different components, namely a change in morphology making a more dense film, making the pores more accessible and a compressive stress induced by the capillary forces which increases the capacitance further.

6.3 Conclusion

We have demonstrated the preparation and characterization of a carbon nanofoam-based supercapacitor electrode material. The material is prepared through infrared laser treatment of a graphene oxide target, and may be directly deposited onto a current collector layer (in this case ITO), or may be transferred from a glass substrate using a water transfer process. We observe significant changes to the morphology of the CNF when transferred in this fashion, including development of compressive stress (as characterized using Raman spectroscopy). This effect arises due to the influence of capillary forces during the transfer process. The outcome is a significant increase in the specific capacitance of the CNF, from 17.5 $F\,g^{-1}$ to around 42 $F\,g^{-1}$.

6.4 Methods

Graphene oxide was prepared using the Hummers method [243, 244]. The GO was characterized using atomic force microscopy to determine flake thickness, SEM to characterized flake size and Raman spectroscopy. For characterization the GO was spin coated onto a silicon substrate.

The GO was deposited by drop casting onto a borosilicate glass slide. The glass slide was completely covered and left to dry at 50 °C to hasten the drying process. A

second drop casting step was added to create a thick layer of GO on the glass slide, it was again left to dry at 50 °C. The film thickness was aimed to be bigger than 200 μm. The exact experimental setup to create the CNF is described elsewhere [225]. A brief summary: the targets were irradiated with a Multiwave Nd:YAG nanosecond pulsed infrared laser (set at 10 ns) in ambient conditions with a set fluence of 417 $\mathrm{mJ\,cm^{-2}}$. To form the CNF on the substrate, it was held stationary over the target with a small ($<$ 1 mm) air-gap in between allowing the aggregation of the carbon clusters on the substrate.

The weight of the CNF was measured using a Mettler Toledo micro-balance. Six lines were deposited on to the same substrate in order to get weight well outside of the error of the balance. The substrates were measured before and after the deposition. The measured weight was then divided by the number of lines deposited. Samples were imaged with a Zeiss SIGMA field emission gun scanning electron microscope using a Zeiss in-lens secondary electron detector. The FEG-SEM working conditions used were; 1 kV accelerating voltage, 20 μm aperture, and 2 mm working distance.

Electrochemical measurements were made with a 3 electrode configuration using a Gamry 600+ reference potentiostat. The counter electrode was a platinum wire and the reference electrode was silver/silver chloride (Ag/AgCl). The electrolyte used was 0.1 M Lithium Perchlorate ($LiClO_4$) in Acetonitrile (ACN). Cyclic Voltammetry measurements were taken in a range of -1 to +1 V vs. Ag/AgCl for a variety of scan rates from 20 mV/s to 5000 $\mathrm{mV\,s^{-1}}$. Impedance Spectroscopy applied a perturbation signal of 10 mV around 0 V at frequencies from 100 kHz to 0.1 Hz. Raman measurements were carried out using a Renishaw Invia Microscope. A 532 nm 50 mW continuous wave laser was used at 10 % intensity for 10 seconds to produce the Raman spectrum. Ten accumulations were used to enhance the signal.

A Bruker Dimension Icon atomic force microscope was used in peak force mode to measure thickness of the GO flakes.

Chapter 7

Conclusion

In summary, device architectures based on a bottom-up approach are presented. The fabrication process is based on laser ablated IDEs. Using the L-S method a percolating film of commercially available graphene flakes is deposited on the electrodes. Exposure to ammonia in a proof of concept setup results in a detection limit of 1 ppm. A response time of 90 seconds was measured. This performance can compete with commercially available gas sensors.

Further, the sensing mechanism in these percolating networks was studied. Using KPFM, the work function change due to doping of the basal plane was measured. Ammonia donates electrons when adsorbed on the graphene. The p-type nature of graphene results in a resistance increase when exposed to NH_3. Acetone works as an electron acceptor depleting graphene of minority carriers. The exposure to acetone therefore has the opposite effect to exposure to ammonia, as demonstrated by the KPFM measurements. Nevertheless the resistance of the percolating film is increasing when exposed to acetone. This leads to the conclusion that the signal originates from the edges of the graphene flakes. This suggests that the dominant resistive effect is the contact resistance between the percolating films. Knowing the adsorption measured is at the edges of the flakes allows one to determine the adsorption energies of the gaseous molecules. By fitting the desorption curves at different temperatures, one can extrapolate the adsorption energy. The measured values coincide with DFT calculations on similar systems. CNF can be deposited on a substrate with a simple direct deposition method. On one hand, its properties can be changed using sputtering as a functionalization technique. The percolating be-

haviour of the functionalization leads to different responses to a change in humidity. Below the percolation threshold the CNF behaves as carbon structure. Electrical conductivity is influenced by the Grotthuus-chain reaction increasing the resistance at lower humidity levels. Above the percolation threshold the CNF acts as scaffold for the Au. The resistance decreases when exposed to a dryer environment. The thin water layer induces a depletion zone into the metal. Removing part of the water decreases the size of the depletion zone decreasing the resistance of the metallic film.

On the other hand the properties of the CNF can be changed when the film is going through a water transfer process. Capillary forces change the morphology of the CNF. SEM and CV measurements show different pore architectures due to the water transfer. Raman reveals that besides a change in pore structure, a compressive stress is present due to the capillary forces. The enhanced gravimetric capacitance originates from a combination of a change in the pore architecture, compressive stress and an enhanced electrical conductivity induced by capillary forces.

These results show the incorporation of commercially available graphene flakes into a bottom-up device structure. The entire fabrication process is based on scalable methods. The combination of laser ablation and L-S deposition is a simple two-step process to create the device. More research is needed to overcome the issues of drift and selectivity.

The determination of the sensing mechanism reveals the scalability of the device. Because the sensing takes place at the edges of the graphene flakes, no high quality material is necessary. Gases can adsorb at the defects of the graphene but they will not contribute to the electrical signal as the edges are dominant. Batch fabricated graphene is ready available and will drop in price. Therefore this method using laser ablation and L-S deposition is a highly scalable approach to incorporating nanomaterials in gas sensor architectures.

Moreover laser setups are highly adaptable. The laser deposition process presented shows the formation of carbon nanomaterials directly onto a pre-patterned substrate. This deposition does not alter the properties of the foam as the deposition is the last step. Pre-studies for gas sensing devices and supercapacitor applications show the deposition technique produces functional carbon nanofoam. These applica-

tions need more research in order to boost their performance but also to understand their behaviour.

The overall aims of this thesis have been reached. A scalable fabrication method for nanomaterials has been demonstrated and the performance of devices utilising these nanomaterials has been measured. A scalable one step deposition technique for carbon nanofoam has been established. These first proof of concept devices have shown promising results and need more research and development to increase their technology readiness level.

Chapter 8

Outlook

It is possible to speculate about future work based on the work done in this thesis. We can distinguish between two different systems of the thesis, namely the Langmuir deposited graphene gas sensor and the CNF gas sensor.

8.1 Future work on Langmuir gas sensor

In order to fully understand the sensing mechanism and to find the best performance further work is required.

More measurements with the current system need to be done in a measurement setup where the environmental conditions are better controlled. This is necessary to measure the device performance in a setup where only gaseous components are present. This allows the removal of the influence of water from the device, such that the adsorption calculations will be more accurate.

Currently only the desorption energy of ammonia has been calculated. There are a lot of different gases available to do measurements with. This would provide further experimental evidence to verify the simulated values of the edge adsorption energies on the graphene flakes.

Fitting of the adsorption and desorption gives a time constant which provides an indication of the process length. Using various cases and analysing the time constants in the adsorption and the desorption curve might lead to interesting results which could be used to improve the selectivity of the devices. These variables could be used, for example, in an algorithmic analysis like principle component analysis.

Additional work is required to fully understand the sensing mechanism. Currently it is not entirely clear if the change in contact resistance is coming from a charge transfer at the edges of the graphene platelets or if the adsorbed molecules place themselves between the flakes and change the contact resistance. Here, novel experimental setups are needed in combination with simulations in order to fully understand the adsorption process in percolating films.

Some more engineering work is also required to see if the system performance can be improved. Controlling the size of the graphene flakes used would enable an investigation into the impact of flake size on device performance. This could also lead to the identification of an optimum flake size. Changing the size of the flakes will change the total contact area which should lead to more adsorption sites with smaller flake size. Small flakes would also have more contact points, potentially leading to an increase in noise level. An optimum should be found where the devices show their best performance. In addition to the flake size, it would also be interesting to investigate the response as a function of the number of layers. Functionalization of the material is another way to improve the performance of the devices. Counter intuitively, measurements with functionalised materials in a L-S deposited film show a conductivity decrease rather than an increase [201].

Further to the above, precise characterization is necessary to determine if functionalisation can overcome the inter-sheet resistance in percolating films. In addition to the investigation of the material geometry, a composite layer comprised of different 2D layers might also show interesting properties. A clear characterisation of where the adsorption takes place and a fitting of the data might be difficult as it is hard to determine which materials are dominant.

8.2 Carbon Nanofoam

First principle studies have been done with CNF in gas sensor structures. A more specific characterisation of the carbon nanofoam as a gas sensor will be interesting work. From literature, it is known that the CNF has a similar chemical structure to activated carbon, which is used in filters for nitrogen dioxide [265, 266]. A response of the CNF towards NO_2 is predicted at low concentrations as the material is highly

porous in a volumetric structure allowing the highest possible surface availability for molecules. The chemical structure of the CNF should make it a quite selective material as there are not many defects that gases can adsorb to. A highly reactive molecule is necessary to trigger a response. In order to characterise the CNF as a gas sensor structure, a more sophisticated gas measurement setup is necessary allowing low concentrations of targeted gases in a small volume to make sure various environmental influences do not play a role during the characterisation.

Chapter 9

Bibliography

Bibliography

[1] L. Wilson, "International technology roadmap for semiconductors (itrs)," *Semiconductor Industry Association*, 2013.

[2] R. W. Keyes, "Physical limits of silicon transistors and circuits," *Reports on Progress in Physics*, vol. 68, no. 12, p. 2701, 2005.

[3] E.-E. Commission *et al.*, "Commission recommendation of 18 October 2011 on the definition of nanomaterial," *Official J Eur Union*, vol. 50, pp. 38–40, 2011.

[4] F. R. Baptista, S. Belhout, S. Giordani, and S. Quinn, "Recent developments in carbon nanomaterial sensors," *Chemical Society Reviews*, 2015.

[5] S. Iijima and T. Ichihashi, "Single-shell carbon nanotubes of 1-nm diameter," *Nature*, vol. 363, no. 6430, p. 603, 1993.

[6] K. S. Novoselov, A. K. Geim, S. V. Morozov, D. Jiang, Y. Zhang, S. V. Dubonos, I. V. Grigorieva, and A. A. Firsov, "Electric field effect in atomically thin carbon films," *Science*, vol. 306, no. 5696, pp. 666–669, 2004.

[7] C. Lee, X. Wei, J. W. Kysar, and J. Hone, "Measurement of the elastic properties and intrinsic strength of monolayer graphene," *Science*, vol. 321, no. 5887, pp. 385–388, 2008.

[8] K. I. Bolotin, K. Sikes, Z. Jiang, M. Klima, G. Fudenberg, J. Hone, P. Kim, and H. Stormer, "Ultrahigh electron mobility in suspended graphene," *Solid State Communications*, vol. 146, no. 9-10, pp. 351–355, 2008.

[9] O. Faruk and M. Sain, *Lignin in Polymer Composites*. William Andrew, 2015.

[10] R. Pekala, J. Farmer, C. Alviso, T. Tran, S. Mayer, J. Miller, and B. Dunn, "Carbon aerogels for electrochemical applications," *Journal of Non-Crystalline Solids*, vol. 225, pp. 74–80, 1998.

[11] J. Biener, M. Stadermann, M. Suss, M. A. Worsley, M. M. Biener, K. A. Rose, and T. F. Baumann, "Advanced carbon aerogels for energy applications," *Energy & Environmental Science*, vol. 4, no. 3, pp. 656–667, 2011.

[12] M. Glora, M. Wiener, R. Petričević, H. Pröbstle, and J. Fricke, "Integration of carbon aerogels in PEM fuel cells," *Journal of Non-Crystalline Solids*, vol. 285, no. 1-3, pp. 283–287, 2001.

[13] S.-W. Hwang and S.-H. Hyun, "Capacitance control of carbon aerogel electrodes," *Journal of Non-Crystalline Solids*, vol. 347, no. 1-3, pp. 238–245, 2004.

[14] J. Feng, J. Feng, Y. Jiang, and C. Zhang, "Ultralow density carbon aerogels with low thermal conductivity up to 2000 C," *Materials Letters*, vol. 65, no. 23-24, pp. 3454–3456, 2011.

[15] S.-A. Wohlgemuth, R. J. White, M.-G. Willinger, M.-M. Titirici, and M. Antonietti, "A one-pot hydrothermal synthesis of sulfur and nitrogen doped carbon aerogels with enhanced electrocatalytic activity in the oxygen reduction reaction," *Green Chemistry*, vol. 14, no. 5, pp. 1515–1523, 2012.

[16] A. V. Rode, S. Hyde, E. Gamaly, R. Elliman, D. McKenzie, and S. Bulcock, "Structural analysis of a carbon foam formed by high pulse-rate laser ablation," *Applied Physics A: Materials Science & Processing*, vol. 69, no. 7, pp. S755–S758, 1999.

[17] V. N. Mochalin, O. Shenderova, D. Ho, and Y. Gogotsi, "The properties and applications of nanodiamonds," *Nature Nanotechnology*, vol. 7, no. 1, p. 11, 2012.

[18] O. A. Williams, *Nanodiamond*. Royal Society of Chemistry, 2014.

[19] J.-B. Donnet, *Carbon black: Science and technology*. CRC Press, 1993.

[20] X.-M. Meng, X.-J. Zhang, C. Lu, Y.-F. Pan, and G.-S. Wang, "Enhanced absorbing properties of three-phase composites based on a thermoplastic-ceramic matrix ($BaTiO_3$+ PVDF) and carbon black nanoparticles," *Journal of Materials Chemistry A*, vol. 2, no. 44, pp. 18725–18730, 2014.

[21] E. Hu, X. Hu, T. Liu, R. Song, K. D. Dearn, and H. Xu, "Effect of TiF_3 catalyst on the tribological properties of carbon black-contaminated engine oils," *Wear*, vol. 305, no. 1-2, pp. 166–176, 2013.

[22] K. D. Esmeryan, C. E. Castano, and R. Mohammadi, "Interactions of superhydrophobic carbon soot coatings with short alkyl chain alcohols and fluorocarbon solutions," *Colloids and Surfaces A: Physicochemical and Engineering Aspects*, vol. 529, pp. 715–724, 2017.

[23] J.-O. Müller, D. S. Su, U. Wild, and R. Schlögl, "Bulk and surface structural investigations of diesel engine soot and carbon black.," *Physical Chemistry Chemical Physics : PCCP*, vol. 9, pp. 4018–25, Aug 2007.

[24] H. Marsh and F. R. Reinoso, *Activated Carbon*. Elsevier, 2006.

[25] I. Tan, B. Hameed, and A. Ahmad, "Equilibrium and kinetic studies on basic dye adsorption by oil palm fibre activated carbon," *Chemical Engineering Journal*, vol. 127, no. 1-3, pp. 111–119, 2007.

[26] Z. Zhao, S. Hao, P. Hao, Y. Sang, A. Manivannan, N. Wu, and H. Liu, "Lignosulphonate-cellulose derived porous activated carbon for supercapacitor electrode," *Journal of Materials Chemistry A*, vol. 3, no. 29, pp. 15049–15056, 2015.

[27] K. F. Mak, C. Lee, J. Hone, J. Shan, and T. F. Heinz, "Atomically thin MoS_2: a new direct-gap semiconductor," *Physical Review Letters*, vol. 105, no. 13, p. 136805, 2010.

[28] Y. Lin and J. W. Connell, "Advances in 2D boron nitride nanostructures: nanosheets, nanoribbons, nanomeshes, and hybrids with graphene," *Nanoscale*, vol. 4, no. 22, pp. 6908–6939, 2012.

[29] L. Li, Y. Yu, G. J. Ye, Q. Ge, X. Ou, H. Wu, D. Feng, X. H. Chen, and Y. Zhang, "Black phosphorus field-effect transistors.," *Nature Nanotechnology*, vol. 9, pp. 372–7, May 2014.

[30] P. Vogt, P. De Padova, C. Quaresima, J. Avila, E. Frantzeskakis, M. C. Asensio, A. Resta, B. Ealet, and G. Le Lay, "Silicene: compelling experimental evidence for graphenelike two-dimensional silicon," *Physical Review Letters*, vol. 108, no. 15, p. 155501, 2012.

[31] L. Shi and T. Zhao, "Recent advances in inorganic 2d materials and their applications in lithium and sodium batteries," *Journal of Materials Chemistry A*, vol. 5, no. 8, pp. 3735–3758, 2017.

[32] A. Zöpfl, M.-M. Lemberger, M. König, G. Ruhl, F.-M. Matysik, and T. Hirsch, "Reduced graphene oxide and graphene composite materials for improved gas sensing at low temperature," *Faraday Discussions*, vol. 173, pp. 403–414, 2014.

[33] F. Schedin, A. K. Geim, S. V. Morozov, E. W. Hill, P. Blake, M. I. Katsnelson, and K. S. Novoselov, "Detection of individual gas molecules adsorbed on graphene," *Nature Materials*, vol. 6, pp. 652–5, Sep 2007.

[34] K. Chikkadi, M. Muoth, V. Maiwald, C. Roman, and C. Hierold, "Ultra-low power operation of self-heated, suspended carbon nanotube gas sensors," *Applied Physics Letters*, vol. 103, no. 22, p. 223109, 2013.

[35] H. D. Vora and N. B. Dahotre, "Lasers in manufacturing and materials processing,"

[36] M. Shirk and P. Molian, "A review of ultrashort pulsed laser ablation of materials," *Journal of Laser Applications*, vol. 10, no. 1, pp. 18–28, 1998.

[37] E. Gamaly, A. Rode, B. Luther-Davies, and V. Tikhonchuk, "Ablation of solids by femtosecond lasers: Ablation mechanism and ablation thresholds for metals and dielectrics," *Physics of Plasmas (1994-present)*, vol. 9, no. 3, pp. 949–957, 2002.

[38] M. S. Brown and C. B. Arnold, "Fundamentals of laser-material interaction and application to multiscale surface modification," in *Laser Precision Microfabrication*, pp. 91–120, Springer, 2010.

[39] T. Lippert, "Interaction of photons with polymers: From surface modification to ablation," *Plasma Processes and Polymers*, vol. 2, no. 7, pp. 525–546, 2005.

[40] D. Bäuerle, "Nanosecond-laser ablation," in *Laser Processing and Chemistry*, pp. 237–278, Springer, 2011.

[41] P. Schaaf, *Laser processing of materials: fundamentals, applications and developments*, vol. 139. Springer Science & Business Media, 2010.

[42] I. Langmuir and V. J. Schaefer, "Activities of urease and pepsin monolayers," *Journal of the American Chemical Society*, vol. 60, no. 6, pp. 1351–1360, 1938.

[43] A. Fahimi, I. Jurewicz, R. J. Smith, C. S. Sharrock, D. A. Bradley, S. J. Henley, J. N. Coleman, and A. B. Dalton, "Density controlled conductivity of pristine graphene films," *Carbon*, vol. 64, pp. 435–443, 2013.

[44] G. Roberts, *Langmuir-Blodgett Films*. Springer Science & Business Media, 2013.

[45] P. Eaton and P. West, *Atomic force microscopy*. Oxford University Press, 2010.

[46] G. Zeng, Y. Duan, F. Besenbacher, and M. Dong, "Nanomechanics of amyloid materials studied by atomic force microscopy," in *Atomic Force Microscopy Investigations into Biology-From Cell to Protein*, InTech, 2012.

[47] W. Melitz, J. Shen, A. C. Kummel, and S. Lee, "Kelvin probe force microscopy and its application," *Surface Science Reports*, vol. 66, no. 1, pp. 1–27, 2011.

[48] C. Kittel, *Introduction to solid state*, vol. 162. John Wiley & Sons New Jersey, 1966.

[49] J. I. Goldstein, D. E. Newbury, J. R. Michael, N. W. Ritchie, J. H. J. Scott, and D. C. Joy, *Scanning electron microscopy and X-ray microanalysis*. Springer, 2017.

[50] S. Kim, S. Park, H. Kim, G. Jang, D. Park, J.-Y. Park, S. Lee, and Y. Ahn, "Characterization of chemical doping of graphene by in-situ raman spectroscopy," *Applied Physics Letters*, vol. 108, no. 20, p. 203111, 2016.

[51] N. Elgrishi, K. J. Rountree, B. D. McCarthy, E. S. Rountree, T. T. Eisenhart, and J. L. Dempsey, "A practical beginner's guide to cyclic voltammetry," *Journal of Chemical Education*, vol. 95, no. 2, pp. 197–206, 2017.

[52] T. A. Witten and L. M. Sander, "Diffusion-limited aggregation," *Physical Review B*, vol. 27, no. 9, p. 5686, 1983.

[53] G.-J. Li, X.-H. Zhang, and S. Kawi, "Relationships between sensitivity, catalytic activity, and surface areas of SnO_2 gas sensors," *Sensors and Actuators B: Chemical*, vol. 60, no. 1, pp. 64–70, 1999.

[54] S. Pohlmann, B. Lobato, T. A. Centeno, and A. Balducci, "The influence of pore size and surface area of activated carbons on the performance of ionic liquid based supercapacitors," *Physical Chemistry Chemical Physics*, vol. 15, no. 40, pp. 17287–17294, 2013.

[55] S. S. Varghese, S. Lonkar, K. Singh, S. Swaminathan, and A. Abdala, "Recent advances in graphene based gas sensors," *Sensors and Actuators B: Chemical*, vol. 218, pp. 160–183, 2015.

[56] T. Zhang, S. Mubeen, N. V. Myung, and M. A. Deshusses, "Recent progress in carbon nanotube-based gas sensors.," *Nanotechnology*, vol. 19, p. 332001, Aug 2008.

[57] J. Theerthagiri, R. Senthil, B. Senthilkumar, A. R. Polu, J. Madhavan, and M. Ashokkumar, "Recent advances in MoS_2 nanostructured materials for energy and environmental applications-a review," *Journal of Solid State Chemistry*, vol. 252, pp. 43–71, 2017.

[58] R. R. Schaller, "Moore's law: past, present and future," *IEEE spectrum*, vol. 34, no. 6, pp. 52–59, 1997.

[59] S. Stankovich, D. A. Dikin, G. H. Dommett, K. M. Kohlhaas, E. J. Zimney, E. A. Stach, R. D. Piner, S. T. Nguyen, and R. S. Ruoff, "Graphene-based composite materials," *Nature*, vol. 442, no. 7100, p. 282, 2006.

[60] M. D. Stoller, S. Park, Y. Zhu, J. An, and R. S. Ruoff, "Graphene-based ultracapacitors.," *Nano Letters*, vol. 8, pp. 3498–502, Oct 2008.

[61] K. S. Novoselov, D. Jiang, F. Schedin, T. J. Booth, V. V. Khotkevich, S. V. Morozov, and A. K. Geim, "Two-dimensional atomic crystals.," *Proceedings of the National Academy of Sciences of the United States of America*, vol. 102, pp. 10451–3, Jul 2005.

[62] P. Blake, P. D. Brimicombe, R. R. Nair, T. J. Booth, D. Jiang, F. Schedin, L. A. Ponomarenko, S. V. Morozov, H. F. Gleeson, E. W. Hill, *et al.*, "Graphene-based liquid crystal device," *Nano letters*, vol. 8, no. 6, pp. 1704–1708, 2008.

[63] Y. Hernandez, V. Nicolosi, M. Lotya, F. M. Blighe, Z. Sun, S. De, I. McGovern, B. Holland, M. Byrne, Y. K. Gun'Ko, *et al.*, "High-yield production of graphene by liquid-phase exfoliation of graphite," *Nature Nanotechnology*, vol. 3, no. 9, p. 563, 2008.

[64] Y. Hernandez, V. Nicolosi, M. Lotya, F. M. Blighe, Z. Sun, S. De, I. T. McGovern, B. Holland, M. Byrne, Y. K. Gun'Ko, J. J. Boland, P. Niraj, G. Duesberg, S. Krishnamurthy, R. Goodhue, J. Hutchison, V. Scardaci, A. C. Ferrari, and J. N. Coleman, "High-yield production of graphene by liquid-phase exfoliation of graphite.," *Nature Nanotechnology*, vol. 3, pp. 563–8, Sep 2008.

[65] M. Lotya, Y. Hernandez, P. J. King, R. J. Smith, V. Nicolosi, L. S. Karlsson, F. M. Blighe, S. De, Z. Wang, I. McGovern, *et al.*, "Liquid phase production of graphene by exfoliation of graphite in surfactant/water solutions," *Journal of the American Chemical Society*, vol. 131, no. 10, pp. 3611–3620, 2009.

[66] P. R. Somani, S. P. Somani, and M. Umeno, "Planer nano-graphenes from camphor by CVD," *Chemical Physics Letters*, vol. 430, no. 1-3, pp. 56–59, 2006.

[67] H. Cao, Q. Yu, R. Colby, D. Pandey, C. Park, J. Lian, D. Zemlyanov, I. Childres, V. Drachev, E. A. Stach, *et al.*, "Large-scale graphitic thin films synthesized on ni and transferred to insulators: Structural and electronic properties," *Journal of Applied Physics*, vol. 107, no. 4, p. 044310, 2010.

[68] S. Bhaviripudi, X. Jia, M. S. Dresselhaus, and J. Kong, "Role of kinetic factors in chemical vapor deposition synthesis of uniform large area graphene using copper catalyst.," *Nano Letters*, vol. 10, pp. 4128–33, Oct 2010.

[69] K. S. Kim, Y. Zhao, H. Jang, S. Y. Lee, J. M. Kim, K. S. Kim, J.-h. Ahn, P. Kim, J.-y. Choi, and B. H. Hong, "Large-scale pattern growth of graphene films for stretchable transparent electrodes.," *Nature*, vol. 457, no. 7230, pp. 706–10, 2009.

[70] X. Li, W. Cai, J. An, S. Kim, J. Nah, D. Yang, R. Piner, A. Velamakanni, I. Jung, E. Tutuc, *et al.*, "Large-area synthesis of high-quality and uniform graphene films on copper foils," *Science*, vol. 324, no. 5932, pp. 1312–1314, 2009.

[71] S. Lee, K. Lee, and Z. Zhong, "Wafer scale homogeneous bilayer graphene films by chemical vapor deposition.," *Nano Letters*, vol. 10, pp. 4702–7, Nov 2010.

[72] A. Reina, X. Jia, J. Ho, D. Nezich, H. Son, V. Bulovic, M. S. Dresselhaus, and J. Kong, "Large area, few-layer graphene films on arbitrary substrates by chemical vapor deposition," *Nano Letters*, vol. 9, no. 1, pp. 30–35, 2008.

[73] J. Wang, M. Zhu, R. A. Outlaw, X. Zhao, D. M. Manos, and B. C. Holloway, "Synthesis of carbon nanosheets by inductively coupled radio-frequency plasma enhanced chemical vapor deposition," *Carbon*, vol. 42, no. 14, pp. 2867–2872, 2004.

[74] A. Malesevic, R. Vitchev, K. Schouteden, A. Volodin, L. Zhang, G. V. Tendeloo, A. Vanhulsel, and C. V. Haesendonck, "Synthesis of few-layer graphene via microwave plasma-enhanced chemical vapour deposition.," *Nanotechnology*, vol. 19, p. 305604, Jul 2008.

[75] R. Vitchev, A. Malesevic, R. H. Petrov, R. Kemps, M. Mertens, A. Vanhulsel, and C. Van Haesendonck, "Initial stages of few-layer graphene growth by microwave plasma-enhanced chemical vapour deposition," *Nanotechnology*, vol. 21, no. 9, p. 095602, 2010.

[76] M. Zhu, J. Wang, B. C. Holloway, R. Outlaw, X. Zhao, K. Hou, V. Shutthanandan, and D. M. Manos, "A mechanism for carbon nanosheet formation," *Carbon*, vol. 45, no. 11, pp. 2229–2234, 2007.

[77] G. Nandamuri, S. Roumimov, and R. Solanki, "Remote plasma assisted growth of graphene films," *Applied Physics Letters*, vol. 96, no. 15, p. 154101, 2010.

[78] S. Bae, H. Kim, Y. Lee, X. Xu, J.-S. Park, Y. Zheng, J. Balakrishnan, T. Lei, H. R. Kim, Y. I. Song, Y.-J. Kim, K. S. Kim, B. Ozyilmaz, J.-H. Ahn, B. H. Hong, and S. Iijima, "Roll-to-roll production of 30-inch graphene films for transparent electrodes.," *Nature Nanotechnology*, vol. 5, pp. 574–8, Aug 2010.

[79] T. Hesjedal, "Continuous roll-to-roll growth of graphene films by chemical vapor deposition," *Applied Physics Letters*, vol. 98, no. 13, p. 133106, 2011.

[80] T. Yamada, M. Ishihara, J. Kim, M. Hasegawa, and S. Iijima, "A roll-to-roll microwave plasma chemical vapor deposition process for the production of 294 mm width graphene films at low temperature," *Carbon*, vol. 50, no. 7, pp. 2615–2619, 2012.

[81] T. Kobayashi, M. Bando, N. Kimura, K. Shimizu, K. Kadono, N. Umezu, K. Miyahara, S. Hayazaki, S. Nagai, Y. Mizuguchi, *et al.*, "Production of a 100m long high-quality graphene transparent conductive film by roll-to-roll chemical vapor deposition and transfer process," *Applied Physics Letters*, vol. 102, no. 2, p. 023112, 2013.

[82] B. N. Chandrashekar, B. Deng, A. S. Smitha, Y. Chen, C. Tan, H. Zhang, H. Peng, and Z. Liu, "Roll-to-roll green transfer of CVD graphene onto plastic for a transparent and flexible triboelectric nanogenerator," *Advanced Materials*, vol. 27, no. 35, pp. 5210–5216, 2015.

[83] M. A. Alrefae, A. Kumar, P. Pandita, A. Candadai, I. Bilionis, and T. S. Fisher, "Process optimization of graphene growth in a roll-to-roll plasma CVD system," *AIP Advances*, vol. 7, no. 11, p. 115102, 2017.

[84] P. R. Kidambi, D. D. Mariappan, N. T. Dee, A. Vyatskikh, S. Zhang, R. Karnik, and A. J. Hart, "A scalable route to nanoporous large-area atomically thin graphene membranes by roll-to-roll chemical vapor deposition and polymer support casting," *ACS Applied Materials & Interfaces*, vol. 10, no. 12, pp. 10369–10378, 2018.

[85] J. Hass, R. Feng, T. Li, X. Li, Z. Zong, W. De Heer, P. First, E. Conrad, C. Jeffrey, and C. Berger, "Highly ordered graphene for two dimensional electronics," *Applied Physics Letters*, vol. 89, no. 14, p. 143106, 2006.

[86] F. Varchon, R. Feng, J. Hass, X. Li, B. N. Nguyen, C. Naud, P. Mallet, J.-Y. Veuillen, C. Berger, E. H. Conrad, *et al.*, "Electronic structure of epitaxial graphene layers on SiC: effect of the substrate," *Physical Rreview Letters*, vol. 99, no. 12, p. 126805, 2007.

[87] Z. Zhang, Z. Sun, J. Yao, D. V. Kosynkin, and J. M. Tour, "Transforming carbon nanotube devices into nanoribbon devices.," *Journal of the American Chemical Society*, vol. 131, pp. 13460–3, Sep 2009.

[88] S. Dhakate, N. Chauhan, S. Sharma, and R. Mathur, "The production of multilayer graphene nanoribbons from thermally reduced unzipped multi-walled carbon nanotubes," *Carbon*, vol. 49, no. 13, pp. 4170–4178, 2011.

[89] A. L. Higginbotham, D. V. Kosynkin, A. Sinitskii, Z. Sun, and J. M. Tour, "Lower-defect graphene oxide nanoribbons from multiwalled carbon nanotubes.," *ACS Nano*, vol. 4, pp. 2059–69, Apr 2010.

[90] L. Jiao, L. Zhang, X. Wang, G. Diankov, and H. Dai, "Narrow graphene nanoribbons from carbon nanotubes.," *Nature*, vol. 458, pp. 877–80, Apr 2009.

[91] D. V. Kosynkin, A. L. Higginbotham, A. Sinitskii, J. R. Lomeda, A. Dimiev, B. K. Price, and J. M. Tour, "Longitudinal unzipping of carbon nanotubes to form graphene nanoribbons.," *Nature*, vol. 458, pp. 872–6, Apr 2009.

[92] S. Mohammadi, Z. Kolahdouz, S. Darbari, S. Mohajerzadeh, and N. Masoumi, "Graphene formation by unzipping carbon nanotubes using a sequential plasma assisted processing," *Carbon*, vol. 52, pp. 451–463, 2013.

[93] J. Chen, L. Chen, Z. Zhang, J. Li, L. Wang, and W. Jiang, "Graphene layers produced from carbon nanotubes by friction," *Carbon*, vol. 50, no. 5, pp. 1934–1941, 2012.

[94] H. He, J. Klinowski, M. Forster, and A. Lerf, "A new structural model for graphite oxide," *Chemical Physics Letters*, vol. 287, no. 1-2, pp. 53–56, 1998.

[95] O. C. Compton and S. T. Nguyen, "Graphene oxide, highly reduced graphene oxide, and graphene: versatile building blocks for carbon-based materials," *Small*, vol. 6, no. 6, pp. 711–723, 2010.

[96] S. Pei and H.-M. Cheng, "The reduction of graphene oxide," *Carbon*, vol. 50, no. 9, pp. 3210–3228, 2012.

[97] D. Li, M. B. Müller, S. Gilje, R. B. Kaner, and G. G. Wallace, "Processable aqueous dispersions of graphene nanosheets.," *Nature Nanotechnology*, vol. 3, pp. 101–5, Feb 2008.

[98] G. Wang, J. Yang, J. Park, X. Gou, B. Wang, H. Liu, and J. Yao, "Facile synthesis and characterization of graphene nanosheets," *The Journal of Physical Chemistry C*, vol. 112, no. 22, pp. 8192–8195, 2008.

[99] C. Deng, H. Hu, X. Ge, C. Han, D. Zhao, and G. Shao, "One-pot sonochemical fabrication of hierarchical hollow CuO submicrospheres.," *Ultrasonics Sonochemistry*, vol. 18, pp. 932–7, Sep 2011.

[100] D. V. Pinjari and A. B. Pandit, "Room temperature synthesis of crystalline CeO_2 nanopowder: advantage of sonochemical method over conventional method.," *Ultrasonics Sonochemistry*, vol. 18, pp. 1118–23, Sep 2011.

[101] V. Safarifard and A. Morsali, "Sonochemical syntheses of a nano-sized copper (II) supramolecule as a precursor for the synthesis of copper (II) oxide nanoparticles," *Ultrasonics Sonochemistry*, vol. 19, no. 4, pp. 823–829, 2012.

[102] K. Krishnamoorthy, G.-S. Kim, and S. J. Kim, "Graphene nanosheets: Ultrasound assisted synthesis and characterization.," *Ultrasonics Sonochemistry*, vol. 20, pp. 644–9, Mar 2013.

[103] V. Abdelsayed, S. Moussa, H. M. Hassan, H. S. Aluri, M. M. Collinson, and M. S. El-Shall, "Photothermal deoxygenation of graphite oxide with laser excitation in solution and graphene-aided increase in water temperature," *The Journal of Physical Chemistry Letters*, vol. 1, no. 19, pp. 2804–2809, 2010.

[104] E. Kymakis, C. Petridis, T. D. Anthopoulos, and E. Stratakis, "Laser-assisted reduction of graphene oxide for flexible, large-area optoelectronics," *IEEE Journal of Selected Topics in Quantum Electronics*, vol. 20, no. 1, pp. 106–115, 2014.

[105] M. F. El-Kady, V. Strong, S. Dubin, and R. B. Kaner, "Laser scribing of high-performance and flexible graphene-based electrochemical capacitors.," *Science (New York, N.Y.)*, vol. 335, pp. 1326–30, Mar 2012.

[106] R. Trusovas, K. Ratautas, G. Ravciukaitis, J. Barkauskas, I. Stankevivciene, G. Niaura, and R. Mavzeikiene, "Reduction of graphite oxide to graphene with laser irradiation," *Carbon*, vol. 52, pp. 574–582, 2013.

[107] H. F. Teoh, Y. Tao, E. S. Tok, G. W. Ho, and C. H. Sow, "Direct laser-enabled graphene oxide–reduced graphene oxide layered structures with micropatterning," *Journal of Applied Physics*, vol. 112, no. 6, p. 064309, 2012.

[108] Y. Guan, Y. Fang, G. Lim, H. Zheng, and M. Hong, "Fabrication of laser-reduced graphene oxide in liquid nitrogen environment," *Scientific Reports*, vol. 6, 2016.

[109] D. A. Sokolov, C. M. Rouleau, D. B. Geohegan, and T. M. Orlando, "Excimer laser reduction and patterning of graphite oxide," *Carbon*, vol. 53, pp. 81–89, 2013.

[110] C. Petridis, Y.-H. Lin, K. Savva, G. Eda, E. Kymakis, T. Anthopoulos, and E. Stratakis, "Post-fabrication, in situ laser reduction of graphene oxide devices," *Applied Physics Letters*, vol. 102, no. 9, p. 093115, 2013.

[111] Y. Zhang, L. Guo, S. Wei, Y. He, H. Xia, Q. Chen, H.-B. Sun, and F.-S. Xiao, "Direct imprinting of microcircuits on graphene oxides film by femtosecond laser reduction," *Nano Today*, vol. 5, no. 1, pp. 15–20, 2010.

[112] V. Strong, S. Dubin, M. F. El-Kady, A. Lech, Y. Wang, B. H. Weiller, and R. B. Kaner, "Patterning and electronic tuning of laser scribed graphene for flexible all-carbon devices.," *ACS Nano*, vol. 6, pp. 1395–403, Feb 2012.

[113] L. J. Cote, R. Cruz-Silva, and J. Huang, "Flash reduction and patterning of graphite oxide and its polymer composite.," *Journal of the American Chemical Society*, vol. 131, pp. 11027–32, Aug 2009.

[114] G. Williams, B. Seger, and P. V. Kamat, "TiO_2-graphene nanocomposites. uv-assisted photocatalytic reduction of graphene oxide.," *ACS Nano*, vol. 2, pp. 1487–91, Jul 2008.

[115] O. Akhavan and E. Ghaderi, "Photocatalytic reduction of graphene oxide nanosheets on TiO_2 thin film for photoinactivation of bacteria in solar light irradiation," *The Journal of Physical Chemistry C*, vol. 113, no. 47, pp. 20214–20220, 2009.

[116] D. A. Pennington, A. R. Clayton, K. L. Juda, C. Paukner, L. Kurzepa, J. C. R. H. ST, K. K. Koziol, and J. Y.-z. Joaug, "Apparatus and method for plasma synthesis of graphitic products including graphene," 2015.

[117] A. C. Ferrari, J. Meyer, V. Scardaci, C. Casiraghi, M. Lazzeri, F. Mauri, S. Piscanec, D. Jiang, K. Novoselov, S. Roth, *et al.*, "Raman spectrum of graphene and graphene layers," *Physical Review Letters*, vol. 97, no. 18, p. 187401, 2006.

[118] M. Inagaki, J. Qiu, and Q. Guo, "Carbon foam: preparation and application," *Carbon*, vol. 87, pp. 128–152, 2015.

[119] J. Klett, R. Hardy, E. Romine, C. Walls, and T. Burchell, "High-thermal-conductivity, mesophase-pitch-derived carbon foams: effect of precursor on structure and properties," *Carbon*, vol. 38, no. 7, pp. 953–973, 2000.

[120] S. Li, Y. Tian, Y. Zhong, X. Yan, Y. Song, Q. Guo, J. Shi, and L. Liu, "Formation mechanism of carbon foams derived from mesophase pitch," *Carbon*, vol. 49, no. 2, pp. 618–624, 2011.

[121] J. Zhu, X. Wang, L. Guo, Y. Wang, Y. Wang, M. Yu, and K.-t. Lau, "A graphite foam reinforced by graphite particles," *Carbon*, vol. 45, no. 13, pp. 2547–2550, 2007.

[122] C. Leroy, F. Carn, R. Backov, M. Trinquecoste, and P. Delhaes, "Multiwalled-carbon-nanotube-based carbon foams," *Carbon*, vol. 45, no. 11, pp. 2317–2320, 2007.

[123] T. Beechem and K. Lafdi, "Novel high strength graphitic foams," *Carbon*, vol. 44, no. 8, pp. 1548–1559, 2006.

[124] A. G. Chakhovskoi, C. E. Hunt, G. Forsberg, T. Nilsson, and P. Persson, "Reticulated vitreous carbon field emission cathodes for light source applications," *Journal of Vacuum Science & Technology B: Microelectronics and Nanometer Structures Processing, Measurement, and Phenomena*, vol. 21, no. 1, pp. 571–575, 2003.

[125] S.-p. Zhang, M.-x. Liu, L.-h. Gan, F.-r. Wu, Z.-j. Xu, Z.-x. Hao, and L.-w. Chen, "Synthesis of carbon foams with a high compressive strength from arylacetylene," *New Carbon Materials*, vol. 25, no. 1, pp. 9–14, 2010.

[126] G. Harikrishnan, T. U. Patro, and D. Khakhar, "Reticulated vitreous carbon from polyurethane foam-clay composites," *Carbon*, vol. 45, no. 3, pp. 531–535, 2007.

[127] K. Lafdi, M. Almajali, and O. Huzayyin, "Thermal properties of copper-coated carbon foams," *Carbon*, vol. 47, no. 11, pp. 2620–2626, 2009.

[128] M. Almajali, K. Lafdi, P. Prodhomme, and O. Ochoa, "Mechanical properties of copper-coated carbon foams," *Carbon*, vol. 48, no. 5, pp. 1604–1608, 2010.

[129] M. Almajali and K. Lafdi, "Assessment of carbon foam geometry during copper coating," *Carbon*, vol. 48, no. 15, pp. 4238–4247, 2010.

[130] K. T. Lee, J. C. Lytle, N. S. Ergang, S. M. Oh, and A. Stein, "Synthesis and rate performance of monolithic macroporous carbon electrodes for lithium-ion secondary batteries," *Advanced Functional Materials*, vol. 15, no. 4, pp. 547–556, 2005.

[131] S. Mayer, R. Pekala, and J. Kaschmitter, "The aerocapacitor: An electrochemical double-layer energy-storage device," *Journal of the Electrochemical Society*, vol. 140, no. 2, pp. 446–451, 1993.

[132] J. Han, K. Cho, K.-H. Lee, and H. Kim, "Porous graphite matrix for chemical heat pumps," *Carbon*, vol. 36, no. 12, pp. 1801–1810, 1998.

[133] R. W. Pekala and R. W. Hopper, "Low-density microcellular carbon foams," *Journal of Materials Science*, vol. 22, no. 5, pp. 1840–1844, 1987.

[134] K. Murakami, Y. Satoh, I. Ogino, and S. R. Mukai, "Synthesis of a monolithic carbon-based acid catalyst with a honeycomb structure for flow reaction systems," *Industrial & Engineering Chemistry Research*, vol. 52, no. 44, pp. 15372–15376, 2013.

[135] X. Wang, Q. Guo, Y. Zhong, X. Wei, and L. Liu, "Heat transfer enhancement of neopentyl glycol using compressed expanded natural graphite for thermal energy storage," *Renewable Energy*, vol. 51, pp. 241–246, 2013.

[136] Y. Xu, K. Sheng, C. Li, and G. Shi, "Self-assembled graphene hydrogel via a one-step hydrothermal process.," *ACS Nano*, vol. 4, pp. 4324–30, Jul 2010.

[137] J. Zhao, W. Ren, and H.-M. Cheng, "Graphene sponge for efficient and repeatable adsorption and desorption of water contaminations," *Journal of Materials Chemistry*, vol. 22, no. 38, pp. 20197–20202, 2012.

[138] H. D. Pham, V. H. Pham, T. V. Cuong, T.-D. Nguyen-Phan, J. S. Chung, E. W. Shin, and S. Kim, "Synthesis of the chemically converted graphene xerogel with superior electrical conductivity," *Chemical Communications*, vol. 47, no. 34, pp. 9672–9674, 2011.

[139] W. Chen and L. Yan, "In situ self-assembly of mild chemical reduction graphene for three-dimensional architectures," *Nanoscale*, vol. 3, no. 8, pp. 3132–3137, 2011.

[140] X. Zhang, Z. Sui, B. Xu, S. Yue, Y. Luo, W. Zhan, and B. Liu, "Mechanically strong and highly conductive graphene aerogel and its use as electrodes for electrochemical power sources," *Journal of Materials Chemistry*, vol. 21, no. 18, pp. 6494–6497, 2011.

[141] H. Hu, Z. Zhao, W. Wan, Y. Gogotsi, and J. Qiu, "Ultralight and highly compressible graphene aerogels.," *Advanced Materials (Deerfield Beach, Fla.)*, vol. 25, pp. 2219–23, Apr 2013.

[142] S. H. Lee, H. W. Kim, J. O. Hwang, W. J. Lee, J. Kwon, C. W. Bielawski, R. S. Ruoff, and S. O. Kim, "Three-dimensional self-assembly of graphene oxide platelets into mechanically flexible macroporous carbon films.," *Angewandte Chemie (International ed. in English)*, vol. 49, pp. 10084–8, Dec 2010.

[143] H. Sun, Z. Xu, and C. Gao, "Multifunctional, ultra-flyweight, synergistically assembled carbon aerogels.," *Advanced Materials (Deerfield Beach, Fla.)*, vol. 25, pp. 2554–60, May 2013.

[144] Y. Tao, X. Xie, W. Lv, D.-M. Tang, D. Kong, Z. Huang, H. Nishihara, T. Ishii, B. Li, D. Golberg, *et al.*, "Towards ultrahigh volumetric capacitance: graphene derived highly dense but porous carbons for supercapacitors," *Scientific Reports*, vol. 3, p. 2975, 2013.

[145] H. Bi, K. Yin, X. Xie, Y. Zhou, N. Wan, F. Xu, F. Banhart, L. Sun, and R. S. Ruoff, "Low temperature casting of graphene with high compressive strength.," *Advanced Materials (Deerfield Beach, Fla.)*, vol. 24, pp. 5124–9, 5123, Sep 2012.

[146] Z. Chen, W. Ren, L. Gao, B. Liu, S. Pei, and H.-M. Cheng, "Three-dimensional flexible and conductive interconnected graphene networks grown by chemical vapour deposition.," *Nature Materials*, vol. 10, pp. 424–8, Jun 2011.

[147] F. Xia, L. T. Yang, L. Wang, and A. Vinel, "Internet of things," *International Journal of Communication Systems*, vol. 25, no. 9, pp. 1101–1102, 2012.

[148] J. M. Samet, S. L. Zeger, F. Dominici, F. Curriero, I. Coursac, D. W. Dockery, J. Schwartz, and A. Zanobetti, "The national morbidity, mortality, and air pollution study," *Part II: morbidity and mortality from air pollution in the United States Res Rep Health Eff Inst*, vol. 94, no. pt 2, pp. 5–79, 2000.

[149] C. Wang, L. Yin, L. Zhang, D. Xiang, and R. Gao, "Metal oxide gas sensors: sensitivity and influencing factors," *Sensors*, vol. 10, no. 3, pp. 2088–2106, 2010.

[150] E. Comini, G. Faglia, and G. Sberveglieri, *Solid State Gas Sensing*, vol. 20. Springer Science & Business Media, 2008.

[151] H. Pinto and A. Markevich, "Electronic and electrochemical doping of graphene by surface adsorbates," *Beilstein Journal of Nanotechnology*, vol. 5, no. 1, pp. 1842–1848, 2014.

[152] S. Rumyantsev, G. Liu, M. S. Shur, R. A. Potyrailo, and A. A. Balandin, "Selective gas sensing with a single pristine graphene transistor," *Nano Letters*, vol. 12, no. 5, pp. 2294–2298, 2012.

[153] G. S. Kulkarni, K. Reddy, Z. Zhong, and X. Fan, "Graphene nanoelectronic heterodyne sensor for rapid and sensitive vapour detection," *Nature Communications*, vol. 5, p. 4376, 2014.

[154] Z. Ben Aziza, Q. Zhang, and D. Baillargeat, "Graphene/mica based ammonia gas sensors," *Applied Physics Letters*, vol. 105, no. 25, p. 254102, 2014.

[155] T. Wang, D. Huang, Z. Yang, S. Xu, G. He, X. Li, N. Hu, G. Yin, D. He, and L. Zhang, "A review on graphene-based gas/vapor sensors with unique properties and potential applications," *Nano-Micro Letters*, vol. 8, no. 2, pp. 95–119, 2016.

[156] F. Yavari and N. Koratkar, "Graphene-based chemical sensors," *The Journal of Physical Chemistry Letters*, vol. 3, no. 13, pp. 1746–1753, 2012.

[157] H. J. Yoon, J. H. Yang, Z. Zhou, S. S. Yang, M. M.-C. Cheng, *et al.*, "Carbon dioxide gas sensor using a graphene sheet," *Sensors and Actuators B: Chemical*, vol. 157, no. 1, pp. 310–313, 2011.

[158] F. Yavari, E. Castillo, H. Gullapalli, P. M. Ajayan, and N. Koratkar, "High sensitivity detection of NO_2 and NH_3 in air using chemical vapor deposition grown graphene," *Applied Physics Letters*, vol. 100, no. 20, p. 203120, 2012.

[159] M. G. Chung, D. H. Kim, H. M. Lee, T. Kim, J. H. Choi, D. kyun Seo, J.-B. Yoo, S.-H. Hong, T. J. Kang, and Y. H. Kim, "Highly sensitive NO_2 gas sensor based on ozone treated graphene," *Sensors and Actuators B: Chemical*, vol. 166, pp. 172–176, 2012.

[160] E. Massera, V. La Ferrara, M. Miglietta, T. Polichetti, I. Nasti, and G. Di Francia, "Gas sensors based on graphene," *Chemistry Today*, vol. 29, no. 1, 2011.

[161] K. Nemade and S. Waghuley, "Chemiresistive gas sensing by few-layered graphene," *Journal of Electronic Materials*, vol. 42, no. 10, pp. 2857–2866, 2013.

[162] H. Choi, H. Y. Jeong, D.-S. Lee, S.-Y. Choi, and C.-G. Choi, "Flexible NO_2 gas sensor using multilayer graphene films by chemical vapor deposition," *Carbon Letters*, vol. 14, no. 3, pp. 186–189, 2013.

[163] H. Bai and G. Shi, "Gas sensors based on conducting polymers," *Sensors*, vol. 7, no. 3, pp. 267–307, 2007.

[164] J.-H. Chen, C. Jang, S. Adam, M. Fuhrer, E. Williams, and M. Ishigami, "Charged-impurity scattering in graphene," *Nature Physics*, vol. 4, no. 5, p. 377, 2008.

[165] Y.-H. Zhang, Y.-B. Chen, K.-G. Zhou, C.-H. Liu, J. Zeng, H.-L. Zhang, and Y. Peng, "Improving gas sensing properties of graphene by introducing dopants and defects: a first-principles study," *Nanotechnology*, vol. 20, no. 18, p. 185504, 2009.

[166] H. E. Romero, P. Joshi, A. K. Gupta, H. R. Gutierrez, M. W. Cole, S. A. Tadigadapa, and P. C. Eklund, "Adsorption of ammonia on graphene.," *Nanotechnology*, vol. 20, p. 245501, Jun 2009.

[167] Y. Dan, Y. Lu, N. J. Kybert, Z. Luo, and A. T. C. Johnson, "Intrinsic response of graphene vapor sensors.," *Nano Letters*, vol. 9, pp. 1472–5, Apr 2009.

[168] P. L. Levesque, S. S. Sabri, C. M. Aguirre, J. Guillemette, M. Siaj, P. Desjardins, T. Szkopek, and R. Martel, "Probing charge transfer at surfaces using graphene transistors," *Nano Letters*, vol. 11, no. 1, pp. 132–137, 2010.

[169] P. A. Denis and F. Iribarne, "Comparative study of defect reactivity in graphene," *The Journal of Physical Chemistry C*, vol. 117, no. 37, pp. 19048–19055, 2013.

[170] Y. Liu, H. Liu, Y. Chu, Y. Cui, T. Hayasaka, V. Dasaka, L. Nguyen, and L. Lin, "Defect-induced gas adsorption on graphene transistors," *Advanced Materials Interfaces*, 2018.

[171] F. Yavari, Z. Chen, A. V. Thomas, W. Ren, H.-M. Cheng, and N. Koratkar, "High sensitivity gas detection using a macroscopic three-dimensional graphene foam network," *Scientific Reports*, vol. 1, p. 166, 2011.

[172] X. Liu, J. Cui, J. Sun, and X. Zhang, "3D graphene aerogel-supported SnO_2 nanoparticles for efficient detection of NO_2," *Rsc Advances*, vol. 4, no. 43, pp. 22601–22605, 2014.

[173] L. Li, M. Liu, S. He, and W. Chen, "Freestanding 3D mesoporous Co_3O_4@ carbon foam nanostructures for ethanol gas sensing," *Analytical Chemistry*, vol. 86, no. 15, pp. 7996–8002, 2014.

[174] L. Li, S. He, M. Liu, C. Zhang, and W. Chen, "Three-dimensional mesoporous graphene aerogel-supported SnO_2 nanocrystals for high-performance NO_2 gas sensing at low temperature," *Analytical Chemistry*, vol. 87, no. 3, pp. 1638–1645, 2015.

[175] X. Liu, J. Li, J. Sun, and X. Zhang, "3D Fe_3O_4 nanoparticle/graphene aerogel for NO_2 sensing at room temperature," *RSC Advances*, vol. 5, no. 90, pp. 73699–73704, 2015.

[176] X. Liu, J. Sun, and X. Zhang, "Novel 3D graphene aerogel-ZnO composites as efficient detection for NO_2 at room temperature," *Sensors and Actuators B: Chemical*, vol. 211, pp. 220–226, 2015.

[177] L. Li, C. Zhang, R. Zhang, X. Gao, S. He, M. Liu, X. Li, and W. Chen, "2d ultrathin Co_3O_4 nanosheet array deposited on 3D carbon foam for enhanced ethanol gas sensing application," *Sensors and Actuators B: Chemical*, vol. 244, pp. 664–672, 2017.

[178] H. Long, A. Harley-Trochimczyk, T. Pham, Z. Tang, T. Shi, A. Zettl, C. Carraro, M. A. Worsley, and R. Maboudian, "High surface area MoS_2/graphene hybrid aerogel for ultrasensitive NO_2 detection," *Advanced Functional Materials*, vol. 26, no. 28, pp. 5158–5165, 2016.

[179] Y. Xue, J. Liu, H. Chen, R. Wang, D. Li, J. Qu, and L. Dai, "Nitrogen-doped graphene foams as metal-free counter electrodes in high-performance dye-sensitized solar cells," *Angewandte Chemie International Edition*, vol. 51, no. 48, pp. 12124–12127, 2012.

[180] L.-Z. Fan, Y.-S. Hu, J. Maier, P. Adelhelm, B. Smarsly, and M. Antonietti, "High electroactivity of polyaniline in supercapacitors by using a hierarchically porous carbon monolith as a support," *Advanced Functional Materials*, vol. 17, no. 16, pp. 3083–3087, 2007.

[181] Z.-Y. Sui, Y.-N. Meng, P.-W. Xiao, Z.-Q. Zhao, Z.-X. Wei, and B.-H. Han, "Nitrogen-doped graphene aerogels as efficient supercapacitor electrodes and gas adsorbents," *ACS Applied Materials & Interfaces*, vol. 7, no. 3, pp. 1431–1438, 2015.

[182] J. Chen, J. Xu, S. Zhou, N. Zhao, and C.-P. Wong, "Nitrogen-doped hierarchically porous carbon foam: a free-standing electrode and mechanical support for high-performance supercapacitors," *Nano Energy*, vol. 25, pp. 193–202, 2016.

[183] S. Y. Sawant, T. H. Han, S. A. Ansari, J. H. Shim, A. T. N. Nguyen, J.-J. Shim, and M. H. Cho, "A metal-free and non-precious multifunctional 3D carbon foam for high-energy density supercapacitors and enhanced power generation in microbial fuel cells," *Journal of Industrial and Engineering Chemistry*, 2017.

[184] Z. Xin, W. Fang, L. Zhao, H. Chen, X. He, and W. Zhang, "N-doped carbon foam constructed by liquid foam with hierarchical porous structure for supercapacitor," *Journal of Porous Materials*, pp. 1–9, 2018.

[185] R. T. Woodward, F. Markoulidis, F. De Luca, D. B. Anthony, D. Malko, T. O. McDonald, M. S. Shaffer, and A. Bismarck, "Carbon foams from emulsion-templated reduced graphene oxide polymer composites: electrodes for supercapacitor devices," *Journal of Materials Chemistry A*, vol. 6, no. 4, pp. 1840–1849, 2018.

[186] J. Miller, B. Dunn, T. Tran, and R. Pekala, "Deposition of ruthenium nanoparticles on carbon aerogels for high energy density supercapacitor electrodes," *Journal of the Electrochemical Society*, vol. 144, no. 12, pp. L309–L311, 1997.

[187] A. E. Fischer, K. A. Pettigrew, D. R. Rolison, R. M. Stroud, and J. W. Long, "Incorporation of homogeneous, nanoscale MnO_2 within ultraporous carbon structures via self-limiting electroless deposition: implications for electrochemical capacitors," *Nano Letters*, vol. 7, no. 2, pp. 281–286, 2007.

[188] E. Spanakis, M. Pervolaraki, J. Giapintzakis, N. Katsarakis, E. Koudoumas, and D. Vernardou, "Effect of gold and silver nanoislands on the electrochemical properties of carbon nanofoam," *Electrochimica Acta*, vol. 111, pp. 305–313, 2013.

[189] S. He, H. Hou, and W. Chen, "3D porous and ultralight carbon hybrid nanostructure fabricated from carbon foam covered by monolayer of nitrogen-doped carbon nanotubes for high performance supercapacitors," *Journal of Power Sources*, vol. 280, pp. 678–686, 2015.

[190] X. Zhang, J. Zhao, X. He, Q. Li, C. Ao, T. Xia, W. Zhang, C. Lu, and Y. Deng, "Mechanically robust and highly compressible electrochemical supercapacitors from nitrogen-doped carbon aerogels," *Carbon*, vol. 127, pp. 236–244, 2018.

[191] B. Timmer, W. Olthuis, and A. Van Den Berg, "Ammonia sensors and their applications-a review," *Sensors and Actuators B: Chemical*, vol. 107, no. 2, pp. 666–677, 2005.

[192] Z. Wu, X. Chen, S. Zhu, Z. Zhou, Y. Yao, W. Quan, and B. Liu, "Enhanced sensitivity of ammonia sensor using graphene/polyaniline nanocomposite," *Sensors and Actuators B: Chemical*, vol. 178, pp. 485–493, 2013.

[193] L. Wang, Z. Lou, R. Zhang, T. Zhou, J. Deng, and T. Zhang, "Hybrid Co_3O_4/SnO_2 core-shell nanospheres as real-time rapid-response sensors for ammonia gas," *ACS Applied Materials & Interfaces*, vol. 8, no. 10, pp. 6539–6545, 2016.

[194] M. Eising, C. E. Cava, R. V. Salvatierra, A. J. G. Zarbin, and L. S. Roman, "Doping effect on self-assembled films of polyaniline and carbon nanotube applied as ammonia gas sensor," *Sensors and Actuators B: Chemical*, vol. 245, pp. 25–33, 2017.

[195] M. Gautam and A. H. Jayatissa, "Ammonia gas sensing behavior of graphene surface decorated with gold nanoparticles," *Solid-State Electronics*, vol. 78, pp. 159–165, 2012.

[196] S. Nufer, M. J. Large, A. A. King, S. P. Ogilvie, A. Brunton, and A. B. Dalton, "Edge selective gas detection using langmuir films of graphene platelets," *ACS Applied Materials & Interfaces*, 2018.

[197] M. Gautam and A. H. Jayatissa, "Graphene based field effect transistor for the detection of ammonia," *Journal of Applied Physics*, vol. 112, no. 6, p. 064304, 2012.

[198] A. Inaba, K. Yoo, Y. Takei, K. Matsumoto, and I. Shimoyama, "Ammonia gas sensing using a graphene field-effect transistor gated by ionic liquid," *Sensors and Actuators B: Chemical*, vol. 195, pp. 15–21, 2014.

[199] G. Lu, L. E. Ocola, and J. Chen, "Reduced graphene oxide for room-temperature gas sensors," *Nanotechnology*, vol. 20, p. 445502, Nov 2009.

[200] J. T. Robinson, F. K. Perkins, E. S. Snow, Z. Wei, and P. E. Sheehan, "Reduced graphene oxide molecular sensors.," *Nano Letters*, vol. 8, pp. 3137–40, Oct 2008.

[201] D. Kostiuk, S. Luby, M. Demydenko, M. Jergel, P. Siffalovic, J. Ivanco, and E. Majkova, "Few-layer graphene langmuir-schaefer nanofilms for H_2 gas sensing," *Procedia Engineering*, vol. 168, pp. 243–246, 2016.

[202] K. Chikkadi, *Wafer-scale integration of single-walled carbon nanotubes for gas sensing*, vol. 19. ETH Zurich, 2014.

[203] A. Baranov, D. Spirjakin, S. Akbari, and A. Somov, "Optimization of power consumption for gas sensor nodes: A survey," *Sensors and Actuators A: Physical*, vol. 233, pp. 279–289, 2015.

[204] S. E. Moon, H. K. Lee, N. J. Choi, J. Lee, W. S. Yang, J. Kim, J. J. Jong, and D. J. Yoo, "Low-power-consumption metal oxide NO_2 gas sensor based on micro-heater and screen printing technology.," *Journal of Nanoscience and Nanotechnology*, vol. 12, pp. 5543–6, Jul 2012.

[205] Y. Zhang, L. Zhang, and C. Zhou, "Review of chemical vapor deposition of graphene and related applications," *Accounts of Chemical Research*, vol. 46, no. 10, pp. 2329–2339, 2013.

[206] Y. Shao, J. Wang, H. Wu, J. Liu, I. A. Aksay, and Y. Lin, "Graphene based electrochemical sensors and biosensors: a review," *Electroanalysis*, vol. 22, no. 10, pp. 1027–1036, 2010.

[207] W. Yuan and G. Shi, "Graphene-based gas sensors," *Journal of Materials Chemistry A*, vol. 1, no. 35, pp. 10078–10091, 2013.

[208] G. Chen, T. M. Paronyan, and A. R. Harutyunyan, "Sub-ppt gas detection with pristine graphene," *Applied Physics Letters*, vol. 101, no. 5, p. 053119, 2012.

[209] A. Lipatov, A. Varezhnikov, P. Wilson, V. Sysoev, A. Kolmakov, and A. Sinitskii, "Highly selective gas sensor arrays based on thermally reduced graphene oxide.," *Nanoscale*, vol. 5, pp. 5426–34, Jun 2013.

[210] G. Lu, S. Park, K. Yu, R. S. Ruoff, L. E. Ocola, D. Rosenmann, and J. Chen, "Toward practical gas sensing with highly reduced graphene oxide: a new signal processing method to circumvent run-to-run and device-to-device variations," *ACS Nano*, vol. 5, no. 2, pp. 1154–1164, 2011.

[211] S. Some, Y. Xu, Y. Kim, Y. Yoon, H. Qin, A. Kulkarni, T. Kim, and H. Lee, "Highly sensitive and selective gas sensor using hydrophilic and hydrophobic graphenes," *Scientific Reports*, vol. 3, p. 1868, 2013.

[212] L. Zhou, F. Shen, X. Tian, D. Wang, T. Zhang, and W. Chen, "Stable Cu_2O nanocrystals grown on functionalized graphene sheets and room temperature H_2S gas sensing with ultrahigh sensitivity," *Nanoscale*, vol. 5, no. 4, pp. 1564–1569, 2013.

[213] G. Ko, H.-Y. Kim, J. Ahn, Y.-M. Park, K.-Y. Lee, and J. Kim, "Graphene-based nitrogen dioxide gas sensors," *Current Applied Physics*, vol. 10, no. 4, pp. 1002–1004, 2010.

[214] Q. T. Tran, T. M. H. Huynh, D. T. Tong, N. D. Nguyen, *et al.*, "Synthesis and application of graphene–silver nanowires composite for ammonia gas sensing," *Advances in Natural Sciences: Nanoscience and Nanotechnology*, vol. 4, no. 4, p. 045012, 2013.

[215] P. Avouris and C. Dimitrakopoulos, "Graphene: synthesis and applications," *Materials Today*, vol. 15, no. 3, pp. 86–97, 2012.

[216] K. Yu, Z. Bo, G. Lu, S. Mao, S. Cui, Y. Zhu, X. Chen, R. S. Ruoff, and J. Chen, "Growth of carbon nanowalls at atmospheric pressure for one-step gas sensor fabrication.," *Nanoscale Research Letters*, vol. 6, no. 1, p. 202, 2011.

[217] F. Rao, H. Almumen, Z. Fan, W. Li, and L. Dong, "Inter-sheet-effect-inspired graphene sensors: design, fabrication and characterization," *Nanotechnology*, vol. 23, no. 10, p. 105501, 2012.

[218] A. Das, S. Pisana, B. Chakraborty, S. Piscanec, S. Saha, U. Waghmare, K. Novoselov, H. Krishnamurthy, A. Geim, A. Ferrari, *et al.*, "Monitoring

dopants by raman scattering in an electrochemically top-gated graphene transistor," *Nature Nanotechnology*, vol. 3, no. 4, pp. 210–215, 2008.

[219] C. E. Kehayias, S. MacNaughton, S. Sonkusale, and C. Staii, "Kelvin probe microscopy and electronic transport measurements in reduced graphene oxide chemical sensors," *Nanotechnology*, vol. 24, no. 24, p. 245502, 2013.

[220] L. Hu, D. Hecht, and G. Grüner, "Percolation in transparent and conducting carbon nanotube networks," *Nano Letters*, vol. 4, no. 12, pp. 2513–2517, 2004.

[221] B. Huang, Z. Li, Z. Liu, G. Zhou, S. Hao, J. Wu, B.-L. Gu, and W. Duan, "Adsorption of gas molecules on graphene nanoribbons and its implication for nanoscale molecule sensor," *The Journal of Physical Chemistry C*, vol. 112, no. 35, pp. 13442–13446, 2008.

[222] O. Leenaerts, B. Partoens, and F. Peeters, "Adsorption of h2o, nh3, co, no2, and no on graphene: A first-principles study," *Physical Review B*, vol. 77, no. 12, p. 125416, 2008.

[223] E. S. Snow and F. K. Perkins, "Capacitance and conductance of single-walled carbon nanotubes in the presence of chemical vapors," *Nano Letters*, vol. 5, no. 12, pp. 2414–2417, 2005.

[224] S. MacNaughton, S. Sonkusale, S. Surwade, S. Ammu, and S. Manohar, "Carbon nanotube and graphene based gas micro-sensors fabricated by dielectrophoresis on silicon," in *Sensors, 2010 IEEE*, pp. 894–897, IEEE, 2010.

[225] S. Nufer, D. Fantanas, S. P. Ogilvie, M. J. Large, D. J. Winterauer, J. P. Salvage, M. Meloni, A. A. King, P. Schellenberger, A. Shmeliov, *et al.*, "Percolating metallic structures templated on laser-deposited carbon nanofoams derived from graphene oxide: applications in humidity sensing," *ACS Applied Nano Materials*, vol. 1, no. 4, pp. 1828–1835, 2018.

[226] F. M. Ernsberger, "The nonconformist ion," *Journal of the American Ceramic Society*, vol. 66, no. 11, pp. 747–750, 1983.

[227] W.-D. Lin, H.-M. Chang, and R.-J. Wu, "Applied novel sensing material graphene/polypyrrole for humidity sensor," *Sensors and Actuators B: Chemical*, vol. 181, pp. 326–331, 2013.

[228] S. Henley, J. Carey, S. Silva, G. Fuge, M. Ashfold, and D. Anglos, "Dynamics of confined plumes during short and ultrashort pulsed laser ablation of graphite," *Physical Review B*, vol. 72, no. 20, p. 205413, 2005.

[229] A. V. Rode, E. G. Gamaly, and B. Luther-Davies, "Formation of cluster-assembled carbon nano-foam by high-repetition-rate laser ablation," *Applied Physics A: Materials Science & Processing*, vol. 70, no. 2, pp. 135–144, 2000.

[230] E. Muñoz, M. de Val, M. L. Ruiz-González, C. López-Gascón, M. L. Sanjuán, M. T. Martinez, J. M. González-Calbet, F. Germán, and M. Laguna, "Gold/carbon nanocomposite foam," *Chemical Physics Letters*, vol. 420, no. 1, pp. 86–89, 2006.

[231] A. Zani, D. Dellasega, V. Russo, and M. Passoni, "Ultra-low density carbon foams produced by pulsed laser deposition," *Carbon*, vol. 56, pp. 358–365, 2013.

[232] J. Chu, X. Peng, P. Feng, Y. Sheng, and J. Zhang, "Study of humidity sensors based on nanostructured carbon films produced by physical vapor deposition," *Sensors and Actuators B: Chemical*, vol. 178, pp. 508–513, 2013.

[233] J. Wu, S. Feng, X. Wei, J. Shen, W. Lu, H. Shi, K. Tao, S. Lu, T. Sun, L. Yu, *et al.*, "Facile synthesis of 3D graphene flowers for ultrasensitive and highly reversible gas sensing," *Advanced Functional Materials*, vol. 26, no. 41, pp. 7462–7469, 2016.

[234] M. Asai, T. Ohba, T. Iwanaga, H. Kanoh, M. Endo, J. Campos-Delgado, M. Terrones, K. Nakai, and K. Kaneko, "Marked adsorption irreversibility of graphitic nanoribbons for CO_2 and H_2O," *Journal of the American Chemical Society*, vol. 133, no. 38, pp. 14880–14883, 2011.

[235] B. Cho, J. Yoon, M. G. Hahm, D.-H. Kim, A. R. Kim, Y. H. Kahng, S.-W. Park, Y.-J. Lee, S.-G. Park, J.-D. Kwon, *et al.*, "Graphene-based gas sensor:

metal decoration effect and application to a flexible device," *Journal of Materials Chemistry C*, vol. 2, no. 27, pp. 5280–5285, 2014.

[236] M. N. Ashfold, F. Claeyssens, G. M. Fuge, and S. J. Henley, "Pulsed laser ablation and deposition of thin films," *Chemical Society Reviews*, vol. 33, no. 1, pp. 23–31, 2004.

[237] M. Qian, Y. S. Zhou, Y. Gao, J. B. Park, T. Feng, S. M. Huang, Z. Sun, L. Jiang, and Y. F. Lu, "Formation of graphene sheets through laser exfoliation of highly ordered pyrolytic graphite," *Applied Physics Letters*, vol. 98, no. 17, p. 173108, 2011.

[238] A. C. Ferrari and J. Robertson, "Interpretation of raman spectra of disordered and amorphous carbon," *Physical Review B*, vol. 61, no. 20, p. 14095, 2000.

[239] J. Siegel, O. Lyutakov, V. Rybka, Z. Kolská, and V. Svorcík, "Properties of gold nanostructures sputtered on glass.," *Nanoscale Research Letters*, vol. 6, no. 1, p. 96, 2011.

[240] Y. Xue, "Water monomer interaction with gold nanoclusters from van der waals density functional theory.," *The Journal of Chemical Physics*, vol. 136, p. 024702, Jan 2012.

[241] A. D. Smith, K. Elgammal, F. Niklaus, A. Delin, A. C. Fischer, S. Vaziri, F. Forsberg, M. Råsander, H. Hugosson, L. Bergqvist, *et al.*, "Resistive graphene humidity sensors with rapid and direct electrical readout," *Nanoscale*, vol. 7, no. 45, pp. 19099–19109, 2015.

[242] C. Cao, C. Hu, L. Fang, S. Wang, Y. Tian, and C. Pan, "Humidity sensor based on multi-walled carbon nanotube thin films," *Journal of Nanomaterials*, vol. 2011, p. 5, 2011.

[243] W. S. Hummers Jr and R. E. Offeman, "Preparation of graphitic oxide," *Journal of the American Chemical Society*, vol. 80, no. 6, pp. 1339–1339, 1958.

[244] C. Vallés, J. D. Núñez, A. M. Benito, and W. K. Maser, "Flexible conductive graphene paper obtained by direct and gentle annealing of graphene oxide paper," *Carbon*, vol. 50, no. 3, pp. 835–844, 2012.

[245] L. L. Zhang and X. Zhao, "Carbon-based materials as supercapacitor electrodes," *Chemical Society Reviews*, vol. 38, no. 9, pp. 2520–2531, 2009.

[246] A. González, E. Goikolea, J. A. Barrena, and R. Mysyk, "Review on supercapacitors: technologies and materials," *Renewable and Sustainable Energy Reviews*, vol. 58, pp. 1189–1206, 2016.

[247] E. Frackowiak and F. Beguin, "Carbon materials for the electrochemical storage of energy in capacitors," *Carbon*, vol. 39, no. 6, pp. 937–950, 2001.

[248] C. Chen, E. B. Kennel, A. H. Stiller, P. G. Stansberry, and J. W. Zondlo, "Carbon foam derived from various precursors," *Carbon*, vol. 44, no. 8, pp. 1535–1543, 2006.

[249] Z. Fan, D. Qi, Y. Xiao, J. Yan, and T. Wei, "One-step synthesis of biomass-derived porous carbon foam for high performance supercapacitors," *Materials Letters*, vol. 101, pp. 29–32, 2013.

[250] P. G. Whitten, G. M. Spinks, and G. G. Wallace, "Mechanical properties of carbon nanotube paper in ionic liquid and aqueous electrolytes," *Carbon*, vol. 43, no. 9, pp. 1891–1896, 2005.

[251] M. D. Stoller, S. Park, Y. Zhu, J. An, and R. S. Ruoff, "Graphene-based ultracapacitors," *Nano Letters*, vol. 8, no. 10, pp. 3498–3502, 2008.

[252] G. Lota, T. A. Centeno, E. Frackowiak, and F. Stoeckli, "Improvement of the structural and chemical properties of a commercial activated carbon for its application in electrochemical capacitors," *Electrochimica Acta*, vol. 53, no. 5, pp. 2210–2216, 2008.

[253] M. Kim, I. Oh, and J. Kim, "Effects of different electrolytes on the electrochemical and dynamic behavior of electric double layer capacitors based on a porous silicon carbide electrode," *Physical Chemistry Chemical Physics*, vol. 17, no. 25, pp. 16367–16374, 2015.

[254] L. Borchardt, M. Oschatz, and S. Kaskel, "Tailoring porosity in carbon materials for supercapacitor applications," *Materials Horizons*, vol. 1, no. 2, pp. 157–168, 2014.

[255] M. Rose, Y. Korenblit, E. Kockrick, L. Borchardt, M. Oschatz, S. Kaskel, and G. Yushin, "Hierarchical micro-and mesoporous carbide-derived carbon as a high-performance electrode material in supercapacitors," *Small*, vol. 7, no. 8, pp. 1108–1117, 2011.

[256] Z. H. Ni, T. Yu, Y. H. Lu, Y. Y. Wang, Y. P. Feng, and Z. X. Shen, "Uniaxial strain on graphene: Raman spectroscopy study and band-gap opening.," *ACS Nano*, vol. 2, pp. 2301–5, Nov 2008.

[257] A. Ferrari and J. Robertson, "Resonant raman spectroscopy of disordered, amorphous, and diamondlike carbon," *Physical Review B*, vol. 64, no. 7, p. 075414, 2001.

[258] S. Cronin, A. Swan, M. Ünlü, B. Goldberg, M. Dresselhaus, and M. Tinkham, "Measuring the uniaxial strain of individual single-wall carbon nanotubes: resonance raman spectra of atomic-force-microscope modified single-wall nanotubes," *Physical Review Letters*, vol. 93, no. 16, p. 167401, 2004.

[259] M. Huang, H. Yan, T. F. Heinz, and J. Hone, "Probing strain-induced electronic structure change in graphene by raman spectroscopy.," *Nano letters*, vol. 10, pp. 4074–9, Oct 2010.

[260] Z. Liu, J. Zhang, and B. Gao, "Raman spectroscopy of strained single-walled carbon nanotubes.," *Chemical Communications (Cambridge, England)*, pp. 6902–18, Dec 2009.

[261] H. Sakata, G. Dresselhaus, M. Dresselhaus, and M. Endo, "Effect of uniaxial stress on the raman spectra of graphite fibers," *Journal of Applied Physics*, vol. 63, no. 8, pp. 2769–2772, 1988.

[262] A. Jorio, E. H. M. Ferreira, L. G. Cançado, C. A. Achete, and R. B. Capaz, "Measuring disorder in graphene with raman spectroscopy," in *Physics and Applications of Graphene-Experiments*, InTech, 2011.

[263] G. Zhang, S. Sun, D. Yang, J.-P. Dodelet, and E. Sacher, "The surface analytical characterization of carbon fibers functionalized by H_2SO_4/HNO_3 treatment," *Carbon*, vol. 46, no. 2, pp. 196–205, 2008.

[264] X. Li, J. Rong, and B. Wei, "Electrochemical behavior of single-walled carbon nanotube supercapacitors under compressive stress.," *ACS Nano*, vol. 4, pp. 6039–49, Oct 2010.

[265] E. Richter, H.-J. Schmidt, and H.-G. Schecker, "Adsorption and catalytic reactions of NO and NH_3 on activated carbon," *Chemical Engineering & Technology*, vol. 13, no. 1, pp. 332–340, 1990.

[266] M. Capano, N. McDevitt, R. Singh, and F. Qian, "Characterization of amorphous carbon thin films," *Journal of Vacuum Science & Technology A: Vacuum, Surfaces, and Films*, vol. 14, no. 2, pp. 431–435, 1996.

Chapter 10

Appendix

Appendix A

Air pollution survey

Department for Environment Food and Rural Affairs

What are the causes of air Pollution

Pollutant	Description and main UK sources	Potential effects on health/environment
Particulate Matter (PM-PM_{10} and $PM_{2.5}$)	Particulate Matter is generally categorised on the basis of the size of the particles (for example $PM_{2.5}$ is particles with a diameter of less than 2.5µm). PM is made up of a wide range of materials and arise from a variety of sources. Concentrations of PM comprise primary particles emitted directly into the atmosphere from combustion sources and secondary particles formed by chemical reactions in the air. PM derives from both human-made and natural sources (such as sea spray and Saharan dust). In the UK the biggest human-made sources are stationary fuel combustion and transport. Road transport gives rise to primary particles from engine emissions, tyre and brake wear and other non-exhaust emissions. Other primary sources include quarrying, construction and non-road mobile sources. Secondary PM is formed from emissions of ammonia, sulphur dioxide and oxides of nitrogen as well as from	Both short-term and long-term exposure to ambient levels of PM are consistently associated with respiratory and cardiovascular illness and mortality as well as other ill-health effects. The associations are believed to be causal. It is not currently possible to discern a threshold concentration below which there are no effects on the whole population's health. PM10 roughly equates to the mass of particles less than 10 micrometres in diameter that are likely to be inhaled into the thoracic region of the respiratory tract. Recent reviews by WHO and Committee on the Medical Effects of Air Pollutants (COMEAP) have suggested exposure to a finer fraction of particles ($PM_{2.5}$, which typically make up around two thirds of PM_{10} emissions and concentrations) give a stronger association with the observed ill-health effects, but also warn that there is evidence that the

	emissions of organic compounds from both combustion sources and vegetation.	coarse fraction between (PM_{10} – $PM_{2.5}$) also has some effects on health.
Oxides of nitrogen (NO_X)	All combustion processes in air produce oxides of nitrogen (NO_X). Nitrogen dioxide (NO_2) and nitric oxide (NO) are both oxides of nitrogen and together are referred to as NO_X. Road transport is the main source, followed by the electricity supply industry and other industrial and commercial sectors.	NO_2 is associated with adverse effects on human health. At high levels NO_2 causes inflammation of the airways. Long term exposure may affect lung function and respiratory symptoms. NO_2 also enhances the response to allergens in sensitive individuals. High levels of NO_X can have an adverse effect on vegetation, including leaf or needle damage and reduced growth. Deposition of pollutants derived from NO_X emissions contribute to acidification and/or eutrophication of sensitive habitats leading to loss of biodiversity, often at locations far removed from the original emissions. NO_X also contributes to the formation of secondary particles and ground level ozone, both of which are associated with ill-health effects. Ozone also damages vegetation.
Ozone (O_3)	Ozone is not emitted directly from any human-made source. It arises from chemical reactions between various air pollutants, primarily NO_X and Volatile Organic Compounds (VOCs), initiated by strong sunlight. Formation can take place over several hours or days and may have arisen from	Exposure to high concentrations may cause irritation to eyes and nose. Very high levels can damage airways leading to inflammatory reactions. Ozone reduces lung function and increases incidence of respiratory symptoms, respiratory hospital admissions and mortality. Ground level ozone can also cause

	emissions many hundreds, or even thousands of kilometres away.	damage to many plant species leading to loss of yield and quality of crops, damage to forests and impacts on biodiversity.
Sulphur dioxide (SO_2)	UK emissions are dominated by combustion of fuels containing sulphur, such as coal and heavy oils by power stations and refineries. In some parts of the UK, notably Northern Ireland, coal for domestic use is a significant source.	Causes constriction of the airways of the lung. This effect is particularly likely to occur in people suffering from asthma and chronic lung disease. Precursor to secondary PM and therefore contributes to the ill-health effects caused by PM_{10} and $PM_{2.5}$. Potential damage to ecosystems at high levels, including degradation of chlorophyll, reduced photosynthesis, raised respiration rates and changes in protein metabolism. Deposition of pollution derived from SO_2 emissions contribute to acidification of soils and waters and subsequent loss of biodiversity, often at locations far removed from the original emissions.
Polycyclic aromatic hydrocarbons (PAHs)	There are many different PAHs emanating from a variety of sources. This strategy uses benzo[a]pyrene (B[a]P) as a marker for the most hazardous PAHs. The main sources of B[a]P in the UK are domestic coal and wood burning, fires (eg accidental fires, bonfires, forest fires, etc), and industrial processes such as coke production. Road transport is the largest source for total PAHs, but this source is dominated by species thought to be	Studies of occupational exposure to PAHs have shown an increased incidence of tumours of the lung, skin and possibly bladder and other sites. Lung cancer is most obviously linked to exposure to PAHs through inhaled air. Individual PAHs vary in their ability to induce tumours in animals or humans. The carcinogenic potency of some PAHs is unknown or uncertain. Individual PAHs have been classified by the International Agency

	less hazardous than B[a]P.	for Research on Cancer, with three classified as "probably carcinogenic to humans", including B[a]P, and three classified as "possibly carcinogenic to humans".
Benzene	Has a variety of sources, but primarily arises from domestic and industrial combustion and road transport.	Benzene is a recognised human carcinogen which attacks the genetic material and, as such, no absolutely safe level can be specified in ambient air. Studies in workers exposed to high levels have shown an excessive risk of leukaemia.
1,3-butadiene	Mainly from combustion of petrol. Motor vehicles and other machinery are the dominant sources, but it is also emitted from some processes, such as production of synthetic rubber for tyres.	1,3-butadiene is also a recognised genotoxic human carcinogen, as such, no absolutely safe level can be specified in ambient air. The health effect of most concern is the induction of cancer of the lymphoid system and blood–forming tissues, lymphoma and leukaemia.
Carbon monoxide (CO)	Formed from incomplete combustion of carbon containing fuels. The largest source is road transport, with residential and industrial combustion making significant contributions.	Substantially reduces capacity of the blood to carry oxygen to the body's tissues and blocks important biochemical reactions in cells. People with existing diseases which affect delivery of oxygen to the heart or brain, such as angina, are at particular risk.
Lead (Pb)	Emitted from the combustion of coal and also the iron and steel combustion and nonferrous metals.	Exposure to high levels in air may result in toxic biochemical effects which have adverse effects on the kidneys, gastrointestinal tract, the joints and reproductive

		systems, and acute or chronic damage to the nervous system. Affects intellectual development in young children.
Ammonia	Mainly derived from agriculture, primarily livestock manure/slurry management and fertilisers. Small proportion derived from variety of sources including transport and waste disposal.	Ammonia can lead to damage of terrestrial and aquatic ecosystems through deposition of eutrophying pollutants and through acidifying pollutants. Precursor to secondary PM and therefore contributes to the ill-health effects caused by PM_{10} and $PM_{2.5}$.

For more information, visit the Defra Air Quality web pages at: http://airquality.defra.gov.uk

National air quality objectives and European Directive limit and target values for the protection of human health						
Pollutant	**Applies**	**Objective**	**Concentration measured as** [10]	**Date to be achieved by (and maintained thereafter)**	**European Obligations**	**Date to be achieved (by and maintained thereafter)**
Particles (PM_{10})	UK	50 µg/m^3 not to be exceeded more than 35 times a year	24 hour mean	31 December 2004	50 µg/m^3 not to be exceeded more than 35 times a year	1 January 2005
	UK	40 µg/m^3	annual mean	31 December 2004	40 µg/m^3	1 January 2005
	Indicative 2010 objectives for PM_{10} (from the 2000 strategy and Addendum) have been replaced by an exposure reduction approach for $PM_{2.5}$ (except in Scotland – see below)					
	Scotland	50 µg/m^3 not to be exceeded more than 7 times a year	24 hour mean	31 December 2010	50 µg/m^3 not to be exceeded more than 35 times a year	1 January 2005
	Scotland	18 µg/m^3	annual mean	31 December 2010	40 µg/m^3	1 January 2005
Particles ($PM_{2.5}$) Exposure Reduction	UK (except Scotland)	25 µg/m^3	annual mean	2020	Target value - 25 µg/m^3	2010
	Scotland	10 µg/m^3		31 December 2020	Limit value - 25 µg/m^3	1 January 2015
	UK urban areas	Target of 15% reduction in concentrations at urban background		Between 2010 and 2020	Target of 20% reduction in concentrations at urban background.	Between 2010 and 2020

National air quality objectives and European Directive limit and target values for the protection of human health						
Pollutant	**Applies**	**Objective**	**Concentration measured as[1]**	**Date to be achieved by (and maintained thereafter)**	**European Obligations**	**Date to be achieved by (and maintained thereafter)**
Nitrogen dioxide	UK	200 µg/m^3 not to be exceeded more than 18 times a year	1 hour mean	31 December 2005	200 µg/m^3 not to be exceeded more than 18 times a year	1 January 2010
	UK	40 µg/m^3	annual mean	31 December 2005	40 µg/m^3	1 January 2010
Ozone	UK	100 µg/m^3 not to be exceeded more than 10 times a year	8 hour mean	31 December 2005	Target of 120 µg/m^3 not to be exceeded by more than 25 times a year averaged over 3 years	31 December 2010
Sulphur dioxide	UK	266 µg/m^3 not to be exceeded more than 35 times a year	15 minute mean	31 December 2005	-	-
	UK	350 µg/m^3 not to be exceeded more than 24 times a year	1 hour mean	31 December 2004	350 µg/m^3 not to be exceeded more than 24 times a year	1 January 2005
	UK	125 µg/m^3 not to be exceeded more than 3 times a year	24 hour mean	31 December 2004	125 µg/m^3 not to be exceeded more than 3 times a year	1 January 2005
Polycyclic Aromatic Hydrocarbons	UK	0.25 ng/m^3 B[a]P	as annual average	31 December 2012	1.0 ng/m^3	31 December 2012

National air quality objectives and European Directive limit and target values for the protection of human health						
Pollutant	**Applies**	**Objective**	**Concentration measured as[1]**	**Date to be achieved by (and maintained thereafter)**	**European Obligations**	**Date to be achieved by (and maintained thereafter)**
Benzene	UK	16.25 µg/m^3	running annual mean	31 December 2003	-	-
	England and Wales	5 µg/m^3	annual average	31 December 2010	5 µg/m^3	1 January 2010
	Scotland, Northern Ireland	3.25 µg/m^3	running annual mean	31 December 2010	-	-
1,3-butadiene	UK	2.25 µg/m^3	running annual mean	31 December 2003	-	-
Carbon monoxide	UK	10 mg/m^3	maximum daily running 8 hour mean/in Scotland as running 8 hour mean	31 December 2003	10 mg/m^3	1 January 2005
Lead	UK	0.5 µg/m^3	annual mean	31 December 2004	0.5 µg/m^3	1 January 2005
		0.25 µg/m^3	annual mean	31 December 2008	-	-

National air quality objectives and European Directive limit and target values for the protection of vegetation and ecosystems						
Pollutant	**Applies**	**Objective**	**Concentration measured as[1]**	**Date to be achieved by (and maintained thereafter)**	**European Obligations**	**Date to be achieved by (and maintained thereafter)**
Nitrogen oxides	UK	30 µg/m^3	annual mean	31 December 2000	30 µg/m^3	19 July 2001
Sulphur dioxide	UK	20 µg/m^3	annual mean	31 December 2000	20 µg/m^3	19 July 2001
	UK	20 µg/m^3	winter average	31 December 2000	20 µg/m^3	19 July 2001
Ozone: protection of vegetation and ecosystems	UK	Target value of 18,000 µg/m^3 based on AOT40 to be calculated from 1 hour values from May to July, and to be achieved, so far as possible, by 2010	Average over 5 years	1 January 2010	Target value of 18,000 µg/m^3 based on AOT40 to be calculated from 1 hour values from May to July, and to be achieved, so far as possible, by 2010	1 January 2010

Appendix B

Cambride Nanoystem Graphene Datasheet

FGV Cambridge Nanosystems Ltd
17 Mercers Row
Cambridge CB5 8HY
Phone: +44 (0)1223 359 316
Email: contact@cnanos.com

Technical Datasheet **CamGraph®** graphene powders.

CamGraph® is a range of graphene powders, derived from a catalyst- and surfactant-free microwave plasma synthesis process. The CamGraph® range consists of three grades of graphene: G1 has the lowest number of graphene layers (between 1 and 5 layers), G3 contains thicker graphene flakes (between 3 and 15 layers), and G2 is a highly purified, high-conductivity version of G3.

Typical Properties

	CamGraph®		
Form	Powder		
Colour	Black		
Odour	Odourless		
Formula	C		
Particle shape	Graphitic (sp^2)		
	G1	**G2**	**G3**
Classification	Very few layer	Multi layer	Multi layer
Carbon content[8]	≥98%	>99%	≥99%
# of graphene layers[1]	3 ± 2	8 ± 5	9 ± 6
Flake thickness[1] (nm)	1.0 ± 0.7	2.7 ± 1.7	3.0 ± 2.0
Lateral size[2] (nm)	475 ± 75	400 ± 150	400 ± 150
Bulk density[3] (g/L)	30 ± 5	185 ± 15	200 ± 20
Conductivity[4] (S/m)	6090 ± 125	2000 ± 100	975 ± 75
Surface area[5,6] (m^2/g)	320 ± 20	240 ± 5	130 ± 5
Pore volume[5,7] (cm^3/g)	0.16	0.12	0.06

[1] As determined by STEM (n = 130)
[2] As determined by SEM (n = 1000)
[3] May differ slightly due to compression of powder during shipping
[4] 4-point-probe measurement on pellets (compressed under 10 bar for 20 minutes)
[5] Nitrogen BET, $P/P_0 = 0.3$
[6] For reference, graphite powder = 8.5 ± 0.5 m^2/g
[7] For reference, graphite powder = 0.005cm^3/g
[8] As determined by combustion elemental analysis (n = 6); oxygen content is determined by pyrolysis.

V 11.3, 14-Feb-2018

FGV Cambridge Nanosystems Ltd
17 Mercers Row
Cambridge CB5 8HY
Phone: +44 (0)1223 359 316
Email: contact@cnanos.com

Representative Characterisation

	G1	G2	G3
TEM	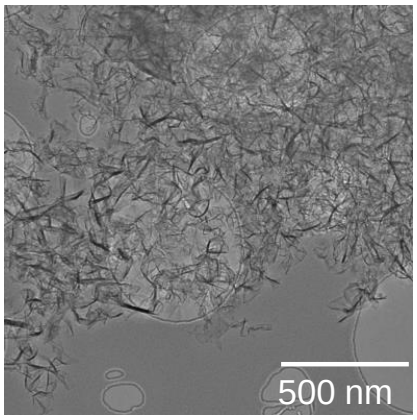	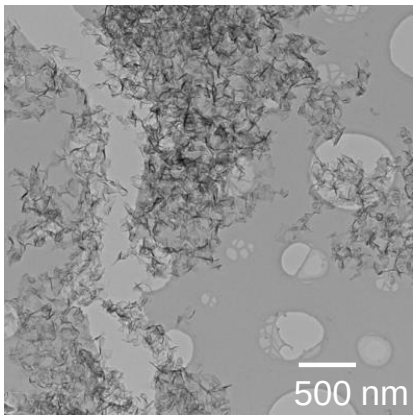	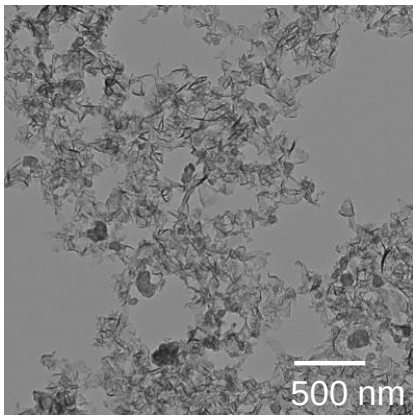
STEM	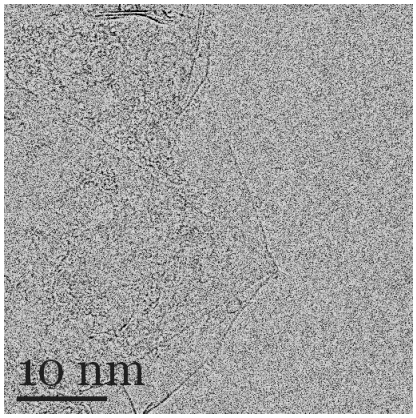	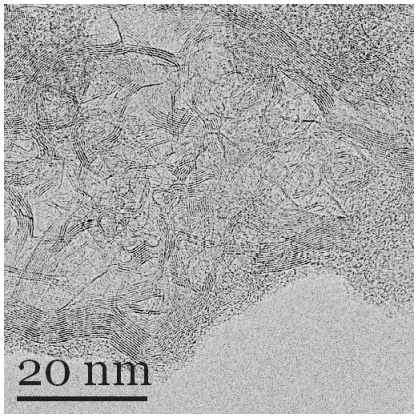	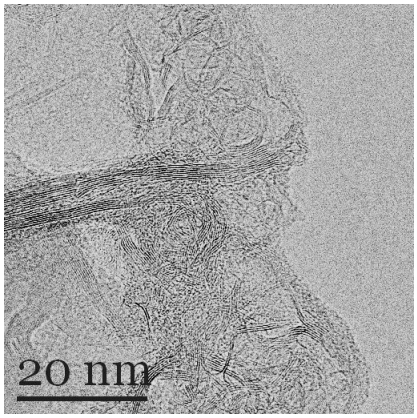
RAMAN	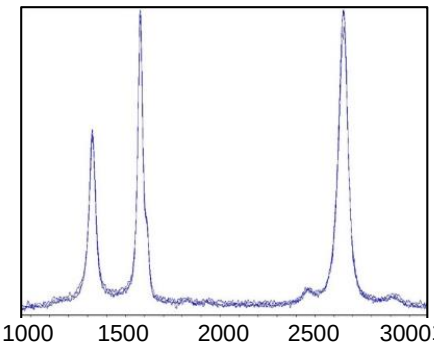	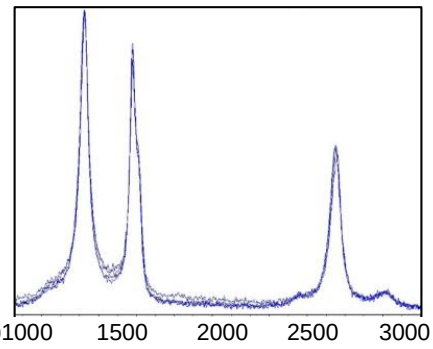	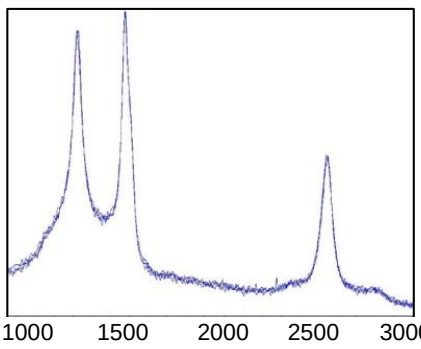

ELEMENTAL ANALYSIS								
	C	97.8	± 0.2	99.4	± 1.0	99.0	± 0.1	C
	H	0.68	± 0.02	0.31	± 0.01	0.70	± 0.02	H
	N	0.29	± 0.03	0.24	± 0.05	0.22	± 0.06	N
	O	0.99	± 0.01	0.32	± 0.01	0.56	± 0.01	O

The information contained in this datasheet is derived from analysis of a typical batch of each product. It is given for information purposes only, without guarantee.

V 11.3, 14-Feb-2018